

© Copyright 2022

Ammar Alghadeer

Human iPSC Derived Ameloblast Organoid Guided by Single-Cell Atlas of
Human Tooth Development

Ammar Alghadeer

A dissertation

submitted in partial fulfillment of the
requirements for the degree of

Doctor of Philosophy

University of Washington

2022

Reading Committee:

Hannele Ruohola-Baker, Chair

Tracy Popowics

Hai Zhang

Program Authorized to Offer Degree:

Oral Health Sciences

University of Washington

Abstract

Human iPSC Derived Ameloblast Organoid Guided by Single-Cell Atlas of Human Tooth Development

Ammar Alghadeer

Chair of the Supervisory Committee:
Professor Hannele Ruohola-Baker
Department of Biochemistry

Tooth enamel secreted by ameloblasts is the hardest material in the human body, acting as a shield protecting the teeth. However, the enamel is gradually damaged or partially lost in over 90% of adults and cannot be regenerated due to a lack of ameloblasts in erupted teeth. In contrast, dentin, the second hardest material in the tooth, continues to be produced by the odontoblasts in the dental pulp. Moreover, undifferentiated dental pulp stem cells (DPSCs), which are present in erupted teeth, are known to participate in the repair of injured dentin, by differentiating into odontoblast-like cells. Here we developed a regenerative strategy to replicate the interface between ameloblast and odontoblasts *in vitro* utilizing the human induced pluripotent stem cells (hiPSCs) to generate early ameloblasts, and DPSCs to generate odontoblast progenitors.

First, we studied the DPSCs from third molars of a diverse patient group. Using high throughput transcriptomic, proteomic analysis, and metabolic flux analysis, we identified the signature for the optimal populations of DPSCs that can be used for expansion and regeneration that do not show rapid cellular senescence phenotype. In particular, we show that the transforming growth factor-beta (TGF- β) pathway and the cytoskeletal proteins are upregulated in rapid aging DPSCs, indicating a loss of stem cell characteristics and spontaneous initiation of terminal differentiation in this particular population.

Second, we used sci-RNA-seq to establish a spatiotemporal single-cell atlas for the developing human tooth and identify regulatory mechanisms controlling the differentiation process of human ameloblasts. We revealed key signaling pathways involved between the support cells and ameloblasts during fetal development and recapitulate those findings in a novel human ameloblast *in vitro* differentiation from hiPSCs. We furthermore developed an enamel organ-like 3D organoid.

Finally, we cocultured the optimal DPSCs population we identified with the newly developed ameloblast organoid to form a polarized ameloblast interface with odontoblast progenitors. These studies pave the way for future regenerative dentistry and therapies toward genetic diseases affecting enamel formation.

TABLE OF CONTENTS

List of Figures	ix
List of Tables	xii
Chapter 1. Dental pulp stem cells	1
1.1 Background	1
1.2 Materials and Methods	3
1.2.1 Extraction and primary culture of DPSCs	3
1.2.2 Cell Culture	4
1.2.3 Protein isolation and Western blotting	5
1.2.4 Flow Cytometry	6
1.2.5 Directed differentiation	6
1.2.6 Osteo/odontogenesis quantification assay	7
1.2.7 Adipogenesis quantification assay	7
1.2.8 RNA extraction and RT-qPCR analysis	8
1.2.9 Transcriptomic data analysis	9
1.2.10 Overexpression of BARX1 and validation of BARX1 antibody in HeLa cells	9
1.2.11 Immunostaining and confocal imaging	10
1.2.12 SeaHorse Extracellular Flux assay	10
1.2.13 Cell surface area measurements	11
1.2.14 Senescence assay	11
1.2.15 Proteomics	11

1.2.16	String analysis.....	12
1.2.17	Secretome prediction analysis.....	12
1.3	Results of DPSC characterization.....	13
1.3.1	Previously identified MSC markers are differentially expressed across DPSC lines generated from patients.....	13
1.3.2	Rapid and slow aging DPSC cell lines	16
1.3.3	DPSC lines are heterogeneous in their differentiation capacities.....	17
1.3.4	DPSCs exhibit a unique transcriptome profile.....	21
1.3.5	BARX1 as a DPSCs marker	26
1.3.6	Metabolic signature, predictive of the rapid aging	29
1.3.7	Rapid aging DPSC cell lines showed increase in TGF-beta pathway activity and upregulation of cytoskeletal regulators.....	32
1.3.8	TGFβ pathway activation induces stress fiber formation and correlates with rapid DPSCs aging.....	35
1.4	Discussion and conclusions	42
Chapter 2. The development of induced ameloblasts		45
2.1	Background.....	45
2.2	Results Ameloblast project	47
2.2.1	A single-cell atlas of the developing human fetal odontogenic tissues	47
2.2.2	sci-RNA-seq and spatial localization reveal stage-specific support cell types and cervical loop stem cells for ameloblast differentiation.....	55

2.2.3	Sci-RNA-seq reveals spatio-temporal expression patterns of critical signaling pathways in ameloblasts and facilitates the development of human iPSC-derived ameloblasts (iAM) in vitro	67
2.2.4	3D Enamel organoids show mineralization and Ameloblastin, Amelogenin, and Enamelin secretion	80
2.3	Discussion and conclusions	85
2.4	Materials and Methods.....	89
2.4.1	Tissue collection and dissection.....	89
2.4.2	Nuclei extraction.....	90
2.4.3	Sci-RNA-seq.....	91
2.4.4	Data Analysis	92
2.4.5	Top marker genes.....	93
2.4.6	Heatmap and GO-terms enrichment	93
2.4.7	Pseudotime analysis	94
2.4.8	Top pathway analysis.....	94
2.4.9	Differential expression.....	96
2.4.10	Multilayer network analysis.....	96
2.4.11	Signaling interaction	96
2.4.12	Datasets projection analysis.....	97
2.4.13	RNA Fluorescence in situ Hybridization (FISH) and analysis.....	98
2.4.14	In vitro differentiation.....	99
2.4.15	De novo FGFR-Miniprotein expression	100
2.4.16	RNA extraction and RT-qPCR analysis	101

2.4.17	Development of Ameloblast Organoid	102
2.4.18	Co-culture protocol for monolayer	103
2.4.19	Cryosectioning and Immunostaining for the organoids.....	103
2.4.20	Wholemout immunostaining analysis.....	105
2.4.21	Injection of iPSC-derived ameloblast-like cells into mouse muscles.....	106
2.4.22	Calcification assays: Von Kossa and Alizarin Red Staining	106
2.4.23	Cryosectioning of fetal samples.....	107
2.4.24	Immunofluorescence staining and Confocal Imaging	107
2.4.25	Data availability	108
2.4.26	Code availability	109
	References.....	110

LIST OF FIGURES

Figure 1.1. Extraction summary.....	13
Figure 1.2. Preliminary screening.....	14
Figure 1.3. Fluorescent cytometry.....	15
Figure 1.4. Difference in growth kinetics within the candidate cell lines.....	17
Figure 1.5. Osteo/odontogenic and Adipogenic potential of DPSCs.....	18
Figure 1.6. TeSR cocktail rescue DPSC 43.....	20
Figure 1.7. Transcriptome of DPSCs compared to BM-MS, Fibroblasts and hESCs....	21
Figure 1.8. Differential expression between DPSCs, BM-MS, Fibroblasts and hESCs.	22
Figure 1.9. BARX1 gene as a new specific marker for DPSCs.....	27
Figure 1.10. BARX1 is not highly expressed in BM-MS.....	28
Figure 1.11. Metabolic assays.....	30
Figure 1.12. Glycolysis assay on candidate DPSCs.....	31
Figure 1.13. Proteomic analysis.....	32
Figure 1.14. Go Term analysis.....	33
Figure 1.15. String analysis.....	34
Figure 1.16. TGF- β pathway related proteins.....	35
Figure 1.17. Secretome prediction.....	36
Figure 1.18. Secretome go terms.....	37
Figure 1.19. SPIA analysis.....	38
Figure 1.20. TGF β pathway control stress fibers in DSPCs.....	39
Figure 1.21. Stress fibers comparison between SA and RA.....	40
Figure 1.22. Differentially expressed genes in cells with slow aging phenotype.....	41
Figure 1.23. Conclusion model.....	44
Figure 2.1. Tooth development and the design of sci-RNA-seq.....	48
Figure 2.2. The dissected samples.....	49
Figure 2.3. Visualization of all sequenced data.....	50
Figure 2.4. Distribution by sample.....	51
Figure 2.5. Heatmap for top markers of each cluster.....	51

Figure 2.6. Stages of tooth development	54
Figure 2.7. Ameloblasts and odontoblasts markers	54
Figure 2.8. Oral and dental epithelial lineages	55
Figure 2.9. Heatmap for top marker genes of dental epithelial lineages	56
Figure 2.10. Heatmap for top marker broken by timepoints.....	57
Figure 2.11. Realtime density plots	58
Figure 2.12. Pesudotime and realtime overlay.....	59
Figure 2.13. Gene expression plots for top marker genes.....	60
Figure 2.14. RNAScope for 13gw toothgerm.....	61
Figure 2.15. RNAScope for 19gw toothgerm.....	62
Figure 2.16. Cluster mapping for 19gw toothgerm.....	63
Figure 2.17. Simplified diagram of the cluster locations.....	66
Figure 2.18. Top pathway analysis work flow.....	67
Figure 2.19. Top pathways in ameloblasts development.....	68
Figure 2.20. The sources of ligands.....	69
Figure 2.21. WNT pathway in ameloblasts development.....	71
Figure 2.22. Induced ameloblast (iAM) differentiation protocol.	72
Figure 2.23. QRT-PCR of oral epithelial markers.....	73
Figure 2.24. Morphology of differentiated cells.....	73
Figure 2.25. RNA-seq of day 16 cells.....	74
Figure 2.26. Importance of each pathway in iAM differentiation.	75
Figure 2.27. sci-RNA-seq for differentiated samples	77
Figure 2.28. Projection of Day16 into UMAP of fetal AM lineage	78
Figure 2.29. Integration of Day16 with fetal AM lineage	78
Figure 2.30. LIGER river plot and labeled Day 16 clusters	79
Figure 2.31. Percentage of AMBN+ cells in Day 16.....	79
Figure 2.32. iAM transplantation into <i>in vivo</i> mouse model	80
Figure 2.33. Mouse <i>in vivo</i> experiments (continued)	81
Figure 2.34. iAM organoids formation.....	82
Figure 2.35. iAM/DPSC-OB organoids coculture.....	83

Figure 2.36. iAM/DPSC-OB coculture and polarity switch. 84

LIST OF TABLES

Table 1.1. Serum free media (SFM)	6
Table 1.2. MAPC Osteoblast Differentiation Media	7
Table 1.3. MAPC Adipocyte Differentiation Media	7
Table 1.4. qPCR Primers	8
Table 1.5. Differentially expressed genes in ESC vs MSC/DPSC	23
Table 1.6. Genes over-expressed in MSC/DPSC compared to Fibroblasts	24
Table 1.7. Differentially expressed genes in MSC vs DPSC.....	25
Table 1.8. Differentially expressed genes in Rapid ageing vs Slow ageing phenotypes..	42
Table 2.1. Marker genes used to identify cell types in Figure 2.3	52
Table 2.2. Marker genes used to identify cell types of the dental epithelium	57
Table 2.3. Logic table used to map clusters.....	60
Table 2.4. Sequencing Depth	93
Table 2.5. List of QRT-PCR primers.....	102
Table 2.6. List of primary antibodies.....	104
Table 2.7. List of Secondary antibodies.....	105

ACKNOWLEDGEMENTS

I thank the Ruohola-Baker lab members for helpful discussions during the course of this work. I thank Dannie Macrin for teaching me the basics ever since I joined the lab. I thank Dr. Dodson, Dr. Popowics, Dr. Janebodin and UW dental clinic, patients who consented giving the extracted teeth for research purpose. I thank Luiza Carvalho, Ella Nestingen and Benjamin Baker for their help. I thank Anjali Patni, Yan Ting Zhao, Dr. Sessa Hanson-Drury, Dr. Devon Ehnes, Chris Cavanaugh, Fatima Al-Shimmary, Christopher Kelley, Aaron Liu and Zicong Li for their excellent technical help. I thank Prof. Carol Ware, Prof. Julie Mathieu, Prof. Jessica Young and Dr. Hai Zhang for inspiring discussions and guidance. I thank Jennifer Dempsey, Ian Phelps, Dr. Diana O'Day from BDRL for processing and collecting the samples from the donors and troubleshooting the nuclei isolation. I thank Dr. Cailyn Suprell, Aishwarya Gogate and Dr. Lea Starita from BBI for the technical support and overall guidance in the design of the sequencing project. I thank Dr. Mary Reigier for assistance in computational quantification of the RNAScope co-expression channels. This work is supported in part by the University of Washington's Proteomics Resource (UWPR95794). RTM is an Investigator of the HHMI. This work is supported in part by grants from CoMotion Innovation Fund, the National Institutes of Health 1P01GM081619, R01GM097372, R01GM97372-03S1 and R01GM083867 and the NHLBI Progenitor Cell Biology Consortium (U01HL099997; UO1HL099993). This work was supported by the BBI grants. This work was also supported by Dr. Douglass L. Mourell Research Fund, and by Imam Abdulrahman bin Faisal University, and Saudi Arabian Cultural Mission (SACM) to the USA.

DEDICATION

To my parents who have encouraged and supported me in this long journey, and to everyone I consider a close family who never hesitated to lift me up during my struggle.

Chapter 1. DENTAL PULP STEM CELLS

1.1 BACKGROUND

In the adult human body, stem cells are present in most of the organs in varying proportions performing the biological function of ensuring normal regeneration needed for the maintenance of the organ (La Noce et al., 2014; Laurenti and Gottgens, 2018; Montagnani et al., 2016; Oh et al., 2014; Soteriou and Fuchs, 2018). Understanding the basic molecular mechanisms that govern the regenerative capacity of adult stem cells may allow us to utilize these cells for future therapeutic approaches such as regenerative medicine and tissue engineering.

Mammalian teeth are formed during development by the interactions between the cranial neural crest derived mesenchyme and the oral ectoderm (An et al., 2018; Balic and Thesleff, 2015; Miletich and Sharpe, 2004). Previous studies have revealed a stem cell population that remains regenerative in adult teeth, the perivascular dental pulp stem cells (DPSC) in postnatal human dental pulp (Shi and Gronthos, 2003). DPSCs in humans are known to be involved in regeneration of dentin structure produced by odontoblast cells (Almushayt et al., 2006; Balic and Thesleff, 2015; Gronthos et al., 2000; Neves et al., 2017; Sharpe, 2016).

Stem cells isolated from dental pulp have been successfully differentiated into adipogenic, chondrogenic, osteogenic and odontogenic lineages (Hosoya and Nakamura, 2015; Isobe et al., 2016; Paduano et al., 2016). DPSCs are thought to express mesenchymal cell surface markers such as CD44, CD45, CD73, CD90, CD146, CD29 and Stro-1 (Govindasamy et al., 2011; Gronthos et al., 2011; Isobe *et al.*, 2016; Ponnaiyan and Jegadeesan, 2014) and some reports suggest that they

might express pluripotent markers OCT3/4, NANOG and SOX2 (Atari et al., 2012). While many studies use MSC markers to characterize these unique stem cells and attribute their differentiation capacity to the combinatorial expression of these molecular markers, no specific markers have been identified for DPSCs.

As observed with many adult stem cells, mesenchymal stem cells (MSC) from various tissues also show age-dependent decline in their regenerative capacity. Proliferation and differentiation capacities of MSCs isolated from older individuals' bone marrow (Siegel et al., 2013), adipose tissue (Alt et al., 2012), or teeth (Alraies et al., 2017) are significantly reduced compared to young individuals. The clinical data correlate with this notion as well. In the dental field, pulp capping is a treatment utilized by many dentists by introducing protective materials such as calcium hydroxide on an exposed vital pulp to induce the pulp cells to differentiate and produce a protective dentin-like layer on top. The success rate of this treatment after 1–5 years follow-up is reported to be significantly lower in older age groups (Cho et al., 2013; Lipski et al., 2018; Marques et al., 2015). This correlates with the reduced properties of DPSCs isolated from senior individuals. However, it is not clear if the different onset of stem cell aging between individuals can be predicted or prevented at an earlier stage.

While many studies have reported the common indicators of aging such as telomerase shortening, reduction in differentiation potential and cells' morphological abnormalities, little is known about the aging mechanism and metabolic signature. We analyzed the metabolic signature in DPSCs derived from multiple individuals to characterize reliable DPSC specific signature. We showed that DPSC cell surface markers CD29, CD44, CD146 and Stro-1 are differentially

expressed across individuals. We also employed assays to quantitatively measure the differentiation capabilities of these cells into osteo/odontogenic and adipogenic lineages. Through genome wide RNA seq analysis we identified homeobox protein, Barx1, as a marker for DPSCs. Using high resolution proteomic analysis, we identified markers for rapid aging DPSC populations. In particular, we showed that the TGF- β pathway and the proteins associated with regulation of cytoskeleton are upregulated in rapid aging DPSCs, indicating a loss of stem cell character and early initiation of terminal differentiation. Importantly, using metabolic flux analysis we identified how the metabolic signature differs between normal vs. rapid aging DPSCs. This metabolic signature is predictive since the differences can be observed prior to replicative senescence phenotypes.

1.2 MATERIALS AND METHODS

1.2.1 *Extraction and primary culture of DPSCs*

Dental pulp stem cells were isolated from human third molars or deciduous teeth from 300 patients ranging from 9 to 58 years old. Teeth were collected from the University of Washington dental clinic after obtaining an informed consent from the patient or legal guardian. This study was approved by the Human Subjects Division of the University of Washington (HSD#51634-EJ) and all methods were performed in accordance with the relevant guidelines and regulations. The teeth were stored in DMEM Glutamax media (Gibco) with 10% Fetal Bovine serum (FBS) (VWR) solution immediately after tooth extraction. Each individual tooth was cut using a dremel at the cemento-enamel junction which exposed the pulp chamber. The pulp was then removed and minced into small pieces. The isolation of pulp tissue was done as previously (Karamzadeh et al., 2012) with the slight modifications and optimization. The pulp tissue underwent an enzymatic

digestion with a solution of collagenase type I (92 μ M) (Sigma-Aldrich, 9001-12-1) and dispase (444 μ M) (Gibco, 17105-041) for an hour at 37 °C with occasional vortexing. Digested pulp pieces were centrifuged to remove the enzyme solution and seeded into proliferation media containing DMEM Glutamax media (Gibco), 10% FBS (Invitrogen), ascorbic acid (0.1 mM) and 1X antibiotic antimycotic solution (Sigma-Aldrich) in a 35-mm cell culture plate. The DPSC292 was isolated from an intact deciduous tooth that was surgically extracted from a nine-year-old patient by the dentist. Pulp tissues from the deciduous teeth were isolated with the same protocol and seeded in proliferation media supplemented with insulin growth factor (IGF-1) to increase proliferation success. Once seeded, the pulp pieces were incubated at 37 °C with 5% CO₂ with media changed every 3 days until cells migrated out and optimal confluence was achieved. When the cells were ~70% confluent, they were trypsinized and passaged to allow expansion in a 10 cm plate for cryopreservation or further experimentation. The passaged DPSCs were cultured and maintained in media containing 10% FBS and 1% Penicillin-Streptomycin (Invitrogen) in DMEM. The cell lines that were selected for further studies DPSC 29, DPSC 43 and DPSC 44 originate from female donors, while DPSC 45 originate from a male donor.

1.2.2 *Cell Culture*

HeLa (ATCC), human foreskin fibroblasts (HFFs) (Stadler et al., 2010), DPSCs (PT-5025) and MSCs derived from bone marrow (MSC, PT-2501) cell lines (Lonza) were cultured with the same media composition as DPSCs later passages (10% FBS and 1% Penicillin-Streptomycin in DMEM). Human embryonic stem cells (hESCs) [Elf-1(NIH_hESCs Registry #0156)] were cultured as previously described in hESCs media (Sperber et al., 2015). Briefly, cells were grown in either mTeSR1 media (StemCell Technologies) or 2iL-I-F media (DMEM/F-12 media supplemented with 20% knock-out serum replacer (KSR), 0.1 mM nonessential amino acids

(NEAA), 1 mM sodium pyruvate, penicillin/streptomycin (all from Invitrogen, Carlsbad, CA), 0.1 mM β -mercaptoethanol (Sigma-Aldrich, St. Louis, MO), 1 μ M GSK3 inhibitor (CHIR99021, Selleckchem), 1 μ M of MEK inhibitor (PD0325901, Selleckchem), 10 ng/mL human LIF (Chemicon), 5 ng/mL IGF1 (Peprotech) and 10 ng/mL bFGF.

1.2.3 *Protein isolation and Western blotting*

Protein extraction and Western blot analysis were performed following previously described procedures (Mathieu et al., 2011). Proteins were isolated from 80% confluent plate by direct lysis with a lysis buffer containing 20 mM Tris-HCl (pH 7.5), 150 mM NaCl, 15% Glycerol, 1% Triton, 3% SDS, 25 mM β -glycerophosphate, 50 mM NaF, 10 mM Sodium Pyrophosphate, 0.5% Orthovanadate, 1% PMSF (all chemicals were from Sigma-Aldrich, St. Louis, MO), 25 U Benzonase Nuclease (EMD Chemicals, Gibbstown, NJ) and protease inhibitor cocktail (Pierce™ Protease Inhibitor Mini Tablets, Thermo Scientific, USA). Total protein was quantified by Bradford's assay and 10 μ g of protein extracts were loaded, separated by either 7.5% SDS-PAGE, or by 4–20% Mini-PROTEAN TGX gels (Bio-Rad Laboratories, Hercules, California, United States. Cat. #456-1094) and transferred to nitrocellulose membrane (0.2 μ M, Bio-Rad Laboratories, Hercules, California, United States). Membranes were blocked with 5% non-fat dry milk for at least 60 minutes at room temperature and incubated overnight at 4 °C with primary antibody. The next day, the membranes were incubated for one hour with horseradish peroxidase-conjugated secondary antibodies, and then visualized using Immobilon Western Chemiluminescent HRP Substrate (Millipore Corp, Billerica, MA). Primary antibodies used were CD29 (Abcam 1:1000), CD146 (Abcam, Cambridge, MA; 1:1000), BARX1 (Santa Cruz Biotechnology, sc-81956, 1:200) and β III tubulin (Promega, 1:1000).

1.2.4 *Flow Cytometry*

Cells grown to an optimal confluence of 70% were used for FACS analysis. Single cell suspension was prepared by dissociating the cells using 0.05% Trypsin and triturating in PFN (PBS + 5%FBS + 0.1% Sodium Azide). The cells were fixed with 4% paraformaldehyde in PFN over ice for 1 hour. The fixed cells were incubated with two primary antibodies per experiment (CD29[Abcam, 1:100]/CD146[Abcam, 1:50 and CD44[Abcam, 1:50]/Stro1[R&D Systems, 1:50]) at 4 °C overnight. Subsequently, the cells were incubated with fluorescent secondary antibodies over ice for 1 hour and analysed by flow-cytometer (Canto II, BD Biosciences). FlowJo software was used for gating and further analysis.

1.2.5 *Directed differentiation*

DPSCs were cultured in 6 well plates for a period of 4–7 days until they reached 70% confluency and differentiated into adipogenic and osteo/odontogenic cells using different conditions supplemented in media. A serum free media (SFM) (Table 1.1) was used as the base media for differentiation. The cells were treated with differentiation media for 10 days for osteo/odontogenesis (media components (Muguruma et al., 2003; Pittenger et al., 1999): Table 1.2) and 7 days for adipogenesis (media components (Muguruma *et al.*, 2003): Table 1.3) with media change every 3 days.

Table 1.1. Serum free media (SFM)

COMPONENTS	Supplier information	Stock Concentration	Final concentration
MCDB-201 media	Sigma M-6770	1L sachet powder	40% v/v
LA-BSA	Sigma L-9530	100x	1x
ITS	Sigma I-3146	100x	1x
PenStep	Hyclone SH30010	100x	1x
2P L-Ascorbic Acid	Sigma A-8960	10mM	0.1mM
DMEM-LG	Gibco 11885092	-	62% v/v
Dexamethasone	Sigma D-2915	250µM	50nM

Table 1.2. MAPC Osteoblast Differentiation Media

COMPONENTS	Supplier information	Stock Concentration	Final concentration
Serum Free Media			78% v/v
FBS	Gibco, 10437028		10%
β - Glycerophosphate	CalBiochem 36575	0.1M	10mM
2P L-Absorbic Acid	A-8960	0.1M	0.2mM
Dexamethasone	Sigma D-2915	250 μ M (H ₂ O)	100nM

Table 1.3. MAPC Adipocyte Differentiation Media

COMPONENTS	Supplier information	Stock Concentration	Final concentration
Serum Free Media			88.5% v/v
Horse Serum			10%
Indomethacin	Alfa Aesar A19910	10mM	100 μ M
Dexamethasone	Sigma D-2915	250 μ M (H ₂ O)	1 μ M
3-isobutyl-1-methyl-xanthine (IBMX)	ACROS 228420010	0.5M	0.5mM

1.2.6 *Osteo/odontogenesis quantification assay*

The candidate cell lines (29, 44, 43 and 45) were cultured in osteo/odontogenic differentiation media for 10-days, followed by fixation with 4% paraformaldehyde in PBS and stained with DAPI. After DAPI quantification, the cells were stained with Alizarin Red stain (binds to extracellular calcifications). The alizarin stain was released with 10% acetic acid and neutralized with 0.1 M ammonium hydroxide. The staining intensity was then quantified in Wallac EnVision system and the relative absorption was calculated by normalizing the alizarin dye absorption with the DAPI emission.

1.2.7 *Adipogenesis quantification assay*

Cells were incubated in the adipogenic medium for 10 days. The media was removed, and the cells were fixed with 4% paraformaldehyde for 10 minutes. The excess paraformaldehyde was washed off with PBS. 1X BODIPY stain was added and incubated in the dark for 5 minutes. The excess

BODIPY stain was removed and rinsed with PBS. The cells were counter stained with DAPI and visualized under fluorescent microscope (Zeiss). Alternatively, after the 7-days adipogenic differentiation, cells were fixed with 4% paraformaldehyde in PBS and stained with DAPI. The total DAPI emission was quantified in a Wallac EnVision multiplate reader. Then the cells were stained with Oil Red O (ORO) (binds to the neutral lipids). The ORO stain was released by dissolving in 100% isopropyl alcohol for 10 min on a rocker. 80% of the total extraction volume was used for colorimetric quantification with the Wallac EnVision system, and the relative absorption was calculated by normalizing the ORO absorption with the DAPI emission.

1.2.8 RNA extraction and RT-qPCR analysis

RNA was extracted using Trizol (Life Technologies) according to manufacturer's instructions. RNA samples were treated with Turbo DNase (Thermo Fisher Scientific) and quantified using Nanodrop ND-1000. Reverse transcription was performed using iScript cDNA Synthesis Kit (Bio-Rad). 10 ng of cDNA was used to perform qRT-PCR using SYBR Green (Applied Biosystems) or TaqMan (Applied Biosystems) on a 7300 real time PCR system (Applied Biosystems). The PCR conditions were set up as the following: stage 1 as 50 °C for 2 mins, stage 2 as 95 °C for 10mis, 95 °C for 15 sec, 60 °C for 1 min (40 Cycles). β -actin was used as an endogenous control. The primer sequences used in this work are shown in Supplementary Table S4.

Table 1.4. qPCR Primers

GENES	Primers	Sequences (5'-3')
Beta-Actin (NM_001101)	Forward	TCCCTGGAGAAGAGCTACG
	Reverse	GTAGTTTCGTGGATGCCACA
RUNX2 (NM_001024630.3)	Forward	TGGAACATCTCCATCAAGGCAG
	Reverse	TCAGGATATTCGGGACGTTGGA
LPL (NM_000237)	Forward	ATGGAGAGCAAAGCCCTGCTC
	Reverse	GTTAGGTCCAGCTGGATCGAG
BARX1 (NM_021570)	TaqMan	Applied Biosystems [Hs00222053_m1] Catalog Number: 4331182

1.2.9 *Transcriptomic data analysis*

RNA was isolated from freshly revived cell samples (Passage 3–5) of the candidate cell lines and forwarded/directed for transcriptome analysis to Covance Genomics lab. RNA-seq were aligned to Ensembl GRCh37 using Tophat ((Trapnell et al., 2009), version 2.0.13). Raw RNA-seq reads from this study and others (Chan et al., 2013; Gafni et al., 2013; Grow et al., 2015; Hanzelmann et al., 2015; Purcell et al., 2014; Sperber *et al.*, 2015; Takashima et al., 2014; Theunissen et al., 2016; Theunissen et al., 2014; Ware et al., 2014) were used. Gene-level read counts were quantified using FeatureCounts (Liao et al., 2014) using Ensembl GRCh 37 gene annotations. Prcomp function from R was used to for Principal Component Analysis. DESeq (Anders and Huber, 2010) was used for differential gene expression analysis. TopGO R package (Alexa et al., 2006) was used for Gene Ontology enrichment analysis, as well as DAVID 6.8 online analytic tool (Huang da et al., 2009a; b). SPIA R package (Tarca et al., 2013) was used for signalling pathway impact analysis utilizing pathway topology data downloaded from KEGG's website (Kanehisa et al., 2017) on: 3/25/2018. RNA-seq datasets generated for this study are available in the NCBI GEO database under accession number (GSE123973).

1.2.10 *Overexpression of BARX1 and validation of BARX1 antibody in HeLa cells*

HeLa cells were transfected overnight with 2 µg/ml of a pcDNA3.1(+) plasmid, constitutively expressing BARX1 under the control of CMV promoter, supplied by Genescript (CloneID: OHu15603). The transfection was carried out with Lipofectamine 3000 transfection kit (Thermo Fisher Scientific). Protein isolation and quantification was done after 48 h as described in protein isolation and western blotting section. DPSC Lonza were transfected with electroporation (Amaxa Nucleofector device) with 2 µg/ml of the same plasmid. Transfected HeLa cells and DPSC Lonza

were plated in a 4-well glass chamber slide system (Thermo Fisher Scientific) overnight and fixed the following day as described in immunostaining and confocal imaging section.

1.2.11 *Immunostaining and confocal imaging*

Cells were fixed in 4% paraformaldehyde in PBS for 15 minutes, and blocked in 2% BSA, 0.1% Triton X-100 in PBS. The cells were then incubated in Anti-BARX1 (1:100, Santa Cruz Biotechnology, sc-81956) overnight. The cells were washed with PBS and incubated with Alexa 488-conjugated secondary antibody (Molecular Probes, 1:500) in 1 hr. DAPI (Nuclear stain) and Alexa Flour 568 phalloidin (Selectively stains F-Actin, 1:250, Thermo Fisher Scientific) were used as counter stains and mounted with 2% of n-Propyl Gallate in 90% Glycerol + PBS solution. Analysis was done on a Leica TCS-SPE Confocal microscope using a 40x objective and Leica Software.

1.2.12 *SeaHorse Extracellular Flux assay*

DPSCs, MSCs and hESCs were seeded on a 96 well seahorse plate at 2×10^4 or 4×10^4 cells/well. The following day culture medium was replaced with base medium (Agilent Seahorse XF base medium, USA) and 1 mM Sodium pyruvate (Gibco). Then, based on the assay type, the media was supplemented with 25 mM glucose (mitostress assay), 25 mM glucose and 50 μ M carnitine (palmitate assay) or 2 mM glutamine (glucose stress assay) 1 hour before starting the assay. The cells were treated with various substrates and selective inhibitors. Mitostress: oligomycin (2.5 μ M), FCCP (1 μ M), rotenone (2.5 μ M) and antimycin (2.5 μ M). Palmitate assay: palmitate (50 μ M in BSA), BSA and ETO (50 μ M). Glucose assay: glucose (2.5 mM), oligomycin (1 μ M) and 2-DG (50 mM). The OCR values were then normalized with readings from Hoechst staining which corresponded to the number of cells in the well.

1.2.13 *Cell surface area measurements*

Bright-field images of cell culture were taken with ZEISS Axio Observer inverted microscope equipped with AxioCam MR R3 camera sensor. Images were processed by manually drawing a line around the cells and then individual cell area were measured with Fiji software distribution of ImageJ v1.51n (Schindelin et al., 2012; Schindelin et al., 2015).

1.2.14 *Senescence assay*

Analysis of cellular senescence was carried out using a Cellular Senescence Live Cell Analysis Assay Kit (Enzo Life Sciences, NY, USA. Catalog number: ENZ-KIT130-0010). Briefly, cells were treated with pretreatment solution at 37 °C for 2 h. Next, senescence-associated β -galactosidase (SA- β -gal) substrate solution was added to the cells overnight. The stained cells were trypsinized and washed twice in PBS containing 2% FBS. Cells were analysed by flow-cytometer (Canto I, BD Biosciences) and FlowJo software (TreeStar, Ashland, OR, USA).

1.2.15 *Proteomics*

Cells were analysed as described previously (Hofsteen et al., 2016; Moody et al., 2017) with minor modifications. Briefly, cells were lysed in 1 M urea, 50 mM ammonium bicarbonate, pH 7.8, and extracted proteins were quantified with a BCA (Bicinchoninic Acid) assay. Proteins were reduced with 2 mM DTT, alkylated with 15 mM iodoacetamide, and digested overnight with trypsin. The resulting peptides were desalted on Waters Sep-Pak C18 cartridges. Peptides were analysed by nano-LC-MS/MS on a Fusion Orbitrap (Thermo Fisher Scientific). Peptides were separated online by reverse phase chromatography using a heated 50 °C 30 cm C18 columns (75 mm ID packed with Magic C18 AQ 3 μ M/100 A beads) in a 280 min gradient (1% to 45% acetonitrile with 0.1% formic acid) separated at 250 nL/min. The Fusion was operated in data-dependent mode with the

following settings: 60000 resolutions, 350–1500 m/z full scan, Top Speed 2 seconds, and a 1.8 m/z isolation window. Identification and label free quantification of peptides were done with MaxQuant 1.5.7.4 using a 1% false discovery rate (FDR) against the human Swiss-Prot/TrEMB database downloaded from Uniprot on June 2nd, 2016. The databases contained forward and reverse human sequences as well as common contaminants. Peptides were searched using a 5 ppm mass error and a match between run window of 2 min. The mass spectrometry proteomics data have been deposited to the ProteomeXchange Consortium via the PRIDE partner repository with the dataset identifier PXD011962.

1.2.16 *String analysis*

Protein-protein interaction networks were generated using the STRING software version 10.5 (Szklarczyk et al., 2015). A list of proteins found in the proteomics analysis were analysed in the software to show the known and predicted interactions under medium confidence settings.

1.2.17 *Secretome prediction analysis*

DPSCs transcriptomic data were submitted for secretome prediction analysis by using the online tool of the Vertebrate Secretome Database (VerSeDa) (Cortazar et al., 2017). The VerSeDa algorithms analyze the amino acid sequences, calculate the probability of secretion by classical or non-classical mechanisms, and return a list of predicted secretome. All default settings were used in our analysis.

1.3 RESULTS OF DPSC CHARACTERIZATION

1.3.1 *Previously identified MSC markers are differentially expressed across DPSC lines generated from patients*

We isolated DPSCs from dental pulp extracted from the human third molars or surgically obtained deciduous teeth of 300 patients (Figure 1.1). Some of the samples were used to optimize the protocol by identifying the window of time at which the samples could be stored in DMEM media (4°C) prior to DPSCs isolation, without loss of DPSCs viability. The samples that took more than 20 days to reach confluence for the first passage were considered unviable. We observed that the percentage of viability and proliferation capacity of the cells decreased substantially when the pulp isolation was delayed for more than 2 days after extraction of the tooth.

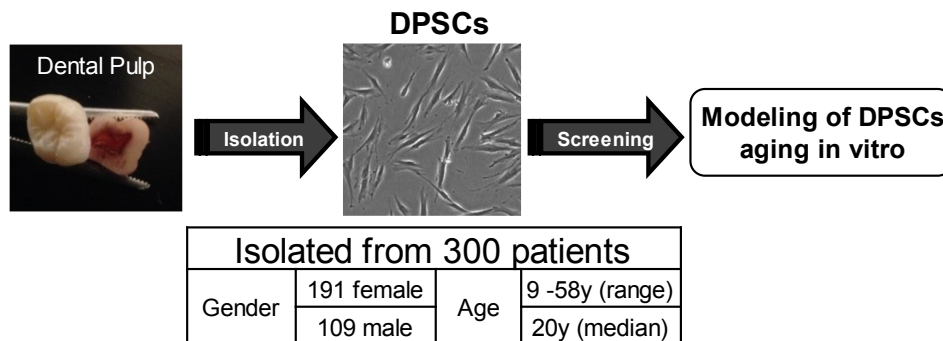


Figure 1.1. Extraction summary.

[A simplified summary of the isolated DPSC lines and the initial project design to model DPSCs aging in vitro.]

The DPSCs were expanded and passaged at least twice before protein isolation or cell harvest. Western blot analysis of previously identified MSC surface markers (CD29 and CD146, (Lv et al., 2014)) were used as a means of preliminary molecular screening. We observed heterogeneity in the expression pattern of these markers (Figure 1.2). A candidate set of DPSCs (DPSC 29, 43, 44, 45), which showed mid-level expression of the CD29 and CD146 markers were

selected for further analysis. We used this subgroup to test if DPSC with similar CD29 and 146 levels might show different kinetics of senescence in vitro. Differential potential for replicative capacity would give us tools to analyse the process in detail.

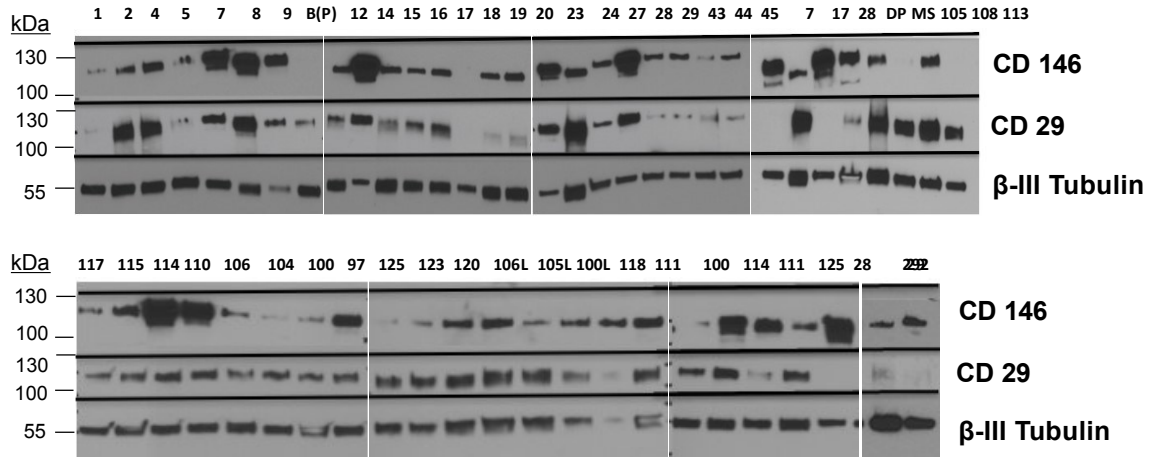


Figure 1.2. Preliminary screening.

[Preliminary screening of cell lines with cell surface markers, CD29 and CD146 using western blot shows differential expression of these markers.]

To know the actual percentage of mesenchymal cells present in the cell lines, the candidate DPSC cell lines along with commercial DPSCs and MSCs (Lonza) were analysed by flow cytometry. The results showed that our population of DPSCs had high percentage of CD29 & CD146, CD44 and Stro-1 double positive cells; 81.1%, 81.1%, 74.1% and 75.6% of CD29+146+ (Figure 1.3.A) and 77.5%, 68.5%, 59.3%, 58.5% of CD44+Stro-1+ (Figure 1.3.B) cells in DPSC 29, 44, 43 and 45, comparable to 78.8% and 75.6% of double positive cells in commercial DPSC. The results validate our isolation protocol and infer that our stem cell lines have high percentage of mesenchymal cells (Figure 1.3.C).

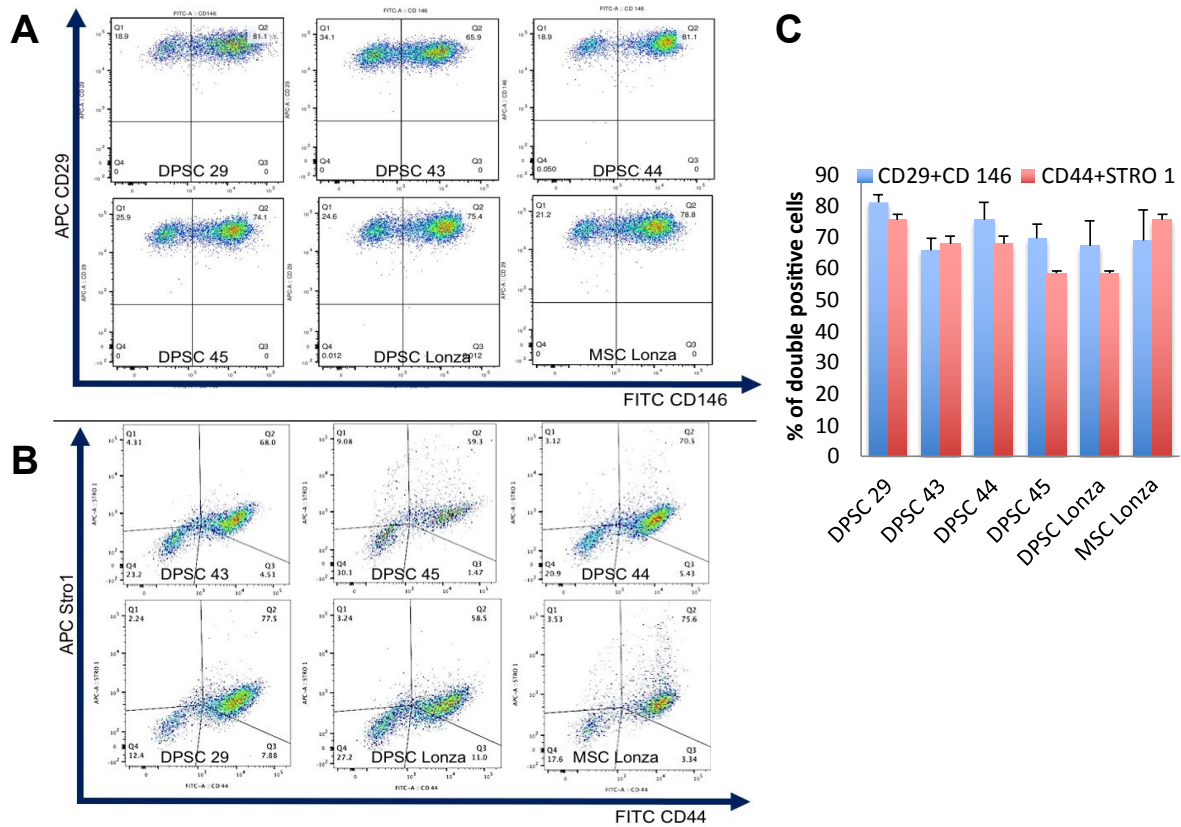


Figure 1.3. Fluorescent cytometry.

[Fluorescent cytometry of candidate cell lines (DPSC 29,44,43,45) demonstrates high percentage of mesenchymal markers; CD29+CD146+ cells (A) and CD44+Stro1+ cells (B). A representative graph shows that the percentage of “double positive” were comparable with commercial DPSC and MSC cell lines from Lonza® (C). (n = 3 per cell line). Graph error bars are the means ± standard error of the mean (SEM).]

1.3.2 *Rapid and slow aging DPSC cell lines*

In order to study the onset of aging in DPSCs we assessed the proliferation capacity of the cell lines through multiple passages. Interestingly we found dramatic differences between the DPSC lines extracted from different individuals. We found that DPSC 29, 44 and commercial DPSC showed minimal changes in proliferation capacity whereas DPSC 43 and 45 exhibited a dramatic decrease in proliferation with progressive cell divisions (Figure 1.4.A). The difference in the decrease in proliferation capacity was not caused by the donor age since the analysed cell lines (DPSC 29, 44, 43 and 45) were all isolated from individuals with similar age (21-23 years old). Based on the rate these cell lines reached replicative senescence they were classified into slow aging (SA: DPSC 29 and 44) and rapid aging cell lines (RA: DPSC 43 and 45). One of the manifestations of senesced cells is an increase in cell size (Oja et al., 2018), therefore we measured the surface area of DPSC 45, and noted a significant (4fold; $p < 0.0001$) increase in average cell size between early passage (P6) and late passage (P17), supporting DPSC 45 senescence during this time period (Figure 1.4.B). However, DPSC 44 showed no significant change in cell size between early passage (P6) and late passage (P16), correlating well with our classification as slow aging cell line. We further analysed the cell lines by measuring the activity of senescence-associated β -galactosidase (SA- β -gal) (Dimri et al., 1995) in a flow cytometric based assay (Figure 1.4.C). Two populations were observed in DPSC 44 early passage (P7) with SA- β -gal assay. At later passage (P18) in DPSC 44, most of the cells expressed SA- β -gal at high intensity indicating that the previous two populations reached senescence by this stage. In DPSC 45, both early (P8) and late (P18) passage cells showed high intensity of SA- β -gal suggesting that senescence starts early in rapid aging cell lines.

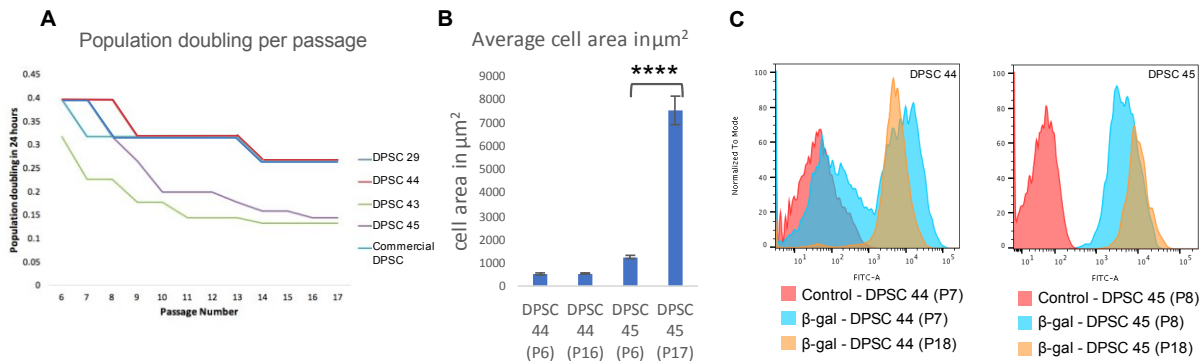


Figure 1.4. Difference in growth kinetics within the candidate cell lines

(A) Number of population doublings in 24 hours calculated in each consecutive passage indicates that two of the candidate cell lines demonstrated replicative senescence which is a classical hallmark of *in vitro* ageing (Cells were passaged to a density of 1:3 in each passage). (B) Quantification of average cell surface area in early and late passages of DPSC 44 and 45. Significance was determined by unpaired Student's t-test; $n = 70$ cells per cell line were measured; **** $p < 0.0001$; Graph error bars are the means \pm SEM (C) flow cytometric analysis of senescence-associated- β -gal activity in early and late passages of DPSC 44 and 45.

1.3.3 DPSC lines are heterogeneous in their differentiation capacities

The multipotency of an adult stem cell can only be gauged by its ability to differentiate into multiple lineages. To analyse the multipotency of the isolated cell lines, the candidate cell lines were pushed towards adipogenic and osteo/odontogenic lineages. The cells were cultured in differentiation media for a time period of 7 days for adipogenesis and 10 days for osteogenesis/odontogenesis (Figure 1.5.A). The differentiation was then quantified using a cell number normalized assay or qPCR (Figure 1.5B-G). Osteogenesis/odontogenesis was quantified based on the staining of extracellular calcification by alizarin red. We observed comparable

osteogenic/odontoblastic differentiation between the selected candidate DPSC lines (DPSC 29, 44, and 45). However, DPSC 43 did not survive the osteogenic/odontoblastic differentiation despite many repeated trials (Figure 1.5.B). An analogous experiment for adipogenesis was quantified based on the staining of neutral lipid vesicles by oil red O stain. This analysis showed that all of our candidate DPSC lines (DPSC 29, 44, 43, 45) differentiated into the adipogenic lineage, similarly to the commercial control DPSC line (Figure 1.5.C).

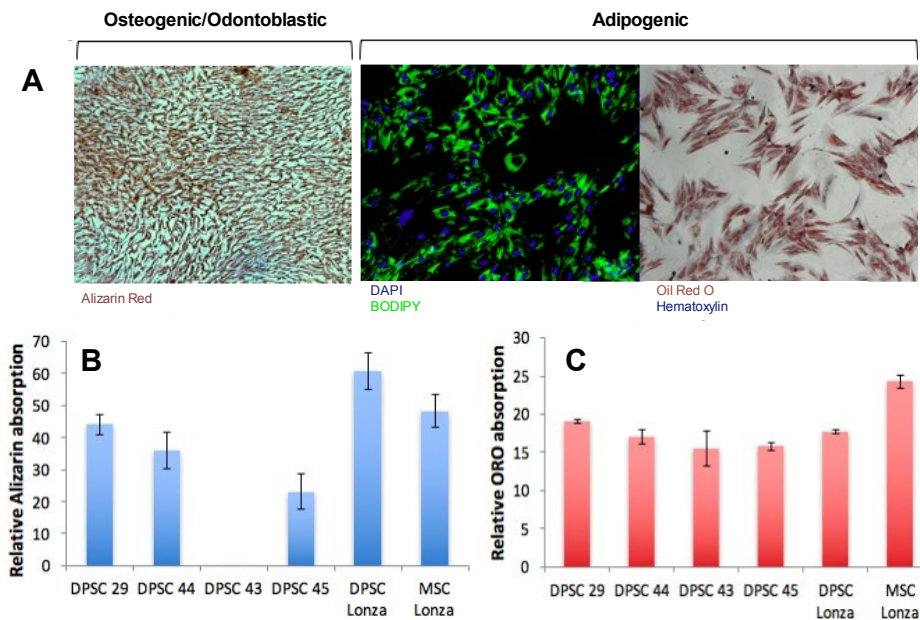


Figure 1.5. Osteo/odontogenic and Adipogenic potential of DPSCs.

(A) Osteo/odontogenic cells were stained for extracellular calcifications with Alizarin red stain. Adipogenic cells were stained for neutral lipids with BODIPY and Oil Red O stain. (B) Spectrometric quantification of Alizarin stain normalized with cell numbers (DAPI staining) showing all the candidate cell lines were able to differentiate into osteoblasts/odontoblast at different levels except DPSC 43 which did not survive the osteogenic differentiation. (C) Spectrometric quantification of Oil Red O stain normalized with cell numbers (DAPI staining) showing all the cell lines were able to differentiate into adipocytes at different levels and are highly resembling the differentiation levels of commercial cell lines.

In an attempt to normalize the heterogeneity in differentiation, we studied the effect of a short term (4 days) treatment of the cells with a TeSR media supplemented with a metabolite-cocktail (TeSRmeta) containing kynurenine (KY) and methylnicotinamide (MNA), which was previously shown to be beneficial to stem cells 29. While this treatment did not show a significant increase in differentiation in most of the DPSC lines, TeSRmeta treated DPSC 43 did show a dramatic increase in the osteogenic/odontoblastic differentiation (Figure 1.6.A-D). The molecular mechanism underlying this phenomenon is a topic of further investigation. Since many of the original lines had variation in the CD146 expression (Figure 1.2), we also differentiated two cell lines with either no CD146 expression (DPSC 105) or high level of CD146 expression (DPSC 28). We observed that the cells with the former phenotype showed minimal differentiation capacity. Though the expression levels of CD146 was not coercive to differentiation of a cell type, complete absence of CD146 led to impaired differentiation ability in both osteogenic/odontogenic and adipogenic differentiation test (Figure 1.6.C-D). We also examined Runx2 (osteoblast/odontoblast marker) and LPL (adipogenic marker) expression levels in differentiated cells (Figure 1.6.E-F) (Graneli et al., 2014; Jang et al., 2016). Taken together, our data showed that the analysed DPSC lines were able to differentiate into adipogenic and osteogenic/odontoblastic lineages.

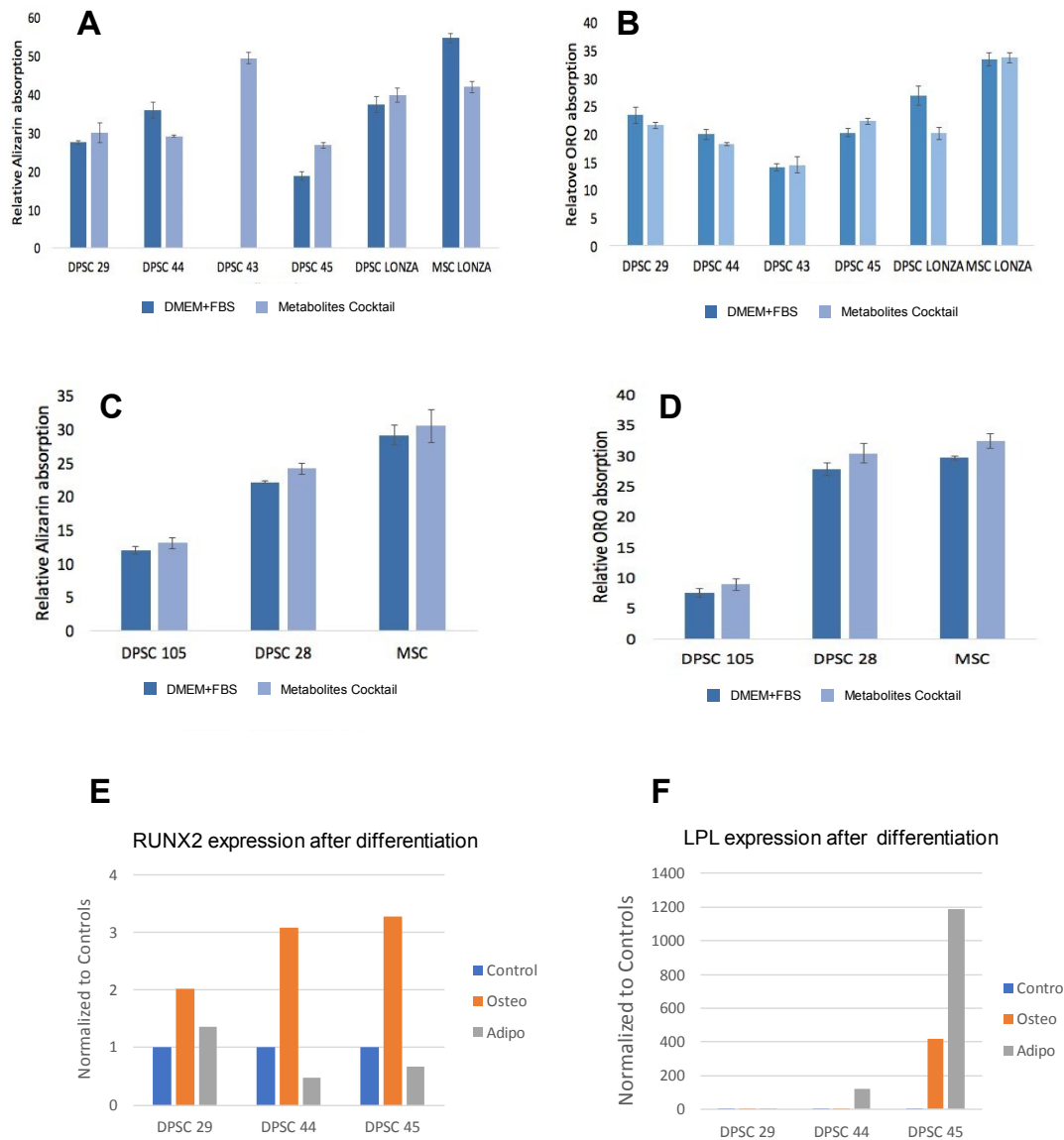


Figure 1.6. TeSR cocktail rescue DPSC 43.

(A-E) Treatment with TeSR cocktail for 4 days did not impact on the differentiation potential of the candidate cell lines, except for DPSC 43 in which it enhanced the survivability and differentiation to osteoblasts/odontoblasts. (n = 3 per cell line). Graph error bars are the means \pm SEM. (E and F) Quantitative PCR reveals the expression of differentiation markers: (E) Runx2, which marks early osteo/odontogenesis, (F) Lipoprotein lipase (LPL), which mark adipogenesis.

1.3.4 DPSCs exhibit a unique transcriptome profile

Transcriptome analysis was performed to identify important genes specifically expressed in adult DPSCs. To achieve this goal, we systematically compared the gene expression signature between embryonic stem cells (hESCs) and adult stem cells derived from bone marrow and dental pulp (MSCs and DPSCs) (Figure 1.7.A). Similarly, the adult MSCs and DPSCs were compared with human skin fibroblasts (Figure 1.7.B) to identify the genes that may be responsible for the stem cell properties of these cells. Finally, the DPSCs were compared with bone marrow MSCs (Figure 1.8.C) to dissect the unique genes expressed in DPSCs. The genes with false discovery rate <0.1 and fold change >1.5 were considered as differentially expressed. Principal component analysis (PCA) indicated that the candidate DPSC cell lines clearly segregated from hESCs and co-localized with MSCs (Figure 1.7.A). PCA with skin fibroblasts, MSCs and DPSCs indicated clustering within cell types (MSCs and DPSCs separated from fibroblasts) with minimal sample to sample variability (Figure 1.7.B).

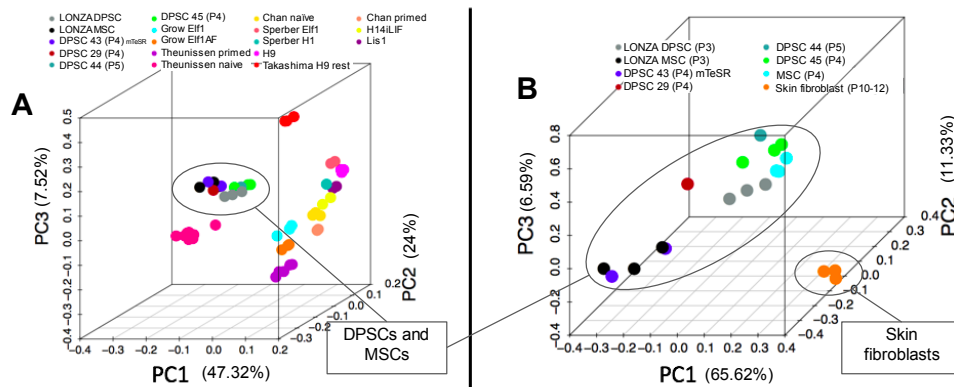


Figure 1.7. Transcriptome of DPSCs compared to BM-MSC, Fibroblasts and hESCs.

(A) Principal component analysis (PCA) of DPSCs, MSCs and hESCs showed that DPSCs and MSC grouped together. (B) Principal component analysis (PCA) of DPSCs with skin fibroblasts and MSCs from literature showed that DPSCs have distinct expression profiles from foreskin fibroblasts.

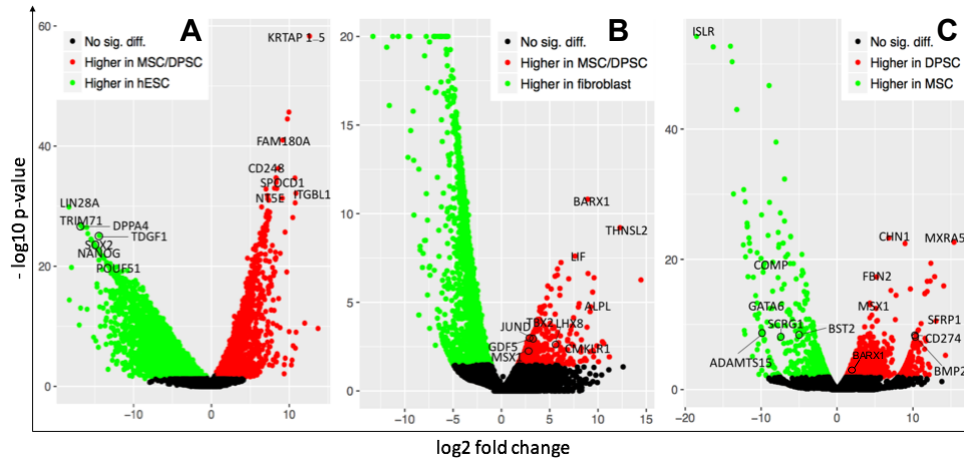


Figure 1.8. Differential expression between DPSCs, BM-MSC, Fibroblasts and hESCs.

(A) Volcano plot of genes differentially expressed in MSC/DPSCs vs. hESCs. (B) Volcano plot of genes differentially expressed in MSC/DPSC compared to fibroblasts. (C) Volcano plot of genes differentially expressed in DPSCs vs. MSC.

The comparison between hESCs and MSCs/DPSCs identified MSCs/DPSCs enriched genes, including MSC surface markers CD248 (Endosialin), CD73 (ecto-5'-nucleotidase), CD29 (ITGB1, Integrin beta 1), (Camilleri et al., 2016; T et al., 2016) (Figure 1.8.A, Table 1.5). We further compared our data between MSCs/DPSCs and human skin fibroblasts which revealed differentially expressed genes, such as ALPL (Alkaline Phosphatase) and GDF5 (Growth Differentiation Factor 5) which promote mineralization and osteogenic potential (Goto et al., 2016; Shimaoka et al., 2004), as well as negative regulators of cellular senescence TBX2 and JUND (Wang et al., 2012; Weitzman et al., 2000) (Wang *et al.*, 2012; Weitzman *et al.*, 2000) (Figure 1.8.B, Table 1.6). Furthermore, the comparison between DPSCs and BM-MSCs revealed the unique genes expressed in DPSCs (Figure 1.8.C,

Table 1.7). Interestingly, both MSX1, a protein responsible for osteogenic differentiation of DPSCs (Goto *et al.*, 2016), and BARX1 (BARX Homeobox 1), a gene primarily known for its role in patterning of teeth (Matthews *et al.*, 2016; Miletich and Sharpe, 2004; Miletich *et al.*, 2011; Tucker *et al.*, 1998) were differentially up-regulated in DPSCs compared to either fibroblasts, hESCs or BM-MSCs. No genome wide transcriptomic differences were observed between SA and RA DPSCs.

Table 1.5. Differentially expressed genes in ESC vs MSC/DPSC

HIGHLY EXPRESSED IN	Gene Symbol	Gene Name	Description
EMBRYONIC STEM CELLS (ESCs)	TDGF1	Teratocarcinoma Derived Growth Factor 1	Embryonic marker (Fang <i>et al.</i> , 2005)
	SOX2	Sex Determining Region Y-Box 2	Embryonic marker (Fang <i>et al.</i> , 2005)
	NANOG	Homeobox Transcription Factor Nanog	Embryonic marker (Fang <i>et al.</i> , 2005)
	POUF51	POU Class 5 Homeobox 1	Embryonic marker (Fang <i>et al.</i> , 2005)
	LIN28A	Zinc Finger CCHC Domain-Containing Protein 1	Let 7 associated protein responsible for growth and metabolism in ESCs (Shyh-Chang and Daley, 2013)
	TRIM71	Tripartite Motif Containing 71	RNA binding protein important for pluripotency (Ye and Belloch, 2014)
	DPPA4	Developmental Pluripotency Associated 4	Involved in the maintenance of pluripotency in stem cells (Tung <i>et al.</i> , 2013)
Mesenchymal Stem cells (MSC/DPSC)	CD248	Endosialin	Mesenchymal marker (Camilleri <i>et al.</i> , 2016)
	CD73	ecto-5'-nucleotidase	Mesenchymal marker (T <i>et al.</i> , 2016)
	CD29 (ITGB1)	Integrin beta 1	Mesenchymal marker (T <i>et al.</i> , 2016)
	KRTAP 1-5	Keratin Associated Protein 1-5	expression increase after actin depolarization and can alter differentiation capacities of MSC (Chang <i>et al.</i> , 2014)
	FAM180A	Family with Sequence Similarity 180 Member A	Observed in MSCs and <i>in vitro</i> progenies (Ghazanfari <i>et al.</i> , 2017)
	SPOCD1	SPOC Domain Containing 1	Gene involved in cell proliferation (Liang <i>et al.</i> , 2018)

Table 1.6. Genes over-expressed in MSC/DPSC compared to Fibroblasts

HIGHLY EXPRESSED IN	Gene Symbol	Gene Name	Description
MSC/DPSC	BARX1	BarH-Like Homeobox 1	Role in patterning of teeth (Graneli <i>et al.</i> , 2014; Jang <i>et al.</i> , 2016; Miletich and Sharpe, 2004)
	LIF	Leukemia Inhibitory Factor	member of the IL-6 cytokine family that activate STAT3(Cherepkova <i>et al.</i> , 2016; Onishi and Zandstra, 2015)
	ALPL	Alkaline Phosphatase	Bone mineralization (Goto <i>et al.</i> , 2016)
	TBX2	T- Box 2	DNA binding protein responsible for epithelial to mesenchymal transition (Wang <i>et al.</i> , 2012)
	JUND	Transcription Factor Jun-D	Protects against P53 dependent senescence and apoptosis (Weitzman <i>et al.</i> , 2000)
	GDF5	Growth Differentiation Factor 5	Promotes osteogenic potential of bone marrow mesenchymal stem cells (Shimaoka <i>et al.</i> , 2004)
	MSX1	Msh Homeobox 1	Protein associated with osteogenesis and odontogenesis of DPSCs (Goto <i>et al.</i> , 2016)
	CMKLR1	Chemerin Chemokine-Like Receptor 1	Involved in osteogenesis and adipogenesis of bone marrow stem cells (Muruganandan <i>et al.</i> , 2010)

Table 1.7. Differentially expressed genes in MSC vs DPSC

HIGHLY EXPRESSED IN	Gene Symbol	Gene Name	Description
MSCs	COMP	Cartilage Oligomeric Matrix Protein	Enhances matrix assembly during chondrogenesis (Haleem-Smith <i>et al.</i> , 2012)
	GATA6	GATA Binding Protein 6	Involved in differentiation of ESCs (Fujikura <i>et al.</i> , 2002)
	ADAMTS15	ADAM Metallopeptidase with Thrombospondin Type 1 Motif 15	Skeletal Muscle development
	SCRG1	Stimulator Of Chondrogenesis 1	Involved in self-renewal, migration, and osteogenic differentiation potential in mesenchymal stem cells (Aomatsu <i>et al.</i> , 2014)
	BST2	Bone Marrow Stromal Cell Antigen 2	Bone marrow stem cells marker enriched in MSCs (Aomatsu <i>et al.</i> , 2014)
DPSCs	CHN1	Chimerin 1	Predominantly expressed in neurons
	MXRA5	Matrix Remodeling Associated 5	Predominantly expressed in multiple cancer cells
	FBN2	Fibrillin 2	Regulates osteoblast supported osteoclasts (Nistala <i>et al.</i> , 2010)
	MSX1	Homeobox Protein Hox-7	Protein responsible for osteogenic and odontogenic differentiation of DPSCs (Goto <i>et al.</i> , 2016)
	SFRP1	Secreted Frizzled Related Protein 1	Protein responsible for maintenance of hematopoietic mesenchymal stem cells (Renstrom <i>et al.</i> , 2009)
	BMP2	Bone Morphogenetic Protein 2	Plays central role in osteoblast differentiation
	CD274	B7 Homolog 1	Novel mesenchymal marker (Camilleri <i>et al.</i> , 2016)

1.3.5 *BARX1 as a DPSCs marker*

The differentially expressed gene in DPSCs compared to fibroblasts, BARX1 (Figure 1.8.C) is a transcription factor, part of the homeobox gene group responsible for early developmental patterning involving craniofacial development, teeth primordia and stomach specification from gut endoderm (Sperber and Dawid, 2008) and repression of cell migration in the context of cancer (Wang et al., 2017).

To validate the RNA-seq results, we analysed BARX1 transcript and protein expression with RT-qPCR and immunofluorescence. The Barx1 antibody was validated on HeLa cells transfected with BARX1 overexpression vector. We next performed BARX1 immunofluorescence staining for DPSCs 29, DPSCs 292 and human skin fibroblasts (HFF-1) cell lines (Figure 1.9). Our results showed that Barx1 was localized in the nuclei of DPSCs as a punctate pattern, suggesting that Barx1 binds to specific chromosomal locations (Figure 1.9.B, C, E and F). Importantly, skin fibroblasts showed no nuclear Barx1 protein signal in immunofluorescence (Figure 1.9.A and D) and BM-MSCs (Lonza) expressed a low level of Barx1 (Figure 1.10.A). The Barx1 transcript qPCR analysis supported the finding; DPSCs show Barx1 expression while fibroblasts do not express BARX1 gene (Figure 1.10.B). These data suggest that BARX1 is a DPSCs marker that can discriminate against fibroblast population.

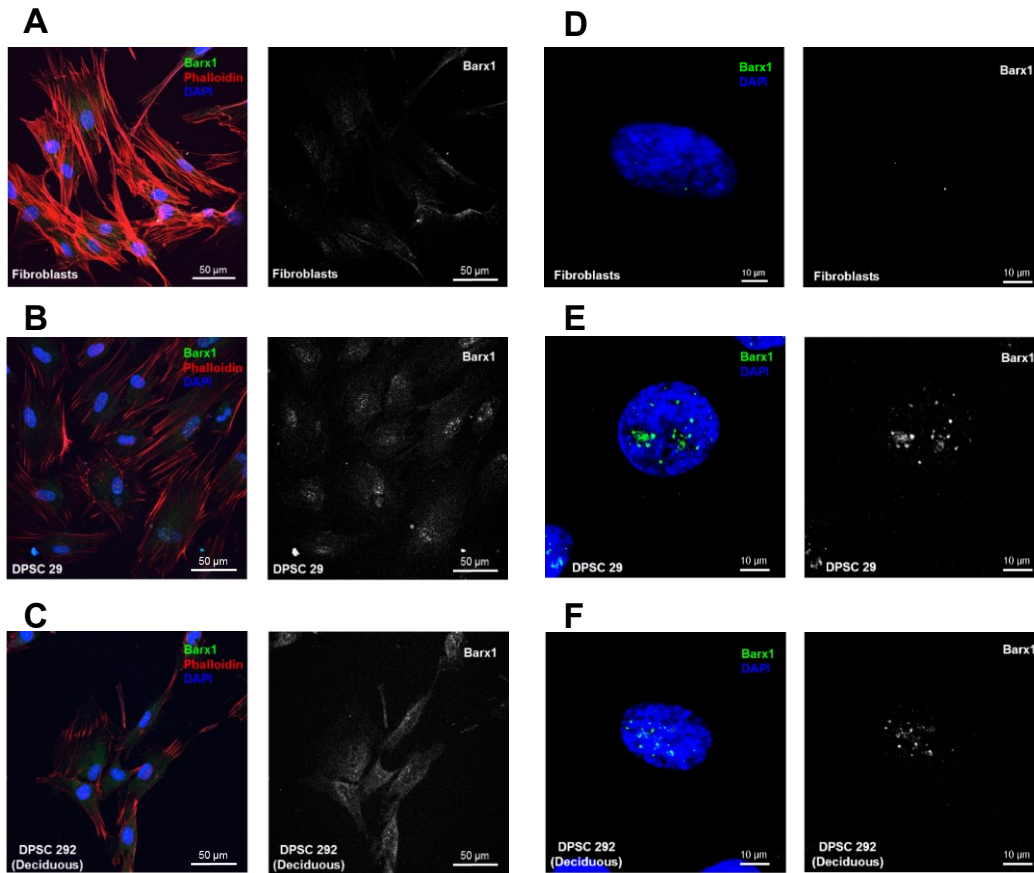


Figure 1.9. BARX1 gene as a new specific marker for DPSCs

(A-C) Immunofluorescent staining of Barx1 in skin fibroblasts, adult DPSCs (DPSC 29), and deciduous DPSCs (DPSC 292) at low power magnification. (D-F) Showing the nuclear localization of Barx1 transcription factor at high power magnification. Exposure settings and laser intensity of the confocal microscope were adjusted and normalized for fibroblasts, and same settings were used for the DPSCs.

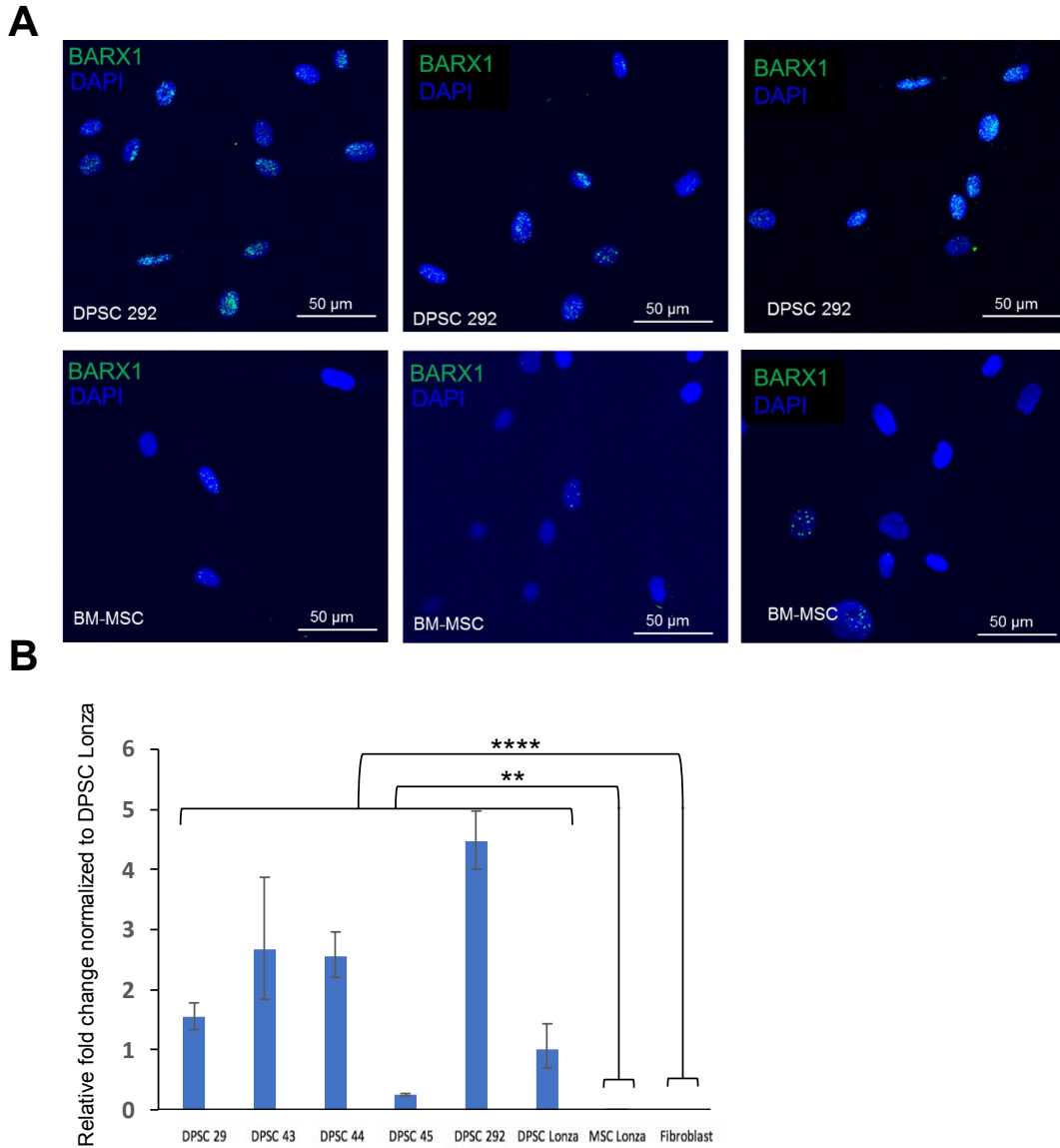


Figure 1.10. BARX1 is not highly expressed in BM-MSCs.

(A) Immunofluorescent staining of Barx1 in DPSC 292 and BM-MSCs Lonza. Exposure settings and laser intensity of the confocal microscope were adjusted for DPSC 292. (B) Quantitative PCR reveals absence of BARX1 gene in BM-MSCs and in skin fibroblasts. Significance was determined by unpaired Student's t-test; $n = 3-6$ per cell line; $**p < 0.01$; $****p < 0.0001$; Graph error bars are the means \pm SEM

1.3.6 *Metabolic signature, predictive of the rapid aging*

Recent work has revealed that cellular metabolism plays other vital roles beyond simply the production of energy. In some situations, metabolism is shown to regulate cellular fate (Mathieu and Ruohola-Baker, 2017). While pluripotent stem cells can switch their metabolic requirements to facilitate cellular changes and hematopoietic stem cells are regulated by metabolic changes (Mathieu and Ruohola-Baker, 2017; Snoeck, 2018), very little is known about adult DPSCs metabolism, and if they utilize metabolism beyond cellular energy production. To analyse the metabolic signature of DPSCs, we used the Seahorse platform to study various metabolic aspects of these cells. The mitostress assay done by uncoupling the electron transport chain (ETC) and ATP synthase and treating the mitochondria with FCCP revealed that the maximum mitochondrial oxygen consumption rate (OCR) was higher in adult DPSCs than hESCs (Figure 1.11.A, B). The DPSC's ability to use lipids as an energy source was measured by an increase in OCR with the presentation of palmitate as an energy substrate (Figure 1.11.C, D). Their glycolytic capacity was assessed by measuring the extracellular acidification rate (ECAR) of the DPSCs after addition of glucose and thereafter treating the cells with a glucose analogue, 2Deoxy-D-glucose (2DG) to block glycolysis (Figure 1.12.B). The results showed that DPSCs were capable of utilizing both fatty acids and glucose as fuel for ATP production (Figure 1.11.C; Figure 1.12.A). However, interestingly, the RA cell lines DPSC lines 43 and 45 showed significant reduction in the utilization of fatty acids and glucose as energy sources compared to SA DPSC lines 29 and 44 (Figure 1.11.C; Figure 1.12.A). While the candidate cell line included in this study showed comparable level of MSC markers CD146, and CD29, we wanted to address the potential correlation of these markers and the metabolic profile. We selected two more cell lines at random that showed higher expression than original candidate lines. We found that DPSC 125 that

expresses CD29 at a higher level, and DPSC 120 that expresses both CD29 and CD146 at higher level showed similar capacity to utilize glucose as commercial DPSC Lonza (Figure 1.12.C).

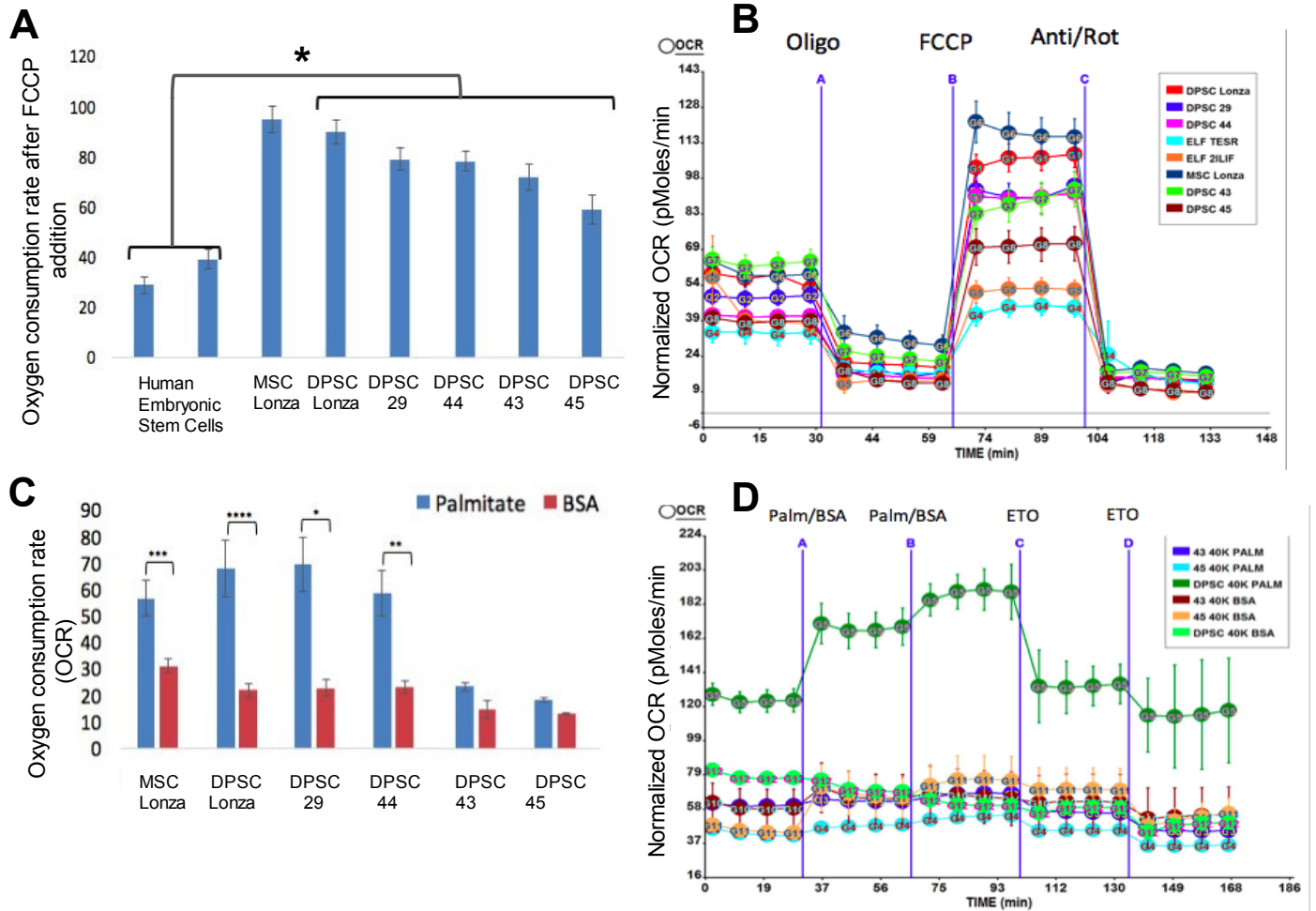


Figure 1.11. Metabolic assays.

(A, B) Mitostress Assay shows that DPSCs have higher mitochondrial activity than human embryonic stem cells (* $p=0.002$). (C, D) From the selected candidate cell lines, DPSC 29 and 44 use palmitate inferring their ability to use fatty acid as an energy source. DPSC 43 and 45 have lower ability to use fatty acid as an energy source. Significance was determined by unpaired Student's t-test; $n = 3-12$ per cell line; * $p < 0.05$; ** $p < 0.01$; *** $p < 0.001$; **** $p < 0.0001$; Graph error bars are the means \pm SEM.

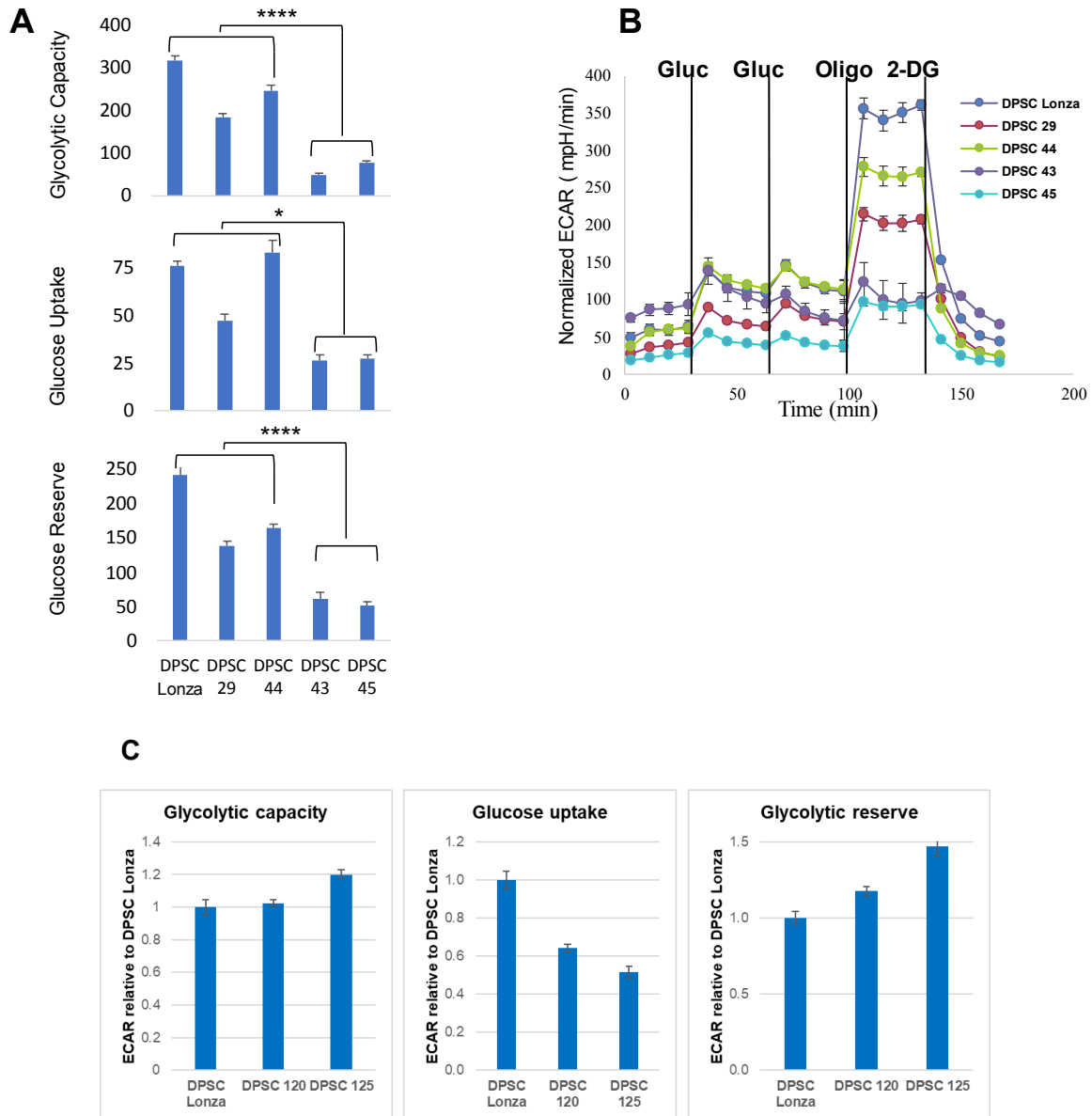


Figure 1.12. Glycolysis assay on candidate DPSCs.

(A, B) Glycolysis stress assay conducted on the selected candidates shows that DPSC 43 and 45 have significantly lower glycolytic capacity compared to DPSC 29, 44 and commercial DPSCs.

(C) Representative graphs for glucose stress assay of DPSC 120 and DPSC 125 inferring that they were able to use glucose as a source of energy normally compared to DPSC Lonza. Graph error bars are the means \pm SEM. Significance was determined by unpaired Student's t-test; n =

3-12 per cell line; * $p < 0.05$; ** $p < 0.01$; *** $p < 0.001$; **** $p < 0.0001$.

1.3.7 Rapid aging DPSC cell lines showed increase in TGF-beta pathway activity and upregulation of cytoskeletal regulators

To better understand the differences between the slow aging (SA: DPSC 29 and 44) and rapid aging cell lines (RA: DPSC 43 and 45) we analysed the proteomes of young/early passage (p3) and old/late passage (p17) cells of each class (Figure 1.13.A). We examined the data for two markers that had been previously suggested to mark levels of replicative senescence (Oja *et al.*, 2018), CDKN2A (Cyclin Dependent Kinase Inhibitor 2A, and also known as P16) and CDKN1A (Cyclin Dependent Kinase Inhibitor 1A, and also known as p21). CDKN2A is reported to increase with senescence. Our proteomic data confirmed an increase of CDKN2A in both groups but more significantly with the rapid aging group ($p < 0.0001$) (Figure 1.13.B). CDKN1A is reported to reach its maximum at the onset of growth arrest and subsequently decrease with senescence (Oja *et al.*, 2018), and we noted a similar trend of downregulation in both senesced groups, but significantly more in rapid aging cell lines ($p = 0.0006$) (Figure 1.13.B). These markers support the different kinetics for senescence observed for DPSC 43/45 and DPSC 29/44.

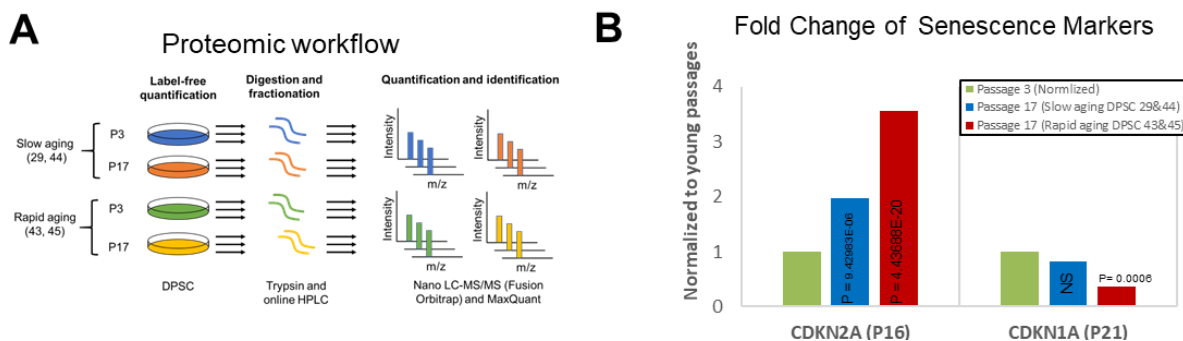


Figure 1.13. Proteomic analysis.

(A) Proteomic workflow used to identify differentially regulated protein expression in young (early passage) versus old (late passage) DPSC in rapid aging (lines 43, 45) or slow aging (lines 29, 44) cells. (B) Fold changes of replicative senescence markers, CDKN2A and CDKN1A in late passages of rapid aging cell lines (43 & 45) and slow aging cell lines (29 & 44).

Unbiased GO-term analysis of the proteomic data showed significant enrichment of muscle contraction proteins, such as ACTN2 (Actinin Alpha 2), MYH11 (Myosin Heavy Chain 11, Smooth Muscle Isoform) and CNN1 (Calponin 1, Basic, Smooth Muscle) (Figure 1.14.A-B) in rapid aging cell lines (DPSC 43,45) when comparing the changes between late passage and early passage. Further analysis of the enriched muscle contraction proteins in String-analysis algorithm revealed the following functional clusters: cell junction regulators, actomyosin structure organization, focal adhesion, skeletal muscle contraction, smooth muscle contraction and calcium ion transport, all of which involved in controlling the cytoskeleton of the cells (Figure 1.15).

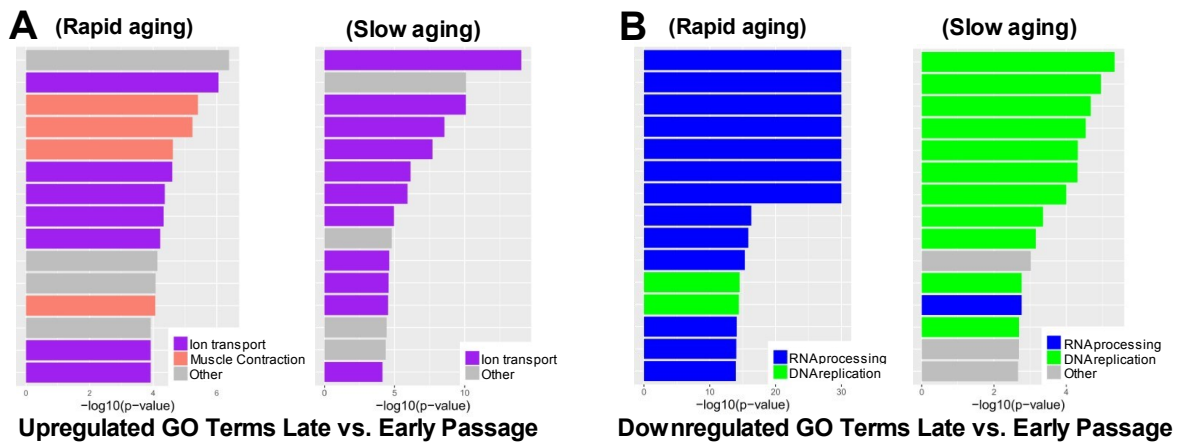


Figure 1.14. Go Term analysis.

Proteomics GO terms enrichment for slow aging (29 & 44) and rapid dividing (43 & 45) cell lines for upregulated terms (A) and downregulated term (B).

We hypothesized that the enrichment in muscle contraction proteins in rapid aging cells (RA-DPSC 43, 45) in late passages (p17), particularly the increase of the smooth muscle specific markers, CNN1 and MYH11, was an indication of differentiation towards myofibroblast-like cells (Kurpinski et al., 2010; Popova et al., 2010). It has been shown previously that fibroblasts (Desmouliere et al., 1993; Vaughan et al., 2000) or mesenchymal stem cells (Desai et al., 2014; El Agha et al., 2017) can differentiate into myofibroblast lineage when subjected to TGF- β pathway.

Therefore, we examined our proteomics data further for TGF- β pathway related genes and found that some of the TGF- β pathway related proteins are enriched in rapid aging cells compared to slow aging cells in early passages (Figure 1.16). These proteins were clustered by string software into two functional categories: TGF- β receptor signalling, and Integrin-mediated cell-substrate adhesion. Of particular interest is ITGB5 (Integrin, Beta 5), a receptor for fibronectin, that has been found to mediate actin stress fiber formation (Bianchi-Smiraglia et al., 2013) by activating the latent form of TGF- β complex (Sarrazy et al., 2014; Wipff and Hinz, 2008). We also found that TGFB2 (an isoform of the TGF- β ligand) and the myofibroblast marker ACTA2 (Rao et al., 2014) (also known as α -smooth muscle actin, α -SMA) were expressed at a higher level in the rapid aging cell lines compared to slow aging cell lines in early passages (Figure 1.16) indicating a possible autocrine activation of TGF- β at early passages. These data further support our hypothesis that in rapid aging RA-DPSCs, TGF- β pathway and its muscle contraction gene targets were upregulated leading to spontaneous terminal differentiation towards myofibroblast-like cells in later passages.

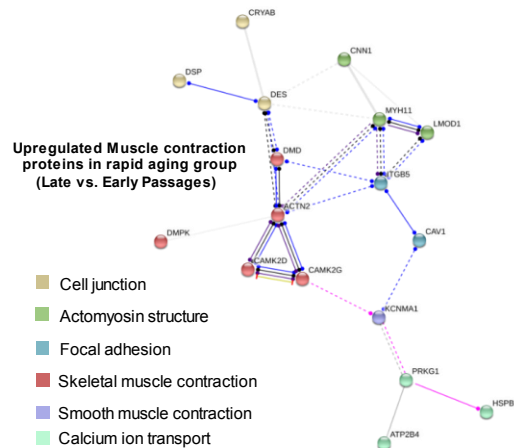


Figure 1.15. String analysis.

String analysis of enriched muscle contraction proteins expressed in late passages of rapid aging cell lines.

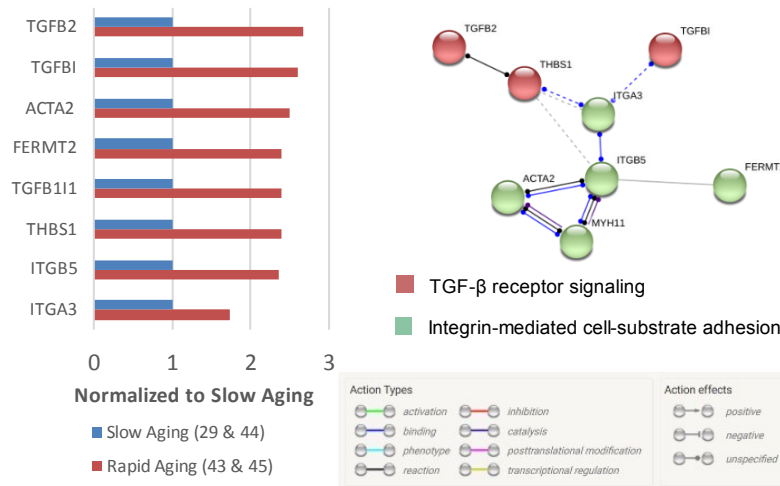


Figure 1.16. TGF- β pathway related proteins.

Fold change of TGF- β pathway related proteins higher in rapid aging compared to slow aging at early passages (P value <0.05) (left), and String analysis of TGFb pathway proteins expressed in early passages (P3) rapid aging cells at higher level than slow aging early passages (right).

1.3.8 *TGF β pathway activation induces stress fiber formation and correlates with rapid DPSCs aging*

To examine the possibility of an autocrine effect underlining the rapid aging phenotype, we analysed the predicted secretome of the young/early passage DPSCs, since secreted molecules can have an autocrine effect in long-term cultures (Wang et al., 2016). We used VerSeDa online tool (Cortazar *et al.*, 2017) to predict the secretome of young DPSCs based on the transcriptomic data. We first used all expressed genes across different DPSC lines (Figure 1.17.A). The result contained a set of four thousand genes of secreted or transmembrane proteins. We performed gene ontology (GO) enrichment analysis to have an overview of the biological processes involved in DPSCs secretome (Figure 1.17.B). Some of the top GO terms were “extracellular matrix organization”, “cell adhesion”, and “positive regulation of cell migration” marking proteins which

are expected to be in any MSCs secretome (Pires et al., 2016). More interestingly, the GO term “response to hypoxia” including genes such as VEGFA (vascular endothelial growth factor A), and VEGFB, might explain the DPSCs sensitivity to hypoxia, as previously reported (Ahmed et al., 2016). The GO term “semaphorin-plexin signalling pathway” which includes different families of semaphorin ligands & plexin receptors (Kruger et al., 2005) suggests that this pathway maybe used in DPSCs migration process towards the injury site (Sharpe, 2016). DPSCs are also expressing NGF (Nerve Growth Factor) as previously reported (Kolar et al., 2017).

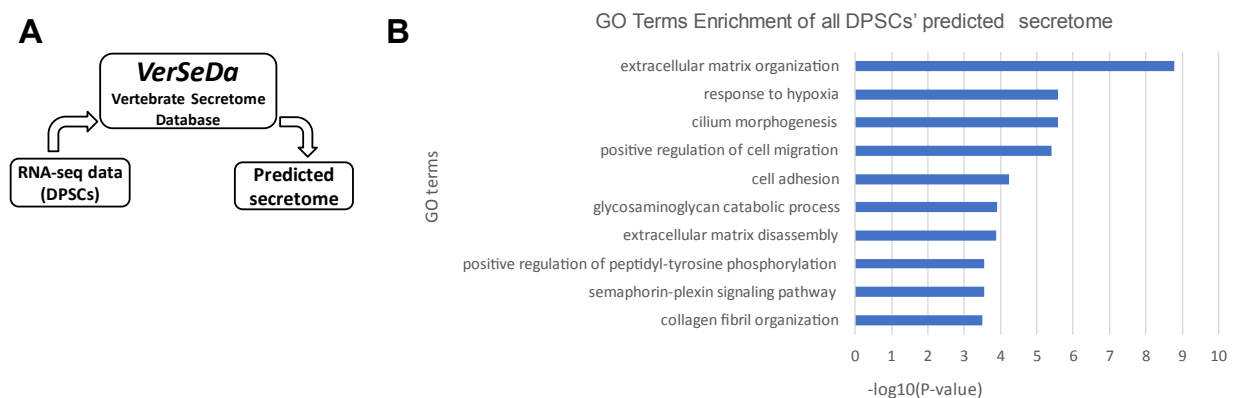


Figure 1.17. Secretome prediction.

(A) A simplified flowchart that shows the process of utilising VerSeDa secretome prediction utilities to analyse the predicted secretome in DPSC. (B) a) GO terms of biological processes enriched across different DPSC lines' predicted secretome.

We further performed GO term enrichment analysis between secretome genes up-regulated in SA and RA cell lines at early passages. Terms such as “axon guidance” and “cell migration” were upregulated in slow aging cells, which include genes for multiple semaphorin family proteins, as well as BMP4 (bone morphogenetic protein 4) (Figure 1.18.A). Semaphorin 3E (SEMA3E), Semaphorin 4D (SEMA4D) and Semaphorin 5A (SEMA5A) have been reported to inhibit focal adhesion by promoting the disassembly of integrin and actin stress fibers on multiple different cell

types including glia, platelets, different types of immune cells, and a number of cancer cell lines, as well as promoting proliferation and cell migration of endothelial cells (Aghajanian et al., 2014; Hung and Terman, 2011; Li et al., 2012; Sadanandam et al., 2010). BMP4 has been suggested to attenuate the effect of TGF- β 2 on the accumulation of extracellular matrix adhesion proteins and therefore aid in cell migration (Guo et al., 2012; Wordinger et al., 2007). In contrast, terms such as “cell adhesion” and “chondrocyte development” were upregulated in rapid aging cells which include aggrecan(ACAN), fibronectin, integrin & osteonectin (SPARC), all of which are reported to be up-regulated under TGF- β pathway activation (Choi et al., 2017; Desai *et al.*, 2014; Fujita et al., 2002; Ignatz and Massague, 1986; Lee et al., 2004; Reed et al., 1994; Shibata and Ishiyama, 2013; Warstat et al., 2010; Zamani et al., 2014) (Figure 1.18.B).

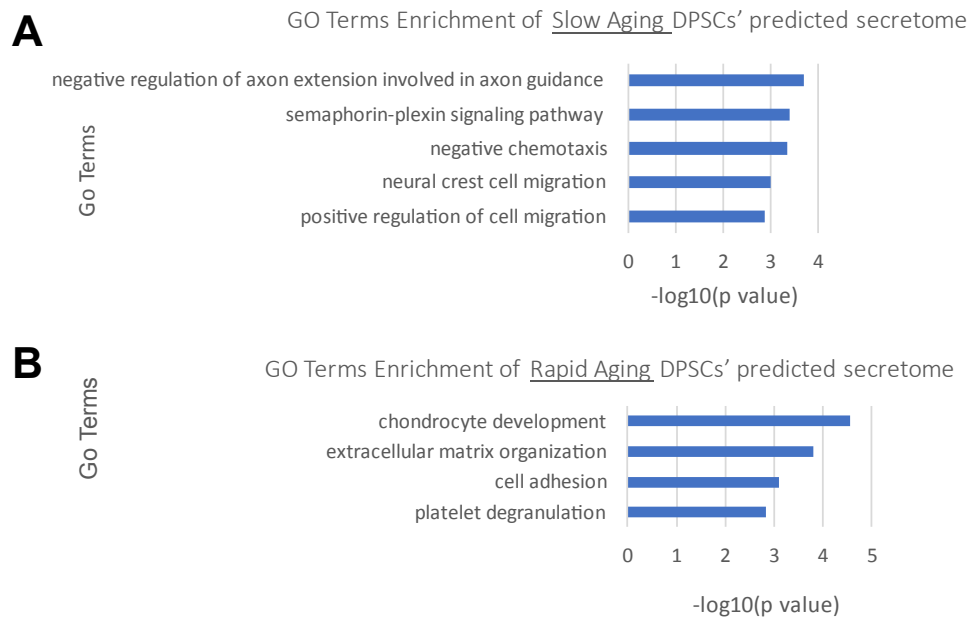


Figure 1.18. Secretome go terms

(A) GO terms of biological processes based on significantly upregulated genes in slow aging DPSCs predicted secretome compared to rapid aging lines. (B) GO terms of biological processes based on significantly upregulated genes in rapid aging DPSCs' predicted secretome compared to slow aging lines.

To further analyse the differences in the secretome between rapid aging cells and slow aging cells, we used Signalling Pathway Impact Analysis (SPIA) method (Tarca *et al.*, 2013), since signalling pathways in particular are closely related to secretome of MSCs (Dong *et al.*, 2017). SPIA analyses the differentially expressed genes and their log fold changes while taking into consideration the signalling pathway network topology from KEGG database (Kyoto Encyclopedia of Genes and Genomes), in order to identify pathways relatively activated or inhibited in a given set of genes. The results from SPIA confirm that TGF- β pathway, focal adhesion and regulation of actin cytoskeleton are activated at the transcriptomic level in rapid aging cells compared to slow aging (Figure 1.19), which is what we found at proteomic level as well.

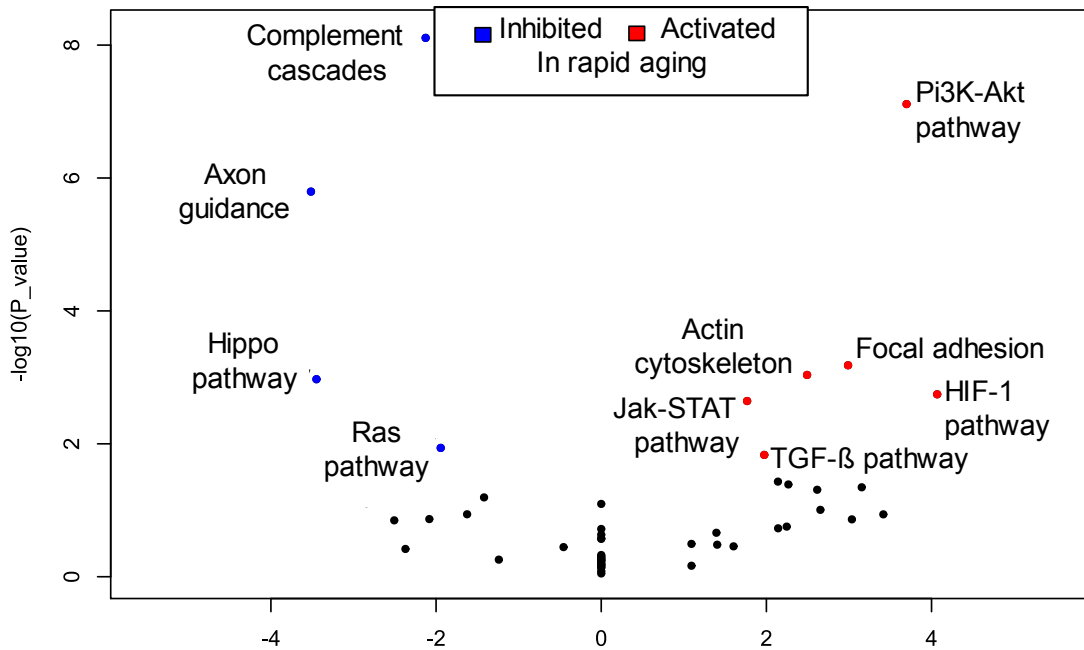


Figure 1.19. SPIA analysis

Signaling pathway impact analysis (SPIA) showing relatively activated or inhibited signaling pathways in rapid aging cell lines' predicted secretome compared to slow aging cell lines. (False discovery rate <0.1).

To test the function of TGF- β pathway for activating actin stress fibers in DPSCs, we treated the SA DPSCs with Activin, and found a significant increase in actin stress fibers in SA DPSCs (Figure 1.20.A-C). Similar stress fibers were previously observed in fibroblasts (Figure 1.9.A). These data show that TGF- β pathway activation is sufficient for actin stress fiber formation in SA DPSCs and suggest that TGF- β pathway activation in RA DPSC results in stress fiber formation and premature senescence. We tested this by quantifying the cells with stress fibers in RA late passage DPSCs (Figure 1.21.A-E). Importantly, we observed a significant increase in stress fiber formation in RA cells, later passages (P value =0.0001) (Figure 1.21.E). One of the inhibited pathways in RA cells is the Hippo pathway, which has been suggested to control cell proliferation of DPSCs (Tian et al., 2017). Therefore, low Hippo pathway activity and TGF- β induced stress fiber formation may explain the slow division rate in RA cells compared to SA cells.

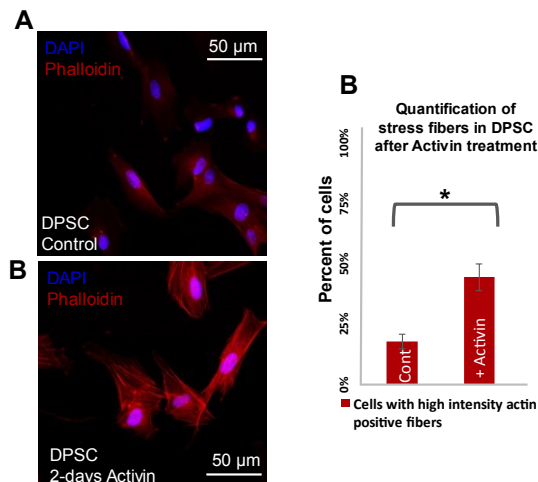


Figure 1.20. TGFb pathway control stress fibers in DPSCs.

(A, B) Activation of TGFb pathway by adding Activin to the DPSCs growth media for 2-days increases actin stress fiber formation (B), compared to control (A). (C) Quantification of stress fibers in DPSC Lonza in control, and after treating with Activin for 2-days. Significance was determined by unpaired Student's t-test; n = 100 cells were counted per condition; *p = 0.03; Graph error bars are the means \pm SEM.

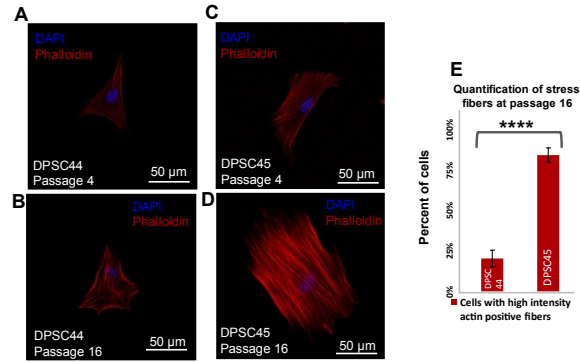


Figure 1.21. Stress fibers comparison between SA and RA.

(A-D) Representative confocal images of DPSC 44 and DPSC 45 comparing the size and intensity of the intensity actin fibers at passage 4, and passage 16. (B) Quantification of cells with senescence phenotype at passage 16 in DPSC 44 and DPSC 45. Significance was determined by unpaired Student's t-test; $n = 100$ cells were counted per condition; $*p = 0.0005$; Graph error bars are the means \pm SEM.

To further dissect the genes that contributed to the slow cell division, a transcriptome level analysis was performed comparing early passage slow vs. rapid aging cells. The genes which might be responsible for their aging and metabolic profile were identified (Figure 1.22, Table 1.8). Some of the key genes enriched in early passages of rapidly aging (RA) cell lines were cell cycle regulators. One of these genes, G0S2 is a G0/G1 switch protein also found to be associated with replicative senescence of human dermal fibroblasts (Yoon et al., 2004) and is known to maintain quiescence in hematopoietic cells (Yamada et al., 2012). Other enriched genes, GATA2 (GATA Binding Protein 2) and DDIT4 (DNA Damage Inducible Transcript 4) are also known to regulate quiescence in hematopoietic stem and progenitor cells (GATA2) (Tipping et al., 2009), or regulates mesenchymal stem cell fate through mTOR pathway (DDIT4) (Gharibi et al., 2016). Interestingly G0S2 blocks lipolysis through direct interaction and inhibition of triglyceride hydrolase activity of Adipose triglyceride lipase (Engin et al., 2017), and together with GATA2

are both regulated by PPAR- γ , connecting them to metabolic regulation. Interestingly, in the rapidly aging cell lines (RA-DPSC 43 and 45) the utilization of glucose or fatty acids as fuels for ATP production is significantly reduced compared to the SA cell lines, DPSC lines 29 and 44 (Figure 1.11.C; Figure 1.12.A). Importantly, this dramatic reduction in glycolytic capacity or fatty acid beta-oxidation was observed in DPSC 45 and 43 already at the early passages (P3). Therefore, the genes connected to metabolic regulation may be responsible for challenged lipid metabolism in rapidly aging cells and might promote terminal differentiation and thereby favour cellular senescence.

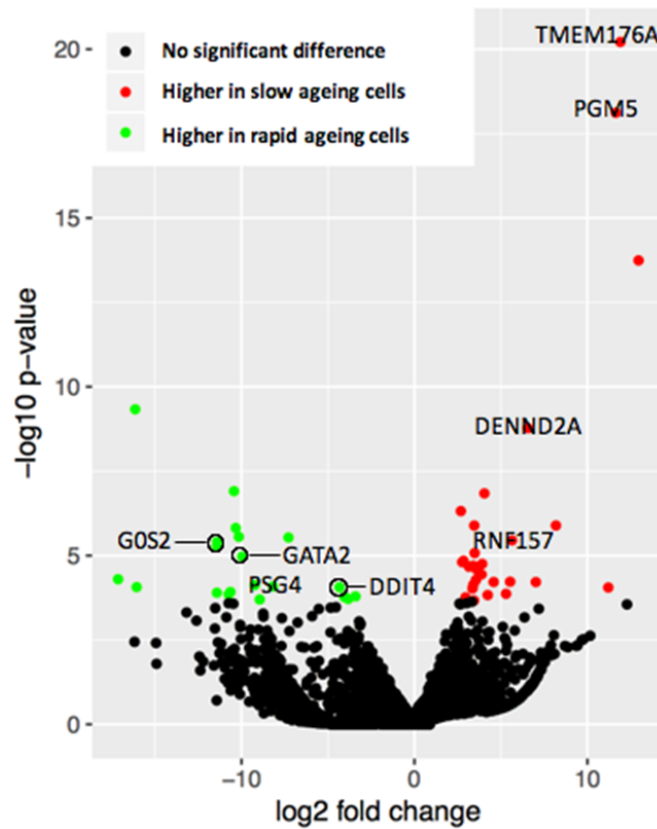


Figure 1.22. Differentially expressed genes in cells with slow aging phenotype.

Volcano plot of genes differentially expressed in cells with slow aging phenotype [DPSC 29 (P4) & DPSC 44 (P5)] compared to rapid aging phenotype [DPSC 43 & 45 (P4)].

Table 1.8. Differentially expressed genes in Rapid ageing vs Slow ageing phenotypes

HIGHLY EXPRESSED IN	Gene Symbol	Gene Name	Description
RAPIDLY AGEING CELLS	G0S2	G0/G1 Switch 2	Found to be associated with replicative senescence of human dermal fibroblasts (Yoon <i>et al.</i> , 2004)
	GATA2	GATA Binding Protein 2	known to regulate quiescence in hematopoietic stem and progenitor cells (Tipping <i>et al.</i> , 2009) (Endoh <i>et al.</i> , 2009)
	PSG4	Pregnancy Specific Beta-1-Glycoprotein 4	
	DDIT4	DNA Damage Inducible Transcript 4	DNA damage inducible protein which regulates mesenchymal stem cell fate (Gharibi <i>et al.</i> , 2016)
	CMKLR1	Chemerin Chemokine-Like Receptor 1	Involved in osteogenesis and adipogenesis of bone marrow stem cells (Muruganandan <i>et al.</i> , 2010)
Slow ageing cells	TMEM176 A&B	Transmembrane Protein 176 A&B	Present in neoplastic fibroblasts and cancer cells (Degnim <i>et al.</i> , 2012)
	PGM5	Phosphoglutamase 5	Lack enzymatic activity (Moiseeva <i>et al.</i> , 1996), but might have structural roles (Molt <i>et al.</i> , 2014)
	DENND2A	DENN Domain Containing 2A	MADD domain containing gene which is an apoptotic signal over expressed in neoplastic cells
	RFN157	Ring Finger protein 157	Maintain survival and morphology of cultured neuronal cells (Matz <i>et al.</i> , 2015)

1.4 DISCUSSION AND CONCLUSIONS

Here we studied the aging of dental pulp stem cells (DPSCs), a population of adult stem cells that is known to participate in the repair of an injured tooth. Using high throughput transcriptomic and proteomic analysis we identified markers for DPSC populations with accelerated replicative senescence. In particular, we show that the transforming growth factor-beta (TGF- β) pathway and the cytoskeletal proteins are upregulated in rapid aging DPSCs, indicating a loss of stem cell characteristics and spontaneous initiation of terminal differentiation. Using metabolic flux analysis, we identified a metabolic signature for the rapid aging DPSCs, prior to onset of the senescence phenotypes. This metabolic signature is therefore predictive for rapid DPSCs aging.

It has been shown that mesenchymal stem cells age during in vitro expansion and exhibit characteristic hallmarks of aging such as replicative senescence and decrease in telomerase length (Bonab et al., 2006). We studied the effects of in vitro aging in dental pulp stem cells and observed that DPSCs showed differences in the rate of replicative senescence. A proteomic analysis of rapid and slow aging cells revealed that genes responsible for muscle contraction were upregulated in rapid aging (late passage cells vs early passage cells). We hypothesized that the rapid aging cells were differentiating into myofibroblasts-like cells in later passages. It has been shown previously that fibroblasts (Desmouliere *et al.*, 1993; Vaughan *et al.*, 2000) or mesenchymal stem cells (Desai *et al.*, 2014) can differentiate into myofibroblast lineage when subjected to TGF- β pathway. We confirmed the upregulation of TGF- β pathway related proteins in rapid aging cells compared to slow aging cells at early passages and validated that activation of TGF- β pathway significantly increased actin stress fibers in DPSCs. TGF- β 1 induces mobilization and rapid polymerization of actin cytoskeleton and leads to the formation of stress fibers, a known morphological hallmark of cellular differentiation and aging (Cho et al., 2004; Edlund et al., 2002; Vallenius, 2013; Vardouli et al., 2008). More recently, treatment of DPSC with Notch ligand Jagged1 has shown to lead to reduced proliferation, upregulation of TGF- β and differentiation markers (Manokawinchoke et al., 2017), which could be correlated to our findings in rapid aging DPSCs. We now propose that upregulated TGF- β pathway genes may be considered as a hallmark of early onset of spontaneous differentiation in primary DPSCs in long-term cultures (Figure 1.21; Figure 1.22).

Cellular metabolism has been implicated in cell fate determination and stem cell activity in a variety of different contexts (Buck et al., 2016; Gascon et al., 2016; Zhang et al., 2016; Zheng et al., 2016). Highly proliferative stem cells have unique metabolic requirements (Vander Heiden et al., 2009), and they have the ability to switch between different metabolic pathways depending

on changes in substrate availability (Mathieu and Ruohola-Baker, 2017). Switching between different metabolic pathways can also regulate quiescent stem cell populations and the onset of differentiation (Beyaz et al., 2016; Cliff et al., 2017; Hamilton et al., 2015; Knobloch et al., 2013; Meng et al., 2018; Simsek et al., 2010). We now show that adult stem cells, DPSCs, are metabolically highly active cells that can utilize multiple fuel sources for ATP production. Mitochondrial theory of aging posits that mitochondrial aging is a fundamental cause of cellular aging (Barzilai et al., 2012). Accordingly, we find that the metabolic profile of DPSCs with early onset of cellular aging differ from the DPSCs with slow aging. In particular, DPSCs showing early onset of cellular aging exhibited lower glycolytic capacity and had highly reduced capacity to utilize lipids as an energy source. Importantly, these defects in preferred fuel usage were observed prior to the onset of other phenotypes, such as slow division rates. We therefore argue that metabolism serves as an early, predictive indicator of DPSCs tendency to lose stem cell self-renewal capacity (Figure 1.23). This raises the possibility that regulation of replicative senescence is controlled by similar switch in metabolism as seen previously with regulation of quiescence.

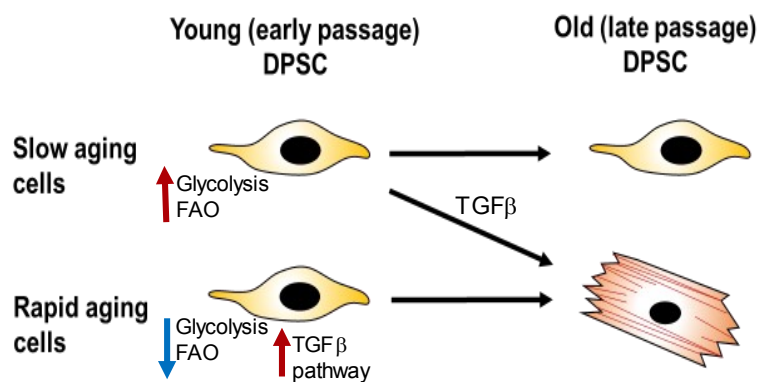


Figure 1.23. Conclusion model.

Hypothetical model: DPSCs transcriptome and metabolic analysis suggest that low glycolysis and fatty acid oxidation (FAO) and upregulation of TGFb activity at early passages are predictive for rapid aging phenotype in later passages.

Chapter 2. THE DEVELOPMENT OF INDUCED AMELOBLASTS

2.1 BACKGROUND

Tooth enamel is the hardest tissue in the human body. In addition to providing masticatory function, it protects the underlying dentin and dental pulp from mechanical, chemical, and microbiological damages that can lead to tooth loss. Unlike many other tissues, the adult human tooth does not regenerate enamel due to the absence of the enamel-secreting cell type, ameloblasts (Park et al., 2013), making enamel vulnerable to permanent damage or tooth loss. In addition to injury and damage, congenital genetic diseases such as Amelogenesis Imperfecta can also contribute to enamel loss. Ameloblasts are dental epithelial cells that secrete enamel protein matrix and deposit minerals to achieve hard and mature tooth enamel during human development (Jernvall and Thesleff, 2012). During tooth eruption in humans, ameloblasts undergo apoptosis (Park *et al.*, 2013; Yajima-Himuro et al., 2014). Though almost all humans acquire some damage to the protective enamel shield as adulthood progresses, we currently do not have a way to regenerate ameloblasts (Fugolin and Pfeifer, 2017).

Although tooth development has been studied over several years (Yu and Klein, 2020), most of these excellent developmental and molecular studies have been conducted using murine models (Balic and Thesleff, 2015; Chiba et al., 2020; Krivanek et al., 2020; Sharir et al., 2019; Thesleff, 2014) which presents several challenges when applied to human development (Balic, 2019; Fresia et al., 2021; Hovorakova et al., 2018). For example, mouse incisors undergo continuous regeneration due to a population of epithelial stem cells in the labial cervical loop that allows for continued enamel formation throughout life (Harada et al., 2002). Since this regenerative process does not occur in adult human teeth, it is critical to understand tooth

differentiation during early human developmental stages. In addition, the enamel organ, which ultimately gives rise to ameloblasts, is comprised of multiple populations of support cells, including the stellate reticulum and the inner and outer enamel epithelium (Nanci and TenCate, 2018). These support cells are thought to be essential for ameloblast function (Harada et al., 2006; Maas and Bei, 1997; Nakamura et al., 1991); however, it is not understood how they are mechanistically involved in ameloblast differentiation and functional maturation. Animal studies have suggested several pathways in driving and regulating this communication, such as the hedgehog (HH) (Koyama et al., 2001), NOTCH (Harada *et al.*, 2006), and FGF (Takamori et al., 2008) pathways. However, the temporal regulation and the extent to which these pathways originate from support cells are not clearly understood since these cells are poorly studied in humans. Dissecting human tooth development at the single-cell level can capture the patterns of gene expression that characterize small populations of support cells that are involved in the differentiation.

In order to understand human tooth development and to facilitate the regeneration of human tooth structures in the future, we have utilized single-cell combinatorial indexing RNA sequencing (sci-RNA-seq) (Cao et al., 2019) technology to study human fetal tooth development at 9-22 gestational weeks (gw). Through computational analysis of the sci-RNA-seq data, we established for the first time a spatiotemporal single-cell atlas for developing human teeth that includes both the epithelial and mesenchymal cell types. Our computational studies established human-specific transcriptional profiles for subtypes of the developing tooth and revealed novel branches in the developmental trajectories of both mesenchymal and epithelial-derived tissues, as well as previously undescribed populations of epithelial support tissues. Further, we defined and induced

the critical signaling pathways that drove changes in cell fate along the developmental trajectory of ameloblasts. This expedited the development of a 3D organoid that exhibits ameloblasts polarized towards odontoblast-like cells. This 3D organoid shows mineralization (calcium deposition) and expression of Ameloblastin, Amelogenin and Enamelin. Hence, we have coined the term Enamel Organoid to describe this new class of organoids.

These studies enhance our understanding of the regulatory mechanism controlling the differentiation process of dental tissues and lay the groundwork toward the development of disease models and regenerative approaches.

2.2 RESULTS AMELOBLAST PROJECT

2.2.1 *A single-cell atlas of the developing human fetal odontogenic tissues*

In humans, oral tissue development begins around 6gw and starts as a thickening in the oral epithelium (de Paula et al., 2017; Jussila and Thesleff, 2012; Nanci and TenCate, 2018), giving rise to all primary teeth and salivary gland tissue. Individual teeth develop independently as an extension of the main dental lamina and progress through a series of morphological stages (bud, cap, & bell) within bony crypts of the jaws (Radlanski et al., 2016). Additionally, each developing tooth is surrounded by thick fibrous tissue called the dental follicle (Wise et al., 1998). The dental follicle and the tissue it contain comprise the toothgerm (Kardos and Hubbard, 1981) (Figure 2.1.A). The oral epithelium will also give rise to the salivary glands (Figure 2.1.A). Like teeth, salivary glands derive from the invagination of a thickened sheet of oral epithelium into the underlying mesenchyme, known as the initial bud stage (Cha, 2017) (Figure 2.1.A).

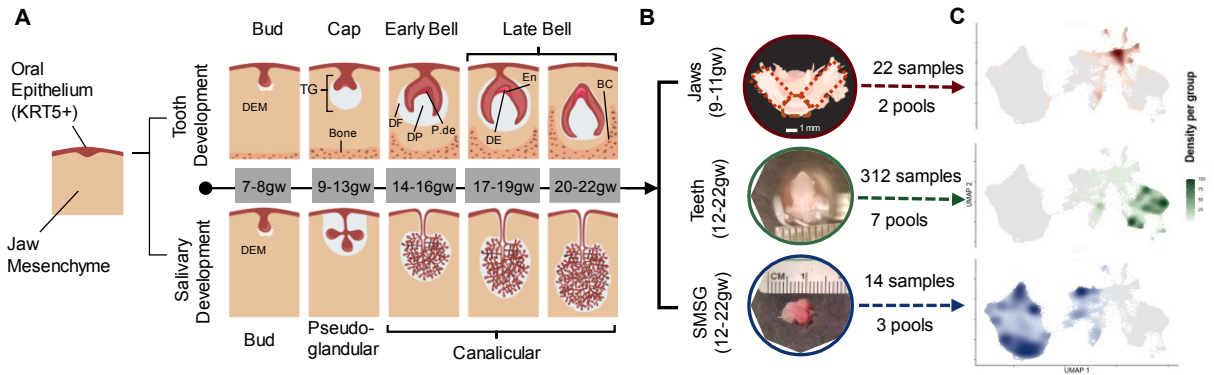


Figure 2.1. Tooth development and the design of sci-RNA-seq.

Human tooth and salivary gland exhibit stepwise developmental processes (A) The oral epithelium (colored in red) will give rise to the epithelial components of teeth and salivary glands, while the condensed dental ectomesenchyme (DEM, colored in grey) will give rise to the mesenchymal component of these tissues. TG: toothgerm, DF: dental follicle, DP: dental papilla, P-de: pre-dentin, De: dentin, En: enamel matrix. (B) Human fetal tooth germs and salivary glands were dissected in a stage-specific manner from human fetal jaw tissue. The young fetal jaws, 9-11 gestational weeks, were segmented into anterior segments (dotted box, which span from the canine-to-canine region) and posterior jaw segment pairs (dotted box) and sequenced independently. For older fetal jaws, 12-22 gestational weeks, individual toothgerms and submandibular salivary glands were dissected. A more detailed look at the dissection process can be found in Figure 2.2. (C) Density plots of the clustered sci-RNA-seq data highlight the location of each tissue type in the same UMAP coordinate in Figure 2.3

To better understand early oral differentiation and to dissect how the epithelial and mesenchymal cell lineages acquire the odontogenic competence, we analyzed the developmental gene expression profiles of human fetal stages by single-cell sequencing. Toothgerm and salivary gland samples were collected from five fetal age groups (Figure 2.1.A-B and Figure 2.2.A-C).

These age groups represented the following developmental stages for tooth differentiation: the cap stage (9-13gw), the early bell stage (14-16gw), and the late bell stage (17-22gw) (Figure 2.1.A) (Nanci and TenCate, 2018; Nelson, 2020). We also collected submandibular salivary glands (SMSG) from three matched timepoints (12-13gw, 14-16gw, 17-19gw) that cover the pseudo-glandular and canalicular stages for salivary gland development (Quirós-Terrón et al., 2019) (Figure 2.1.A).

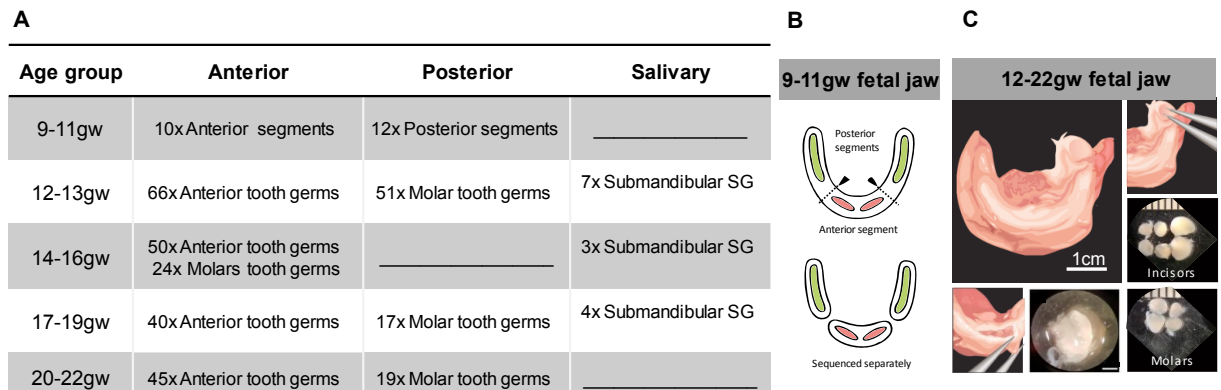


Figure 2.2. The dissected samples.

(A) Depending on the tissue size at a given age, between 3 and 50 of each tissue sample were collected, pooled into 12 samples, and sent for sci-RNA-seq. (B) At 9-11w, dissecting individual toothgerms or salivary glands in the bud stage was not feasible due to the large number of cells required to perform sci-RNA-seq protocol. Instead, jaws were separated into two segments of posterior jaw, containing jaw tissue distal of the canines (B, red boxes), and one segment of anterior jaw spanning from canine tooth to canine tooth region (B, blue box). At 12 weeks gestation and beyond, individual toothgerms and submandibular salivary glands could be identified and isolated to be sequenced separately (C).

Single-cell sequencing data of the tissue samples were analyzed using Monocle3 (Cao *et al.*, 2019; Trapnell et al., 2014) and visualized in uniform manifold approximation and projection (UMAP) space (Figure 2.3). The distribution of the cells from each tissue origin was identified by using density plots based on tissue type (Figure 2.1.C) or by individual samples (Figure 2.4).

Utilizing a graph-based clustering algorithm, we annotated 20 major clusters based on key marker genes (Figure 2.4; Figure 2.5; Table 2.1) from PanglaoDB (Franzén et al., 2019). The major cell types in salivary gland samples include salivary mesenchyme, salivary epithelium, cycling salivary epithelium, myoepithelium, and ductal cells (Figures 2.1.C; Figure 2.4; Figure 2.5). In the jaw samples (9-11gw) (Figures 2.1.C; Figure 2.4; Figure 2.5), we identified mesenchymal progenitors, osteoblasts, neuronal, Schwann cells, muscle, respiratory epithelium, otic epithelium, and oral epithelium (Figures 2.1.C; Figure 2.4; Figure 2.5). The major cell types in tooth samples include dental mesenchyme, epithelium, odontoblasts, and ameloblasts. The cell types observed in all samples include endothelial (Albelda et al., 1991; Jiang et al., 2016; Lampugnani et al., 1992) and immune (Böheim et al., 1987; Filion et al., 1990) cells.

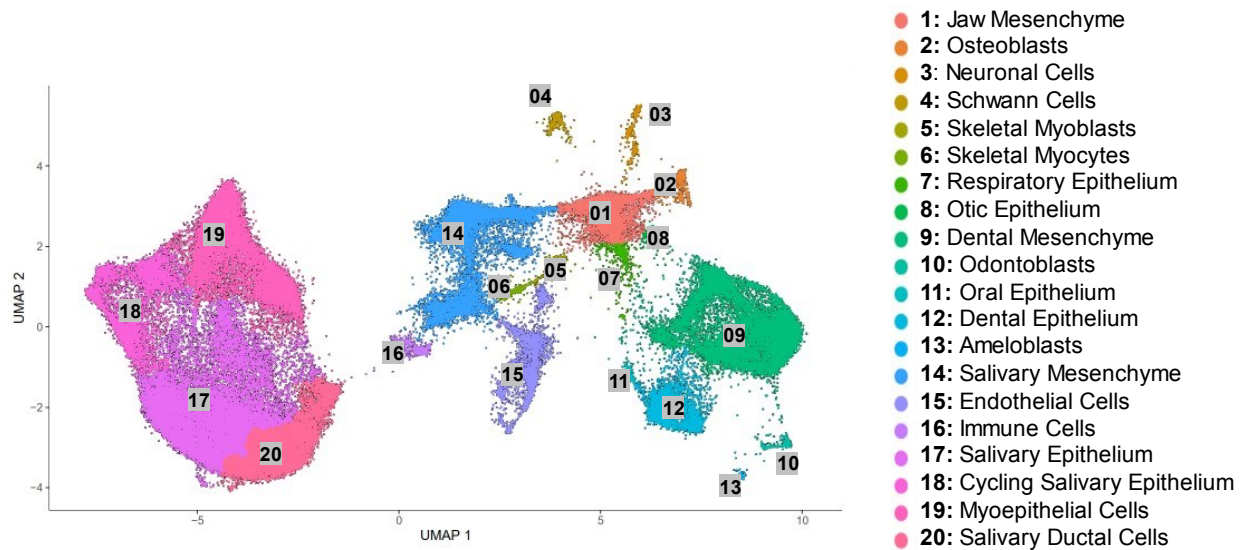


Figure 2.3. Visualization of all sequenced data

sci-RNA-seq data visualized in the UMAP coordinate showing the 20 annotated clusters from all sequenced data.

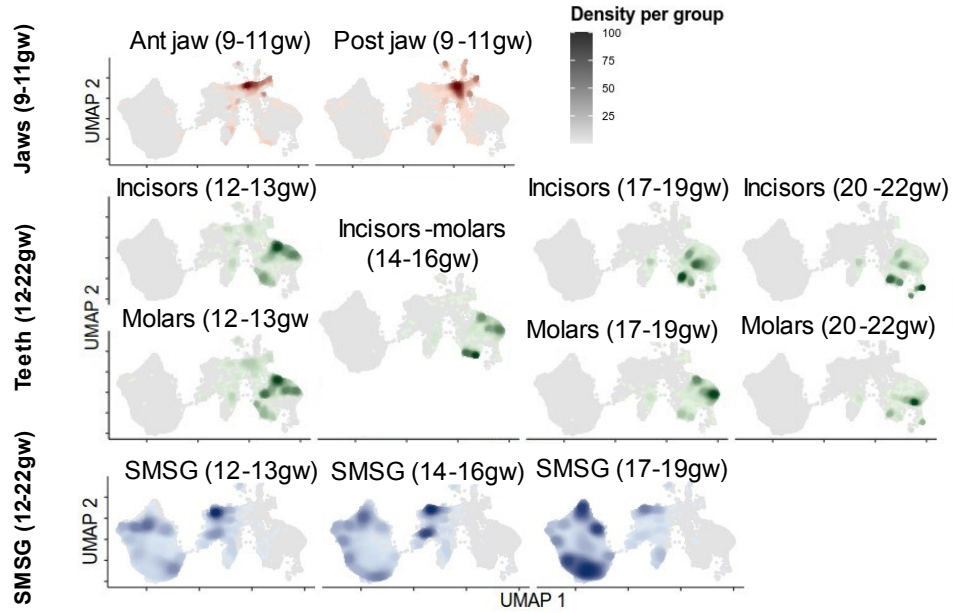


Figure 2.4. Distribution by sample

Sequenced data was clustered, and the resulting plot revealed that each major tissue type occupied a specific region of the plot, with some shared support tissues localized in the center.

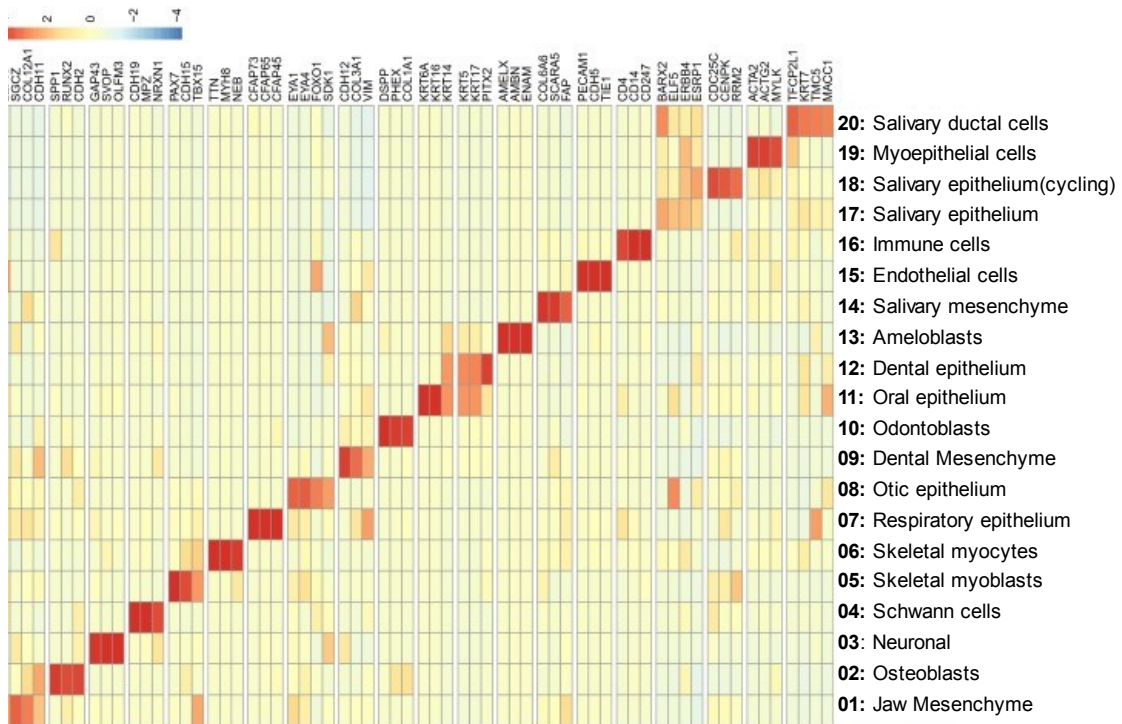


Figure 2.5. Heatmap for top markers of each cluster

Clusters were identifiable by expression of known markers for each tissue type in heatmap.

Table 2.1. Marker genes used to identify cell types in Figure 2.3

Cluster	Cell Type	Marker Gene	Gene Name
1	Jaw Mesenchyme	LEPR1	Leptin-receptor
2	Osteoblasts	SPP1	Secreted Phosphoprotein 1 or Osteopontin
		RUNX2	RUNX Family Transcription Factor 2
3	Neuronal Cells	GAP43	Growth Associated Protein 43 or Neuromodulin
4	Schwann Cells	MPZ	Myelin Protein Zero
		CDH19	Cadherin 19
5	Skeletal Myoblasts	PAX7	Paired Box 7
		CDH15	Cadherin 15 or Muscle Cadherin
6	Skeletal Myocytes	TTN	Titin
		MYH8	Myosin Heavy Chain 8
		NEB	Nebulin
7	Respiratory Epithelium	CFAP73	Cilia And Flagella Associated Protein 73
		CFAP65	Cilia And Flagella Associated Protein 65
		CFAP45	Cilia And Flagella Associated Protein 45
8	Otic Epithelium	EYA1	EYA Transcriptional Coactivator And Phosphatase 1
		EYA4	EYA Transcriptional Coactivator And Phosphatase 4
		FOXO1	Forkhead Box O1
9	Dental Mesenchyme	COL3A1	Collagen Type III Alpha 1 Chain
		VIM	Vimentin
		CDH12	Cadherin 12 or Neuronal Cadherin 2
10	Odontoblasts	DSPP	Dentin Sialophosphoprotein
11	Oral Epithelium	KRT14	Keratin 14
		KRT5	Keratin 5
		KRT6A	Keratin 6A
		KRT16	Keratin 16
		KRT17	Keratin 17
12	Dental Epithelium	PITX2	Paired Like Homeodomain 2
13	Ameloblast	AMELX	Amelogenin X-Linked
		AMBN	Ameloblastin
		ENAM	Enamelin
14	Salivary Mesenchyme	FAP	Fibroblast Activation Protein Alpha
15	Endothelial Cells	PECAM	Platelet And Endothelial Cell Adhesion Molecule 1 or CD31
		CDH534	Cadherin 5 or CD144
16	Immune Cells	CD4	CD4 Molecule
		CD14	CD14 Molecule

Cluster	Cell Type	Marker Gene	Gene Name
17	Salivary Epithelium	ELF4	E74 Like ETS Transcription Factor 4
		ERBB4	Erb-B2 Receptor Tyrosine Kinase 4
		BARX2	BARX Homeobox 2
18	Cycling Salivary Epithelium	CDC25C	Cell Division Cycle 25C
		CENPK	Centromere Protein K
		RRM2	Ribonucleotide Reductase Regulatory Subunit M2
19	Myoepithelial Cell	ACTA2	Actin Alpha 2, Smooth Muscle
20	Salivary Ductal Cells	TFCP2L1	Transcription Factor CP2 Like 1 or LBP9
		KRT7	Keratin 7

To confirm the timing of the tooth morphological stages, we performed immunohistochemistry on tissue sections. As expected, all the enamel organ derived tissues were visualized by KRT5 (green) (Figure 2.6). There are two critical lineages in tooth development: odontoblasts and ameloblasts. These two cell types secrete the mineralized protective layers that cover the soft dental pulp, which contains the nerves and the nutrient-transporting blood vessels. Odontoblasts are ectomesenchyme-derived cells secreting the inner coverage for the pulp, called dentin, while ameloblasts are ectoderm-derived and secrete the outermost layer, enamel. In order to establish the expression of known odontoblast and ameloblast markers in our tissue, immunohistochemistry was performed on human fetal toothgerm at 20gw using dentin sialophosphoprotein (DSPP) and ameloblastin (AMBN), respectively (Figure 2.7.A-F). As expected, ameloblasts express AMBN in secretory vesicles (Figure 2.7.D and E); likewise, odontoblasts secrete DSPP (Figure 2.7.D and F).

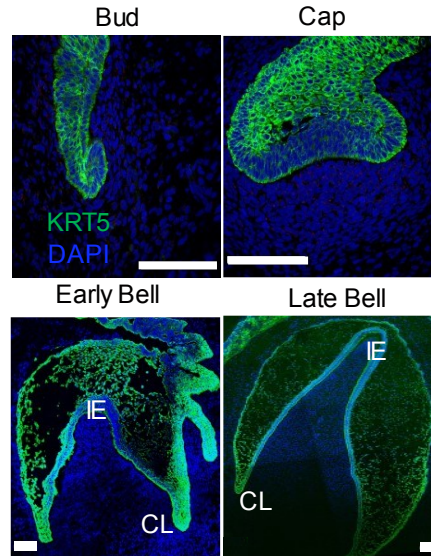


Figure 2.6. Stages of tooth development

Immunofluorescence staining of developing toothgerms tissue sections with anti-Krt5 (green) that specifically marks the dental epithelial morphology throughout the developmental stages. Counterstained with the nuclear staining DAPI (blue). Abbreviations: incisal edge (IE), cervical loop (CL). Scale bars: 50 μ m.

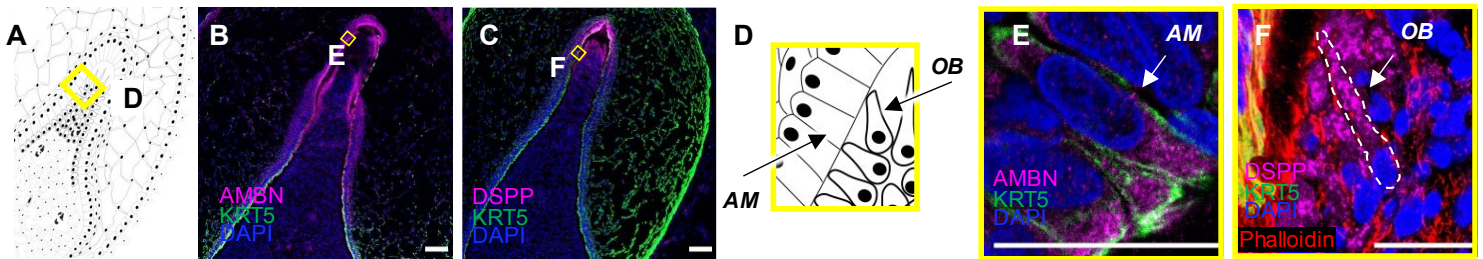


Figure 2.7. Ameloblasts and odontoblasts markers

To establish expression of known odontoblast and ameloblast markers in our tissue, immunofluorescence was performed on human fetal toothgerm at 20gw using dentin sialophosphoprotein (DSPP) and ameloblastin (AMBN), respectively (B,C) higher magnification in (E,F). Simplified illustration in (A, D). As expected, ameloblasts marked by AMBN (B, E) (pink), and odontoblasts by DSPP (C, F) (pink). Scale bars: 50 μ m.

2.2.2 *sci-RNA-seq and spatial localization reveal stage-specific support cell types and cervical loop stem cells for ameloblast differentiation*

To further analyze the subtypes of the dental epithelium, we subset oral epithelium, dental epithelium, and ameloblast clusters (Figure 2.8). The subset yielded 13 unique clusters that we identified by collating highly expressed cluster-specific genes (Figure 2.9 and Figure 2.10; Table 2.2). We were able to identify oral epithelium (OE), dental epithelium (DE), enamel knot (EK), enamel epithelium (outer enamel epithelium/inner enamel epithelium, OEE/IEE), cervical loop (CL), inner and outer stratum intermedium (SII, SIO), inner and outer stellate reticulum (SRI and SRO), pre-ameloblasts (PA) and two AMBN expressing ameloblast clusters (early ‘eAM’ and secretory ‘sAM’; Figure 2.8; Figure 2.9; Figure 2.10; Table 2.2). The identity of these clusters aligned with their likely real-time appearance as represented by a real-time distribution of cells (Figure 2.11). Moreover, GO analysis (Figure 2.9) indicated cell type-specific roles in tooth development in agreement with our annotations. For example, the OE cluster revealed proper stratified epithelium, including keratinization, keratinocyte differentiation, and cornification (Adams, 1976), while the DE shows epithelial organization and differentiation, indicative of its function in reorganizing to form the tooth bud (Ahtiainen et al., 2016).

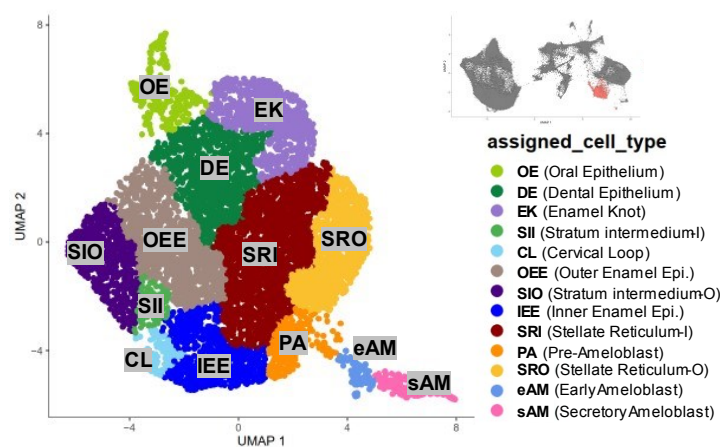


Figure 2.8. Oral and dental epithelial lineages

(A) UMAP graph of subclustered molar and incisor toothgerm type dental epithelium derived cells from the total dataset identified 13 transcriptionally unique clusters including the oral epithelium (OE), dental epithelium progenitors (DE), enamel knot (EK), outer enamel epithelium (OEE), inner enamel epithelium (IEE), cervical loop (CL), inner stratum intermedium (SII), outer stratum intermedium (SIO), inner stellate reticulum (SR), inner stellate reticulum (SRI), pre-ameloblasts (PA), early ameloblasts (eAM) and ameloblasts (sAM). (B) A custom heatmap was generated to identify the marker genes specific to each cluster, the top associated GO-terms to characterize cluster function, and calculated Age Score per cluster.

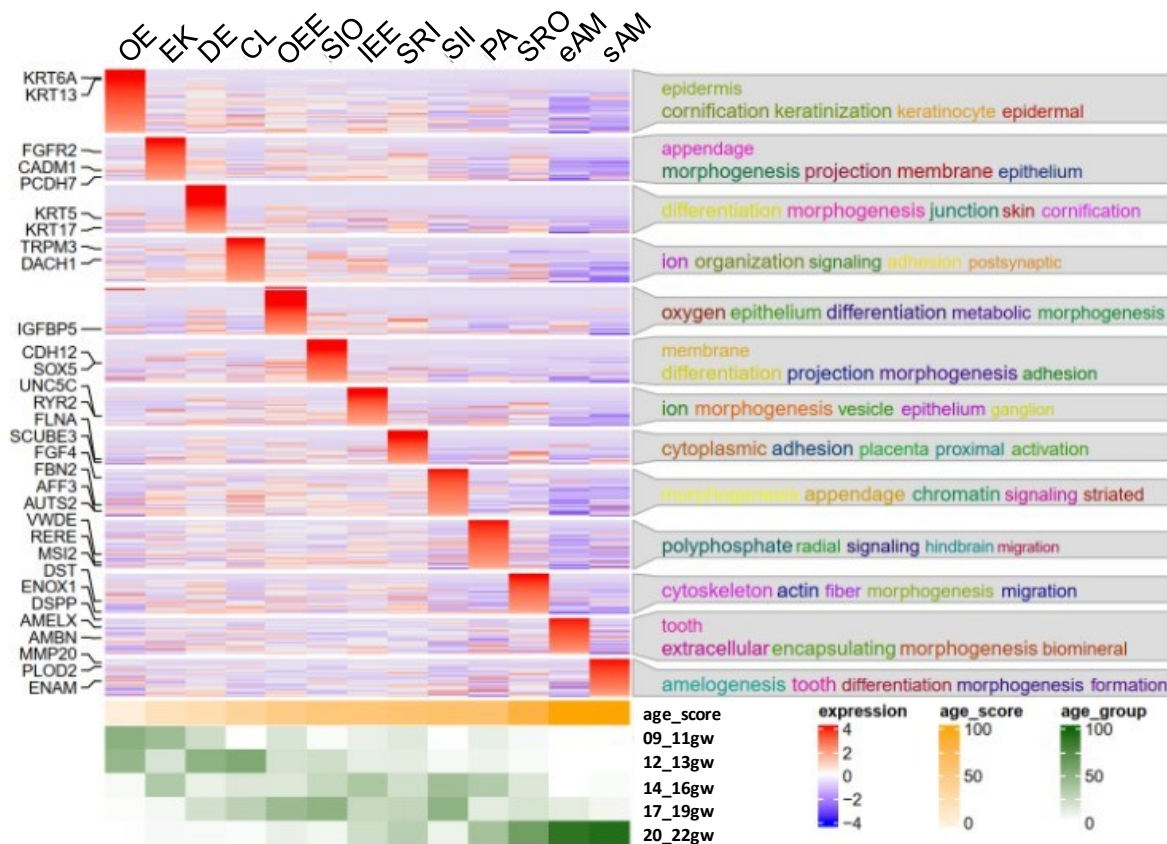


Figure 2.9. Heatmap for top marker genes of dental epithelial lineages

A custom heatmap was generated to identify the marker genes specific to each cluster, the top associated GO-terms to characterize cluster function, and calculated Age Score per cluster.

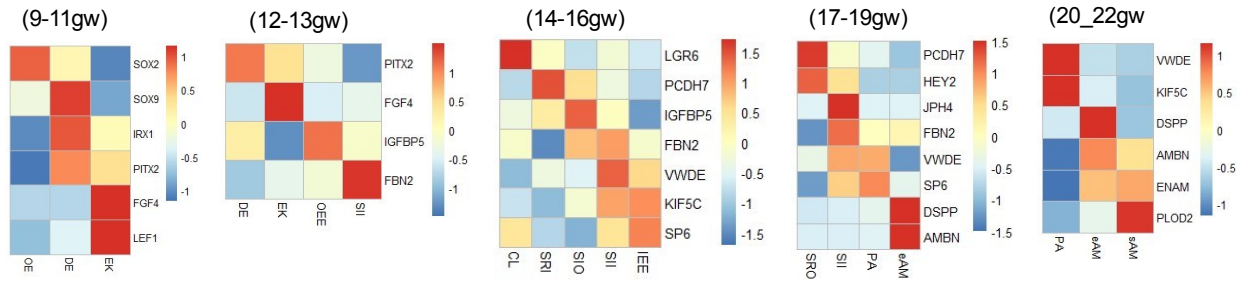


Figure 2.10. Heatmap for top marker broken by timepoints

Expression of known markers at stages of dental epithelial lineage align with previously identified markers in each tissue and appear at expected developmental timepoints.

Table 2.2. Marker genes used to identify cell types of the dental epithelium

Cell Type	Marker Gene	Gene Name
Oral Epithelium (OE)	KRT6A	Keratin 6A
	KRT13	Keratin 13
Enamel Knot (EK)	SHH	Sonic Hedgehog Signaling Molecule
	LEF1	Lymphoid Enhancer Binding Factor 1
	FGF4	Fibroblast Growth Factor 4
	FGFR2*	Fibroblast Growth Factor Receptor 2
	CADM1*	Cell Adhesion Molecule 1
	PCDH7*	Protocadherin 7
Dental Epithelium (DE)	PITX2	Paired Like Homeodomain 2
	KRT5*	Keratin 5
	KRT17*	Keratin 17
Cervical Loop (CL)	LGR6	Leucine Rich Repeat Containing G Protein-Coupled Receptor 6
	TRPM3*	Transient Receptor Potential Cation Channel Subfamily M Member 3
	DACH1*	Dachshund Family Transcription Factor 1
Outer Enamel Epithelium (OEE)	IGFBP5**	Insulin Like Growth Factor Binding Protein 5
Stratum Intermedium Outer (SIO)	CDH12*	Cadherin 12
	SOX5*	SRY-Box Transcription Factor 5

Cell Type	Marker Gene	Gene Name
Inner Enamel Epithelium (IEE)	UNC5C*	Unc-5 Netrin Receptor C
	RYR2*	Ryanodine Receptor 2
Stratum Reticulum Inner (SRI)	PCDH7**	Protocadherin 7
	FLNA*	Filamin A
	SCUBE3*	Signal Peptide, CUB Domain And EGF Like Domain Containing 3
Stratum Intermedium Inner (SII)	FBN2**	Fibrillin 2
	AFF3*	AF4/FMR2 Family Member 3
	AUTS2*	Activator Of Transcription And Developmental Regulator AUTS2
Preameloblast (PA)	VWDE	Von Willebrand Factor D And EGF Domains
	SHH	Sonic Hedgehog Signaling Molecule
	CYP2S1	Cytochrome P450 Family 2 Subfamily S Member 1
	KIF5C	Kinesin Family Member 5C
	RERE*	Arginine-Glutamic Acid Dipeptide Repeats
	MSI2*	Musashi RNA Binding Protein 2
Stratum Reticulum Outer (SRO)	DST*	Dystonin
	ENOX1*	Ecto-NOX Disulfide-Thiol Exchanger 1
Early Ameloblast (eAM)	DSPP	Dentin Sialophosphoprotein
	AMELX18	Amelogenin X-Linked
	AMBN19	Ameloblastin
Secretory Ameloblast (sAM)	MMP20	Matrix Metalloproteinase 20
	PLOD2	Procollagen-Lysine,2-Oxoglutarate 5-Dioxygenase 2
	ENAM	Enamelin
		<i>*Predicted **Novel</i>

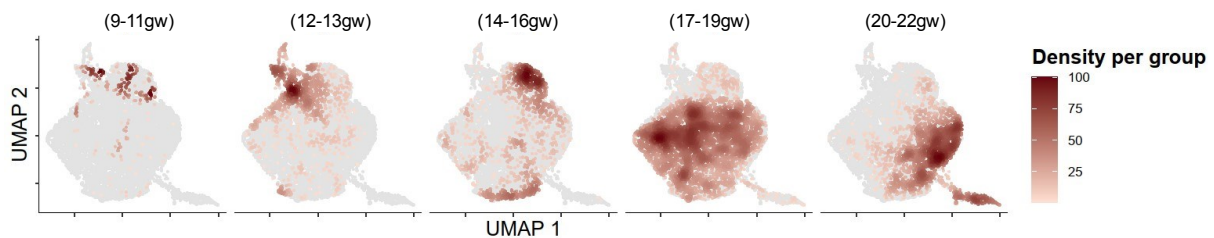


Figure 2.11. Realtime density plots

Density of cells plotted by age demonstrates that clusters enriched with more cells at a given timepoint.

To identify the developmental trajectory of the dental epithelial lineages, we performed pseudotime analysis (Figure 2.12.A) summarized by the simplified tree graphs (Figure 2.12.B, ameloblast trajectory with red arrows). The trajectory analysis suggests that the OE directly gives rise to DE. The DE then gives rise to the EK and SR lineages and the OEE lineage, which gives rise to SI, IEE/PA, and eAM/sAM. In order to validate our bioinformatic findings, we performed RNAScope in situ hybridization at multiple timepoints. We used combinations of cluster-specific markers identified by transcriptional analysis (Figure 2.13; Table 2.3) to map cells from each cluster in the fetal tissues (Figure 2.14.A, 2.15.A-B;). Computational pseudo-spatial mapping of these cells revealed the following insights on EK, support cells, and CL function (Figure 2.14.B and Figure 2.16).

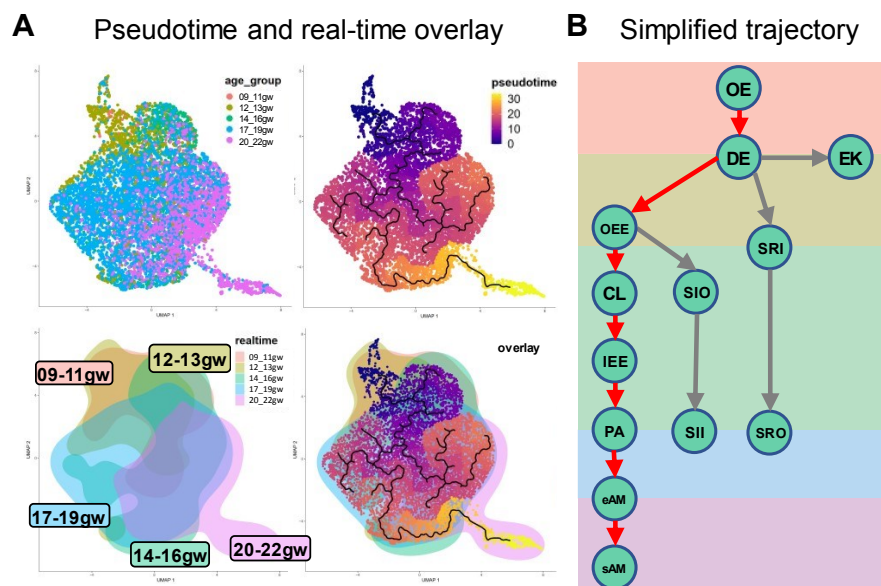


Figure 2.12. Pseudotime and realtime overlay

(A) Pseudotime trajectory analysis and realtime overlay for dental epithelium derived cells suggests that the DE directly gives rise to three branch lineages including the OEE, SR and EK. (B) Simplified differentiation trajectory tree illustrating the separate lineages originating from the DE, including the main AM lineage (red), of OEE, which gives rise to CL, IEE and PA, which then gives rise to eAM and sAM; and support cell trajectories (grey).

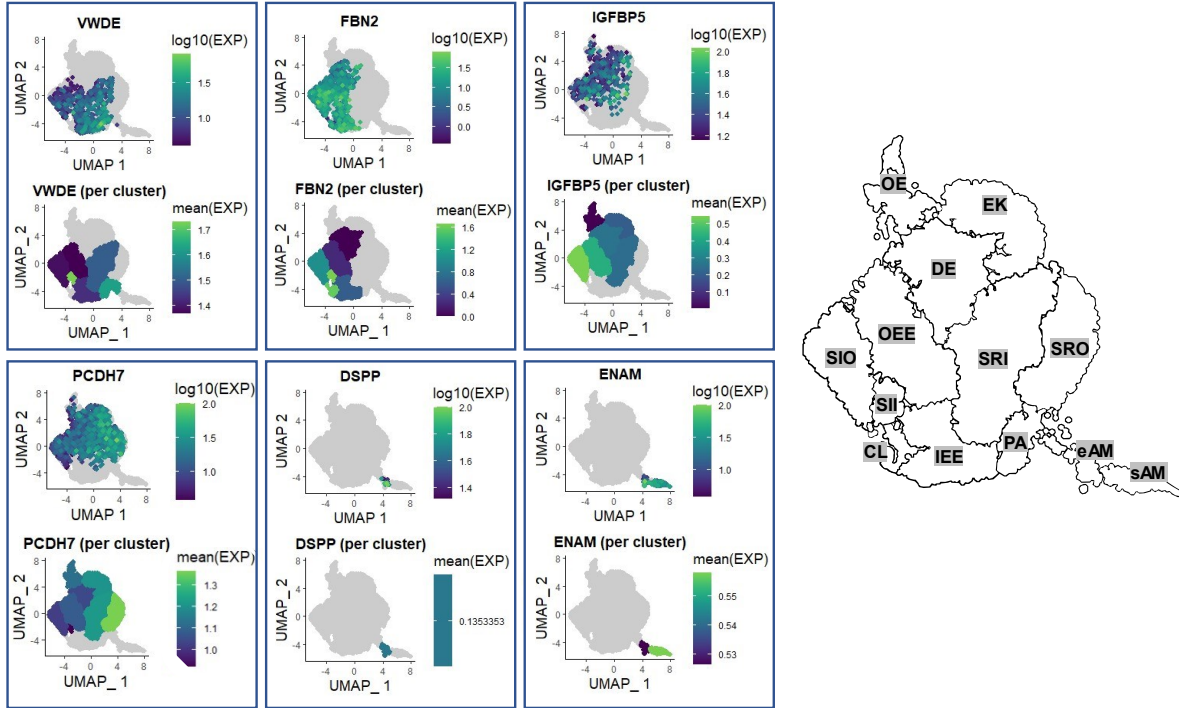


Figure 2.13. Gene expression plots for top marker genes.

Gene plots and mean expression per cluster summary plots in UMAP space generated for the markers used to infer the logic table 2.3 which is used in the RNAScope mapping. The threshold expression per cluster was set to 25% of maximum expression per gene. Light green clusters considered as high expressing, dark blue as low expressing, and gray as low or no expression.

Table 2.3. Logic table used to map clusters

		Probe						
		PCDH7	FBN2	KRT5	VWDE	IGFBP5	DSPP	ENAM
Cluster	PA	0, Low	0, Low	Low	High	0, Low	NA	NA
	IEE	0, Low	Low, High	Low	Low	0	NA	NA
	SII	0, Low	High	High	High	0, Low	NA	NA
	SIO	0, Low	Low, High	High	0, Low	Low, High	NA	NA
	OEE	0, Low, High	0, Low	Low, High	0, Low	High	NA	NA
	CL	0, Low	0, Low, High	High	0	0	0	0
	SRI	0, Low, High	0	Low, High	Low	0, Low	NA	NA
	SRO	0, Low, High	0	Low	0	0, Low	NA	NA
	sAM	NA	NA	Low, High	NA	NA	High	0, Low
	eAM	NA	NA	Low, High	NA	NA	0, Low	High

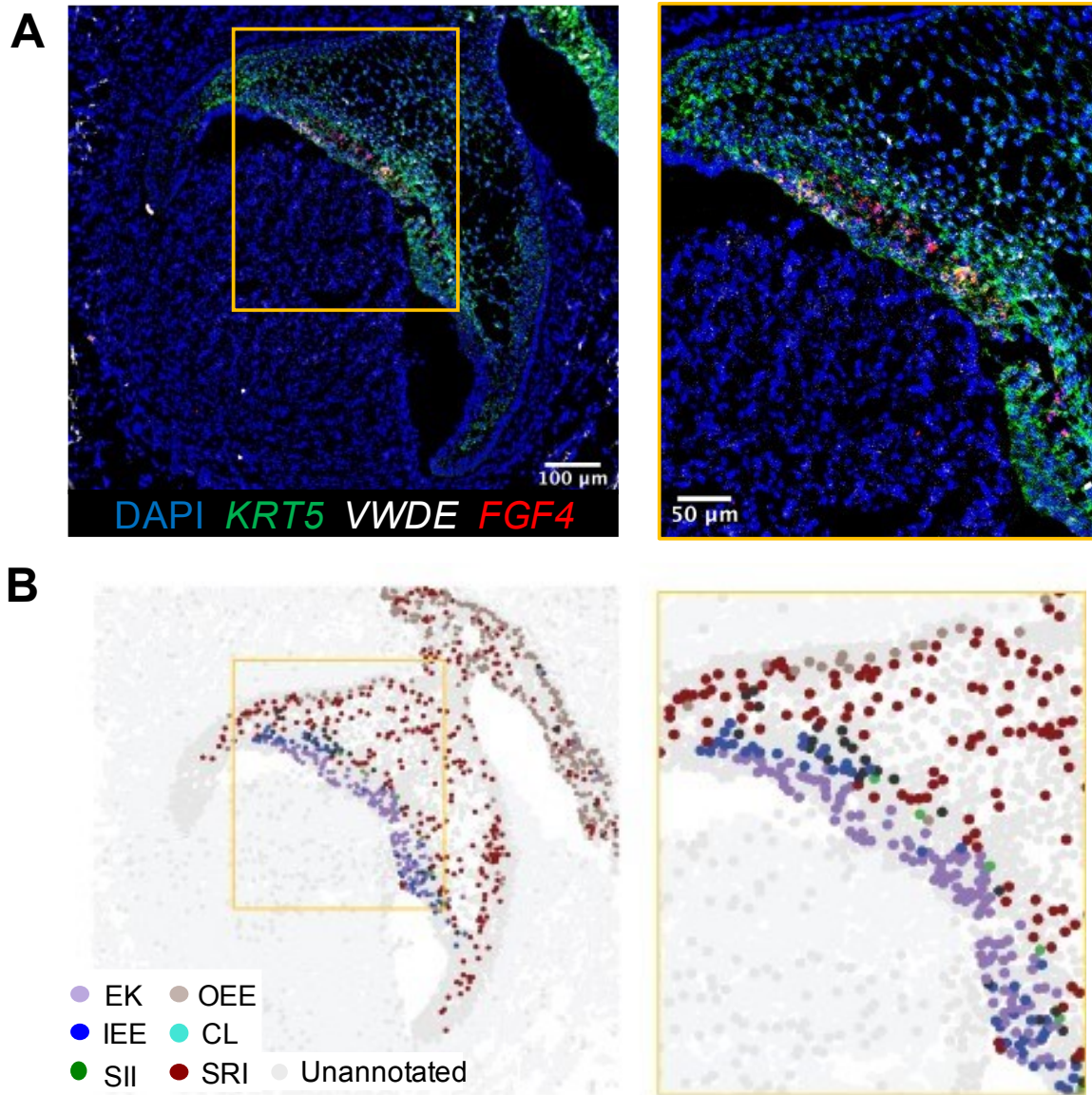


Figure 2.14. RNAScope for 13gw toothgerm

(A) RNAScope HiPlex *in situ* hybridization image and inset for VWDE (high in IEE, SII, SRI), and FGF4 (high in EK) probes with DAPI nuclear stain at 13gw. (B) RNAScope map of individual dental epithelium-derived clusters - EK, OEE, IEE, CL, SII, and SRI – present at 80d shown as determined by relative expression of markers as specified in table 2.3

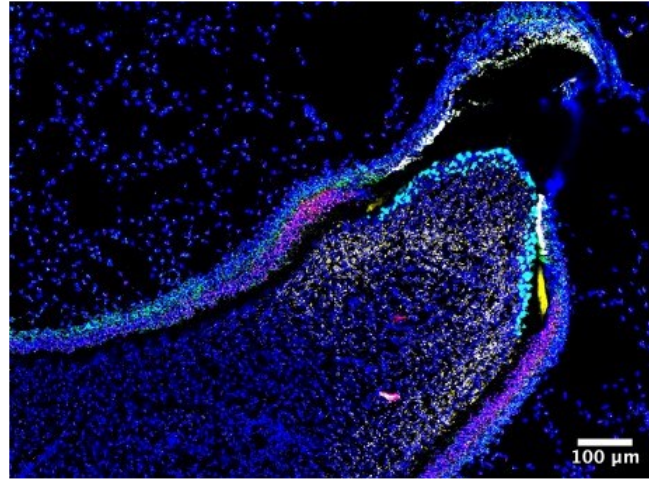
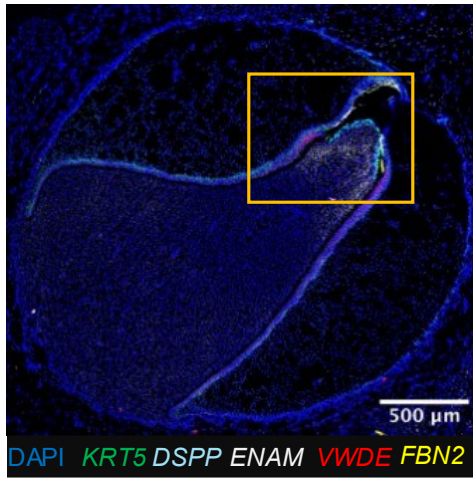
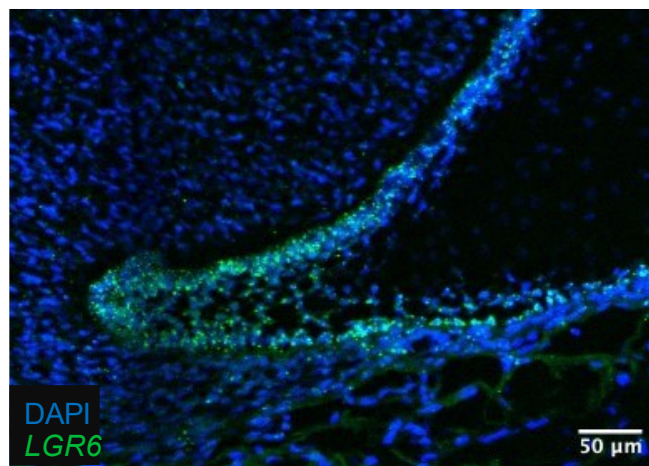
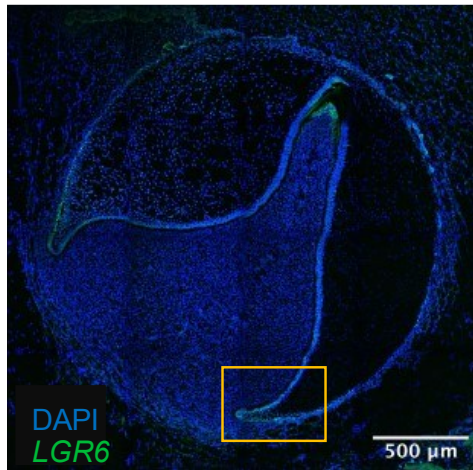
A**B**

Figure 2.15. RNAScope for 19gw toothgerm

(A) RNAScope HiPlex *in situ* hybridization image and inset for *DSPP* (high in eAM), *ENAM* (high in sAM), *VWDE* (high in SII, CL, PA), *FBN2* (high in IEE, SII, CL) probes with DAPI nuclear stain at 19gw. (B) RNAScope staining for *LGR6* probe marking the cervical loops.

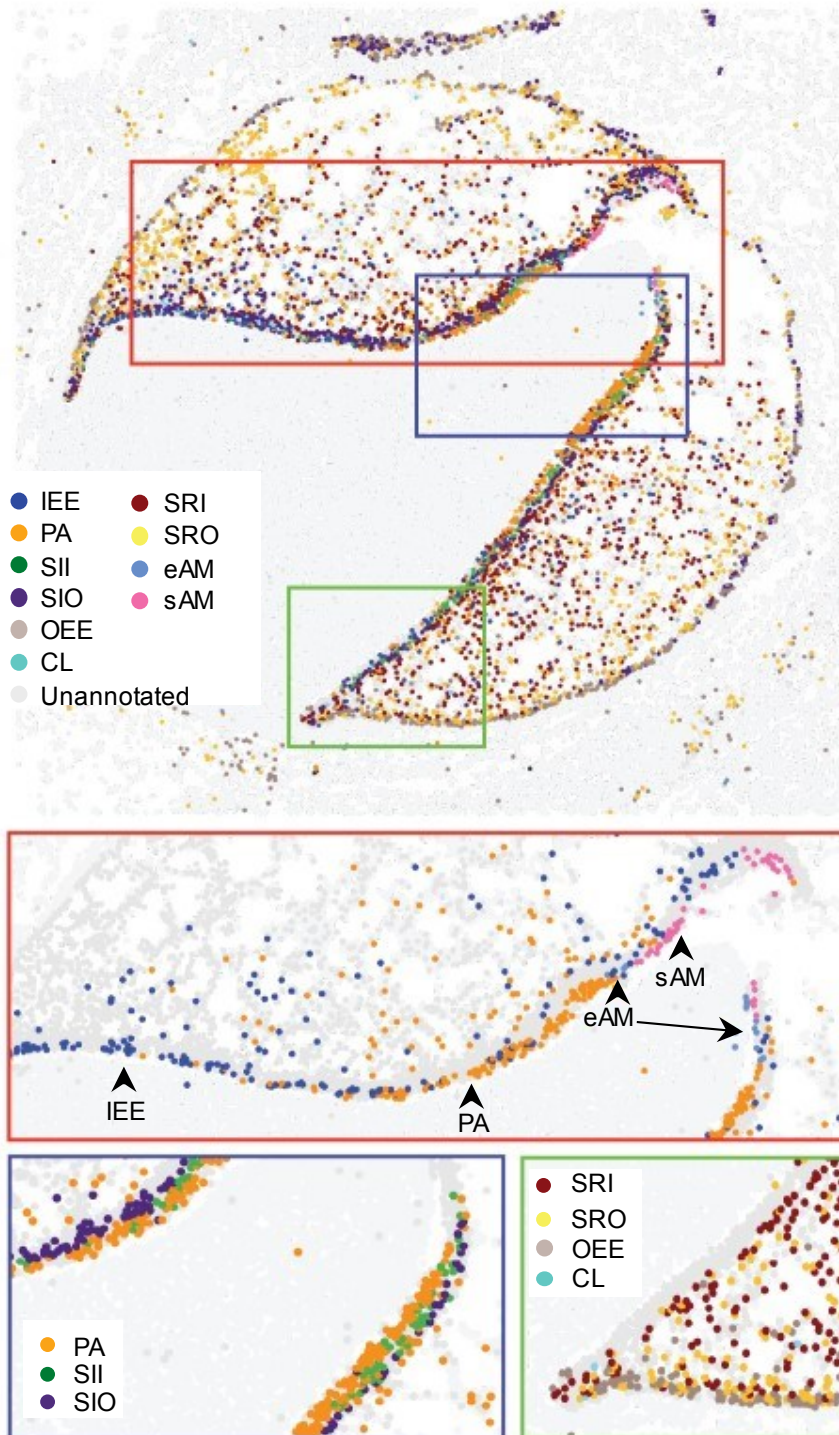


Figure 2.16. Cluster mapping for 19gw toothgerm

RNAScope map of individual dental epithelium derived clusters – IEE, PA, SII, SIO, OEE, CL, SRI, SRO, eAM, and sAM – present at 19gw shown as determined by relative expression of markers as specified in (Table 2.3)

The EK is a structure that has previously been identified at various times in mouse tooth development and is thought to organize local cell proliferation for epithelial budding or folding during cap and bell stage transitions (Thesleff et al., 2001; Vaahtokari et al., 1996; Yu et al., 2020). Primary EK has been shown to appear at the time of the first folding of the toothgerm to form the cusp, followed by secondary EK formation for subsequent cusp development. We identified a cluster of cells consistent with EK in human fetal development. Real-time distribution showed that cells occupying this cluster appeared at 9-11gw (early cap stage) and again at 14-16gw (early bell stage) (Figure 2.9; Figure 2.10; Figure 2.14), in line with the expected appearance of primary and secondary EK, respectively. EK are essential signaling centers in these early stages of tooth morphogenesis, playing a role in determining crown shape. Accordingly, GO terms identified in response to top gene expression associated with these clusters included morphogenesis and appendage development. These findings represent the first time this population has been identified at the transcriptional level and can lead to further understanding of the initiation of tooth morphogenesis and toothgerm type determination.

Multiple types of support tissues exist in the developing enamel organ. The SR are support cells with a star-shaped appearance in histological sections (Liu et al., 2016), which are thought to provide nutrients to and cushion the developing ameloblasts (Nanci and TenCate, 2018). Another support cell type, SI, is thought to support ameloblast differentiation (Liu *et al.*, 2016) (Figure 2.8 and Figure 2.9). We identified both types of support tissue in human fetal tissues. Furthermore, our single-cell analysis expanded upon what we understand about these populations. Transcriptomic analysis revealed two subgroups of SR, inner SR (SRI) closer to the inner surface of the toothgerm and outer SR (SRO) (Figure 2.9; Figure 2.10; Figure 2.16). Our analyses also

identified, for the first time, two human SI sub-clusters that appear at 12gw and persist to later development (Figure 2.8; Figure 2.9; Figure 2.10; Figure 2.16). Inner SI (SII) represents the cell layer closer to ameloblasts lineage, and outer SI (SIO) represents the parallel support cell types adjacent to SII. The SI lineage at the early bell stage consists of two layers of cells, SII and SIO, that lie near ameloblast lineage (IEE, PA, and AM) (17-19gw) (Figures 2.15; Figure 2.16; Figure 2.17), creating a 3rd previously unidentified stage-specific layer of cells (Figure 2.16 bottom left enlarged box). Furthermore, at the late bell stage, PA differentiates into eAM and matures to sAM (17-19gw) (Figure 2.16 top enlarged box; Figure 2.17). We propose these novel subgroups of support cells have precise signaling capacity to the specific, nearby epithelial cells in ameloblast lineage.

The enamel epithelium is the basal cell layer on the periphery of the tooth consisting of OEE, lining the outer side of the tooth, and IEE (Krivanek *et al.*, 2020), lining the concave side of the folded tooth (Liu *et al.*, 2016). As predicted, the transcriptional analysis revealed the presence of both of these populations, which was confirmed with RNAScope in situ hybridization (Figure 2.8; Figure 2.9; Figure 2.16 bottom right enlarged box). sci-RNA-Seq and RNAScope analysis revealed that in the cap stage, the core cells of the enamel organ are the DE that will give rise to the signaling center EK and the OEE (12-13gw) (Figures 2.14 and Figure 2.17). sci-RNA-Seq also revealed a small population of LGR6⁺ CL cells expressing markers previously reported in epithelial stem cells of the regenerating adult mouse incisor (Chang *et al.*, 2013). We could localize these cells in human fetal tissue to the expected location of the CL, where the OEE and IEE meet (Figures 2.15.B and Figure 2.17). During the early bell stage, OEE are the basal cells on the periphery of the tooth organ that gives rise to SI, CL, & PA lineages (17-19gw) (Figure 2.15.A;

Figure 2.16 and Figure 2.17). Importantly, the trajectory analysis predicts that the stem cells in CL can give rise to the ameloblast lineage. These data suggest that CL has a stage-specific role; while CL in humans is traditionally thought to be involved in later root development, our data suggest that during the early stage of fetal development, CL has a vital function in generating ameloblast lineage as the tooth crown expands. Further study is needed to determine these CL cells' role in toothgerm type determination, including root number and morphology.

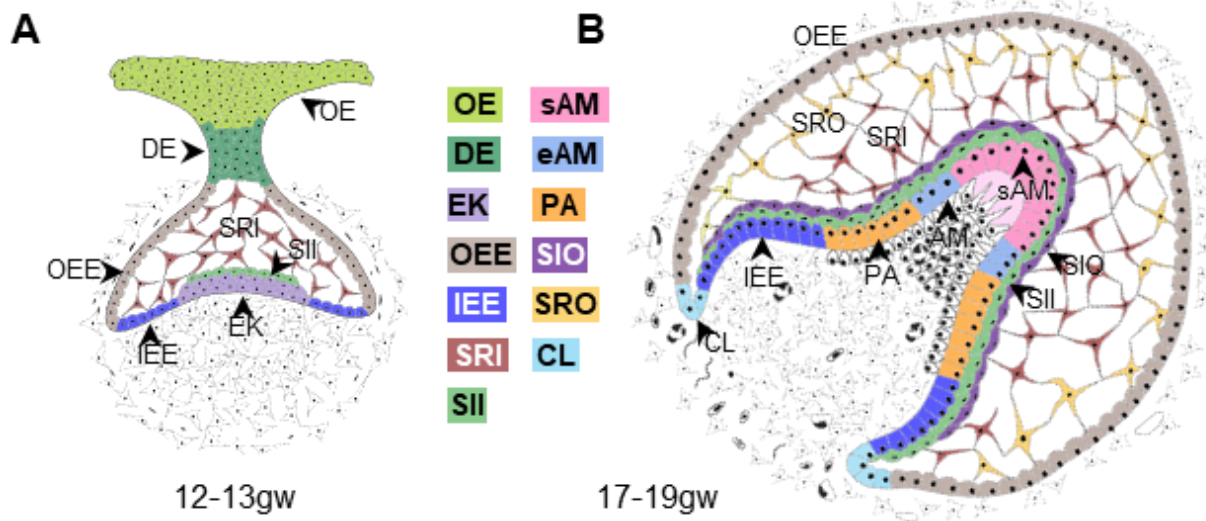


Figure 2.17. Simplified diagram of the cluster locations

A diagram of the developing dental epithelium derived cell types of a toothgerm at 12-13 gestational weeks. The OE is lining the oral cavity while DE is the stalk connecting OE to the enamel organ. DE has given rise to the signaling center EK and SRI. OEE present at the periphery of the enamel organ have given rise to CL, SII and IEE. (K) A diagram of the developing dental epithelium derived cell types of a toothgerm at 17-19 gestational weeks. SII give rise to SIO layer, and together represent the superficial layer above IEE, PA, eAM and sAM, while SRI and SRO represent the bulk of the cells inside the enamel organ.

2.2.3 *Sci-RNA-seq reveals spatio-temporal expression patterns of critical signaling pathways in ameloblasts and facilitates the development of human iPSC-derived ameloblasts (iAM) in vitro*

To understand the signaling pathways involved in ameloblast differentiation, we compiled a comprehensive multiplexed analysis pipeline based on ligand-receptor interactions and downstream transcriptional activity (Figure 2.18). Briefly, a *talklr* (Wang, 2020) R package was used to identify specific ligand-receptor communications between the cell types at each developmental time point. DEsingle (Miao et al., 2018) and *scMLnet* (Cheng et al., 2021) programs were used to evaluate the downstream signaling activity by establishing multilayer networks between ligands and receptors and between transcription factors and their differentially expressed targets. Finally, activity scores were assigned to each pathway, which represent a percentage (0-100%) of the overall activity for all pathways included in the analysis.

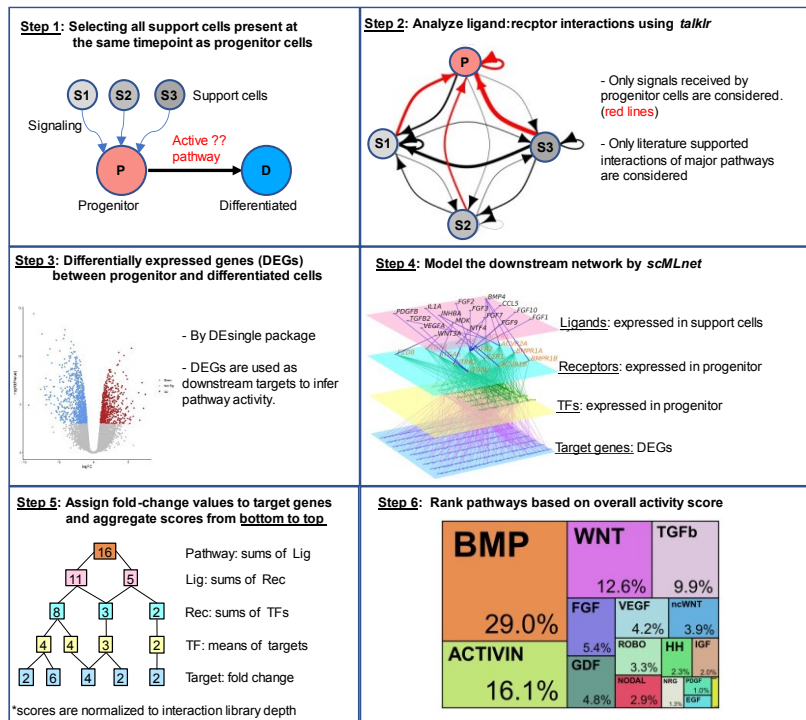


Figure 2.18. Top pathway analysis work flow

A schematic for the computational workflow to identify critical pathways at different stages.

The most active signaling pathways involved in ameloblast differentiation were identified to be BMP, WNT, EGF, TGFb, HH and FGF.

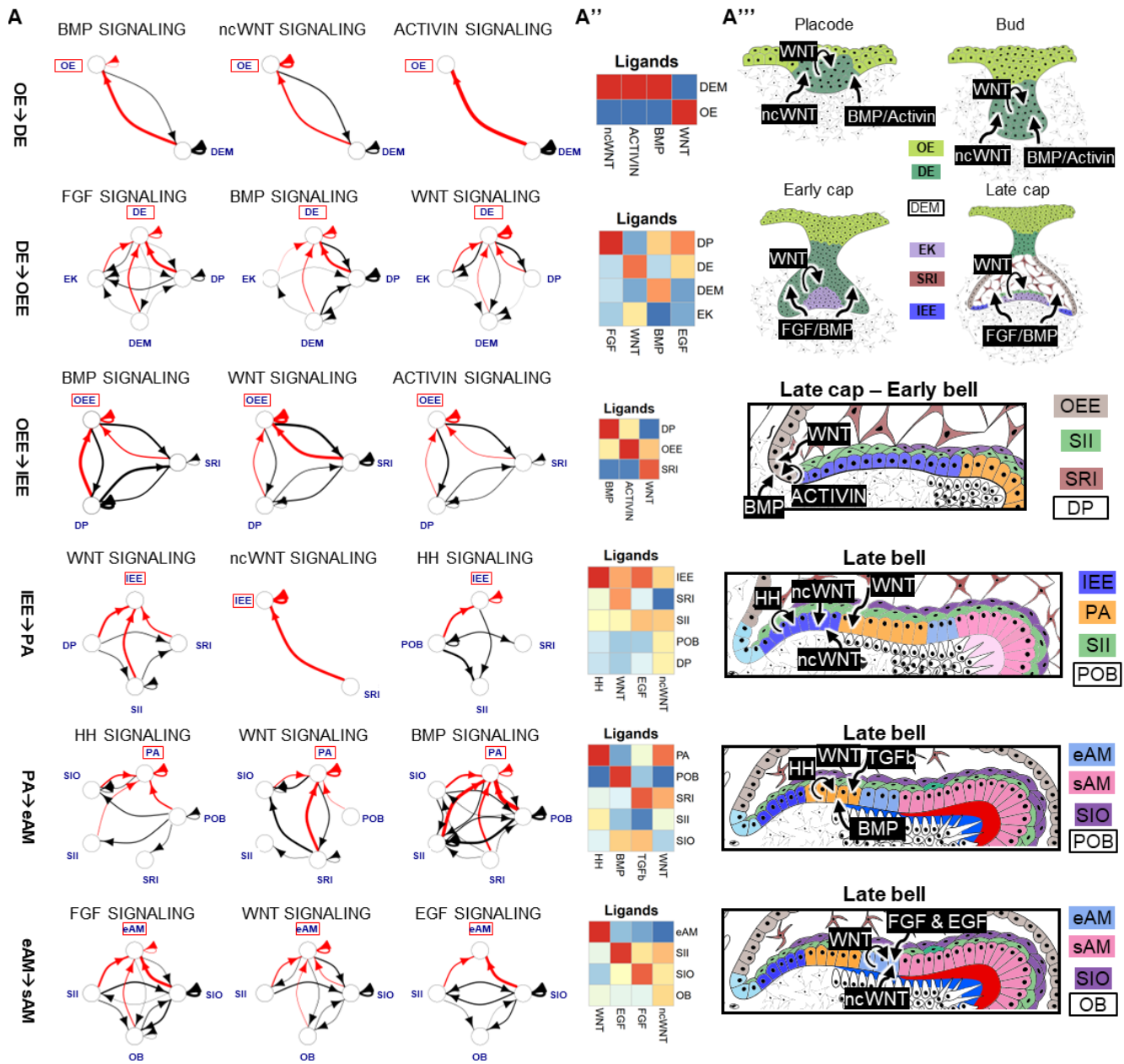


Figure 2.20. The sources of ligands.

(A) The sources of critical signaling ligands for the top three pathways involved for each developmental stage originate from both the dental epithelium and mesenchyme derived tissues, with the thickness of the line indicating the number of ligand:receptor interactions, arrowheads indicating the cell possessing the receptor, and interactions of interest (red) and between support cells (black). (A'') Heatmaps for the top three or four pathways were generated by aggregating pathway ligand gene expression, which is then averaged per cluster. (A''') Diagrams illustrate the suggested ligand sources for each pathway at varying stages of tooth development.

Based on the signaling pathway prediction analysis, we found that BMP, ncWNT and ACTIVIN pathways are most active during OE to DE transition. However, ncWNT and ACTIVIN pathways down-regulate during DE to OEE transition when FGF and WNT pathways become more prominent. During the OEE to IEE stage transition, BMP is the most active, followed by WNT and ACTIVIN pathways. Meanwhile, in IEE to PA stage, mostly WNT (40% including canonical and non-canonical), HH (17%), and EGF (10%) become more active. In PA to eAM transition, the HH is the most active at (35%), followed by WNT, BMP and TGF β . To analyze the maturation stage, we evaluated the pathway activities between eAM and sAM clusters and found that FGF, WNT and EGF signaling are involved in ameloblast maturation (Figure 2.19 and Figure 2.20). Our analysis of the stages of ameloblast development reveals a critical function for support cells, SI, SR and mesenchyme signaling: BMP and ACTIVIN from mesenchyme are involved in the transition from OE to DE, ncWNT from DE, and support cells and BMP again from mesenchyme in the transition from DE to OEE, and from OEE to IEE. Similarly, IEE to PA differentiation utilizes specific accompanying SII to secrete ncWNT/EGF and WNT from SRI (Figure 2.19 and Figure 2.20). In last stages of ameloblast differentiation, from PA to eAM, PA and SII secrete HH ligands, while SRI and SIO secrete TGF β . At the final maturation stage, from

eAM to sAM, SII secretes EGF & SIO secretes FGF. Interestingly, WNT activity in the transition of OEE to IEE (Figure 2.20.A''') can be linked to the emergence of SP6 expression in IEE in the junction of the cervical loop (Figure 2.21.A). WNT pathway has been suggested to work upstream of the expression of the transcription factor SP6 (Aurrekoetxea et al., 2016; Haro et al., 2014; Ibarretxe et al., 2012), which in turn was found to interact with AMBN/AMELX promoters (Rhodes et al., 2021) (Figure 2.21.A-D). Additionally, we found that SP6 is mostly localized in the cytoplasm of the early stages IEE/PA. However, in later stages, SP6 is localized to the nuclei coinciding with AMBN expression in eAM/sAM (Figure 2.21.F). These data support the hypothesis that SP6 expression is induced by WNT pathway already in IEE transition stage, but becomes functional in eAM stage when it translocates to the nucleus and induces AMBN expression. Future loss-of-function analysis is required to test this hypothesis. Together these data suggest that WNT, TGF β , HH, FGF, and BMP pathways are the top active pathways in ameloblast development compared to all 25 pathways included in the analysis.

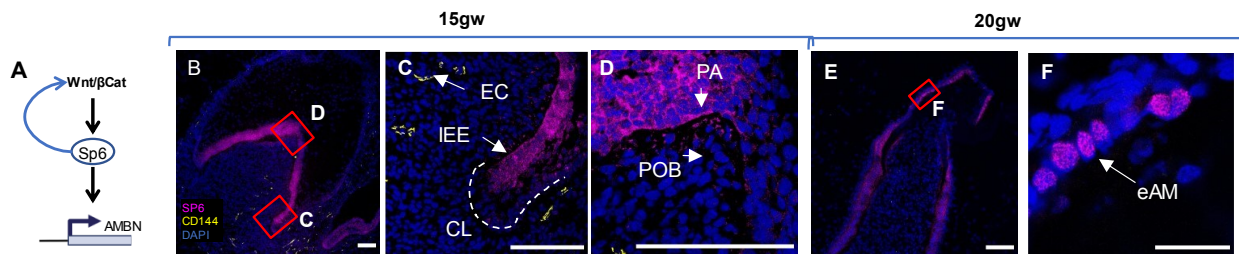


Figure 2.21. WNT pathway in ameloblasts development.

(A) Diagram for the proposed involvement of WNT pathway in activating the expression of SP6 which subsequently activate AMBN expression. Immunofluorescence staining of SP6 in 15gw tooth germ (B-D) confirm the start of expression of SP6 in cytosol of IEE where we predict the initiation of WNT activity in Figure 2.21.A''' at (OEE→IEE), in the region of CL. Endothelial cells (EC) are present within the developing dental pulp at the same stage. At 20gw, SP6 is mainly localized to the nuclei coinciding with the onset of AMBN expression in differentiated AM at the tip of the toothgerm (E-F). Scale bars: 50µm.

We utilized the inferred signaling pathways from the sci-RNA-seq data (Figure 2.19 and Figure 2.20) to develop a novel in vitro differentiation protocol that recapitulated the early stages of human ameloblast development from hiPSCs (iAM differentiation; Figure 2.22). We first optimized a protocol to differentiate iPSC into OE (Ochiai et al., 2015; Suga et al., 2011; Tanaka et al., 2018). At day10 of differentiation, the OE markers were upregulated, while pluripotency markers were downregulated, and neuroepithelial and early mesodermal markers remained unchanged (Figure 2.23). To differentiate the OE cells into an early stage ameloblasts, we activated the main pathways we identified (Figure 2.19) from the OE stage to the PA stage (BMP4, TGFβ1, WNT/CHIR99021, EGF, and HH/SAG pathways in the order of their activity during differentiation (Figure 2.22). This differentiation procedure resulted in marked epithelial morphological changes and a high expression of the ameloblast early marker AMBN at day 16 in the differentiation (Figures 2.22; 2.24; 2.25), indicative of the early ameloblast differentiation stage.

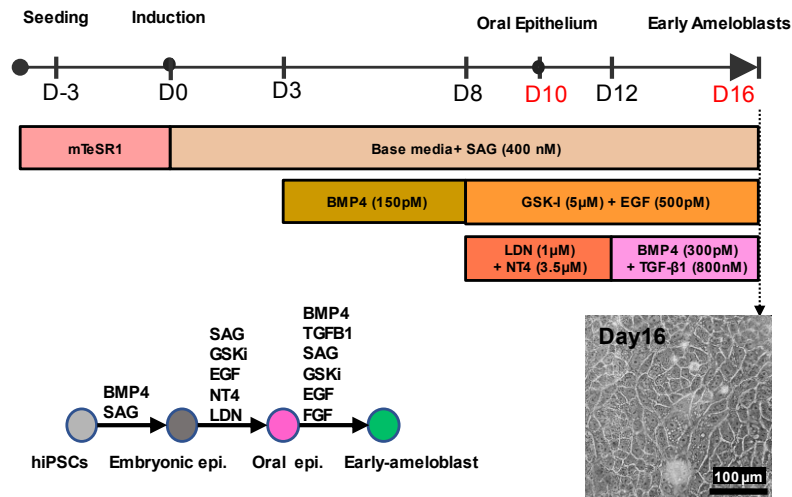


Figure 2.22. Induced ameloblast (iAM) differentiation protocol.

Schematic of the 16-day differentiation protocol, which targets the identified signaling pathways utilizing growth factors and small molecules to transition through the ameloblast developmental stages.

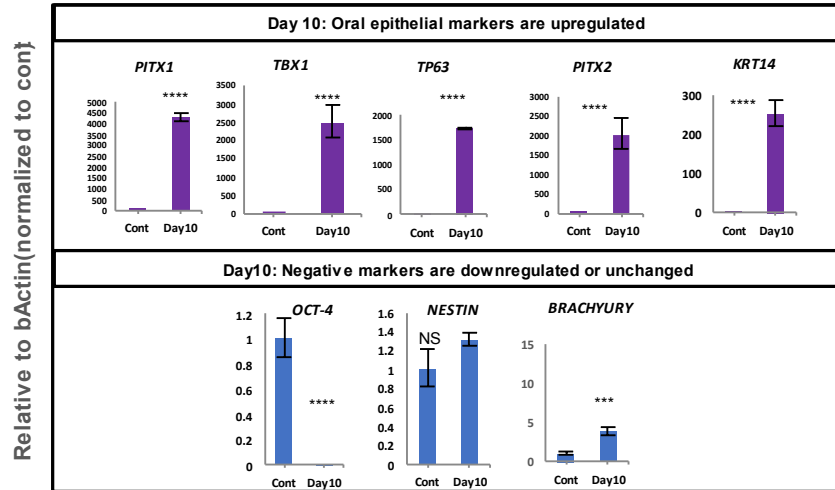


Figure 2.23. QRT-PCR of oral epithelial markers.

Cells at Day 10 of differentiation show upregulated expression of oral epithelium markers *PITX2*, *PITX1*, *TBX1*, *TP63* and *KRT14* as assessed by QRT-PCR compared to undifferentiated hiPSCs, concomitant with a significant decrease in known pluripotency marker *OCT-4*. Additionally, the neuroepithelial marker *NESTIN*, and the early mesodermal marker *TBXT* (*BRACHYURY*) are relatively unchanged at day10 of the differentiation, indicative of a relatively lineage-specific differentiation. Each study was performed in triplicate. Significance was determined by unpaired Student's t-test; *** $p < 0.001$; **** $p < 0.0001$; Graph error bars are the means \pm SEM.

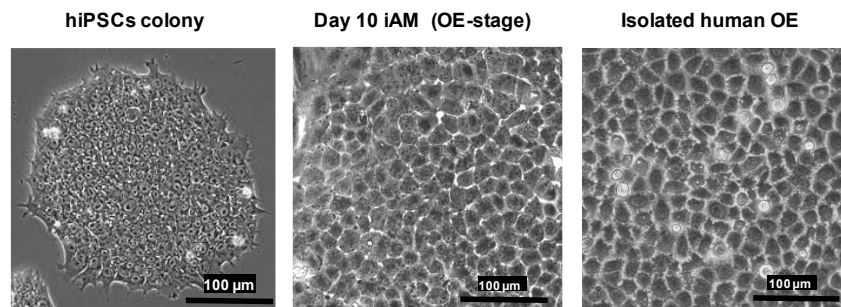


Figure 2.24. Morphology of differentiated cells.

Brightfield images of hiPSCs, day 10 of *in vitro* differentiation, and isolated fetal oral epithelium after culturing for seven days show that oral epithelium differentiated from iPSCs exhibit the same morphological characteristics as culture human oral epithelium.

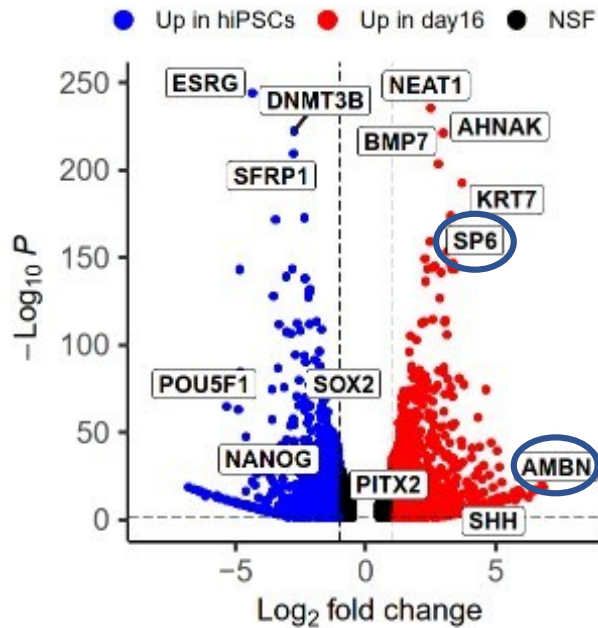


Figure 2.25. RNA-seq of day 16 cells.

The cells at day 16 of differentiation show upregulation of ameloblast markers *SP6* and *AMBN* as assessed by bulk RNA-seq compared to undifferentiated hiPSC control.

To dissect which pathways were essential for the differentiation from day10 to day16, we used the process of elimination (Figure 2.26). When removing EGF, SAG, BMP4, or TGF β 1 independently, we found that the expression of *AMBN* is significantly reduced to less than half compared to when all factors are present. However, removing GSKi completely abolished *AMBN* expression, suggesting that WNT signaling is a master regulator upstream to other pathways (Figure 2.26). Our pathway prediction pipeline also suggested that the FGF pathway is heavily involved; however, adding bFGF had no significant effect on *AMBN* expression (Figure 2.26). We hypothesized that the cells in culture secrete enough FGF ligands to saturate the receptors, and any exogenous ligands would have minimal effects. To test this hypothesis, we used a computationally designed protein, FGFR2 mini-binder (FGFR-mb), that specifically binds and inhibits the activity of the FGFR2 (Cao et al., 2022). Adding the FGFR2-binder almost totally

abolished the expression of *AMBN*, which shows that the *FGFR* pathway is indeed required for ameloblast differentiation (Figure 2.26). This marks the importance of highly specific AI-designed mini-proteins in analyzing the requirement of signaling pathways in differentiation. It is plausible that temporal preciseness and high penetrance, combined with specificity of designed mini-binders to their targets may partially out-compete in the future genetic perturbations of signaling pathway in iPSC derived differentiation paradigms.

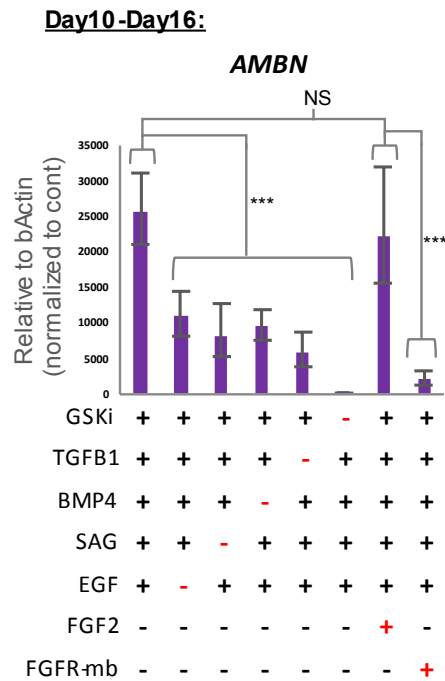


Figure 2.26. Importance of each pathway in iAM differentiation.

The efficiency of each pathway activated in the differentiation from day10 to day16 were assessed by removing each agonist one at a time or adding *FGFR2* mini binder to inhibit the *FGFR2* pathway. *AMBN* expression was assessed in QRT-PCR, and each condition was performed in triplicate. Significance was determined by unpaired Student's t-test; *** $p < 0.001$; **** $p < 0.0001$; Graph error bars are the means \pm SEM.

To analyze the efficiency of the differentiation, we performed sci-RNA-seq on Day10 and Day16 of iPSC derived ameloblast differentiation (day10-OE and day16-Early-ameloblasts) and

compared the gene expression data to the fetal tissue gene expression data. Our initial clustering and trajectory analysis indicated three major clusters at day10 and six clusters at day16 (Figure 2.27.A-B). Sequencing revealed a significant overlap between human fetal and iPSC-derived ameloblasts in 2D culture. A survey of relevant markers to the dental epithelium (Figure 2.27.C-D) showed the kinetics of their differential expression across the proposed trajectory (Figure 2.27.A-B). Utilizing the markers for the oral/dental epithelial progenitors (Sun et al., 2016; Yu *et al.*, 2020), enamel epithelium (Nakamura et al., 2017), and ameloblasts (Seidel et al., 2010), we were able to identify all the differentiated cell types (Figure 2.27.A-B). For a better comparison between the *in vivo* and *in vitro* datasets, we used the projection method in Seurat 4.0 and the integration method in LIGER software packages (Hao et al., 2021; Welch et al., 2019) to overlay the datasets. We converted our dataset from Monocle3 format to Seurat format; then, we performed the projection over the UMAP of the fetal dental epithelium lineage. Lastly, we classified the projected cells using graph-based clustering. A small proportion of the cells in the day16 sample were OE-like, DE-like, SR-like, and SI-like. However, the majority (60%) were PA and AM-like, indicating that most of the differentiated cells are directed toward the ameloblast lineage (Figure 2.28). We performed river plot analysis using LIGER to show the relationship between the annotated clusters from the fetal dental epithelial lineage and the *in vitro* day16 differentiation clusters that share the same space in LIGER joint clusters (Figure 2.29), which allows label matching for the unannotated clusters in the differentiation (Figure 2.30). Interestingly, the fetal OE cluster matched cluster 1 (d16_1; Figure 2.28.B) in *in vitro* differentiation; the DE, SR, and OEE from *in vivo* samples mainly matched cluster 2 (d16_2) and SI matching cluster 4 (d16_4). The pre-ameloblast and ameloblast clusters matched clusters 5 and 6 (d16_5, d16_6), respectively, which represent 47% of total cells (Figure 2.30). Finally, we analyzed the functionality of the iAM

by analyzing the number of cells in day16 differentiated samples that produced AMBN, the product secreted by ameloblasts. Notably, 25% of the cells in 16 days of differentiation can produce and, in some cases, secrete AMBN protein (Figure 2.31). This analysis suggests that our iAMs share similarities with fetal pre-ameloblasts and ameloblasts, demonstrating that the described 2D procedure can generate early differentiated ameloblasts.

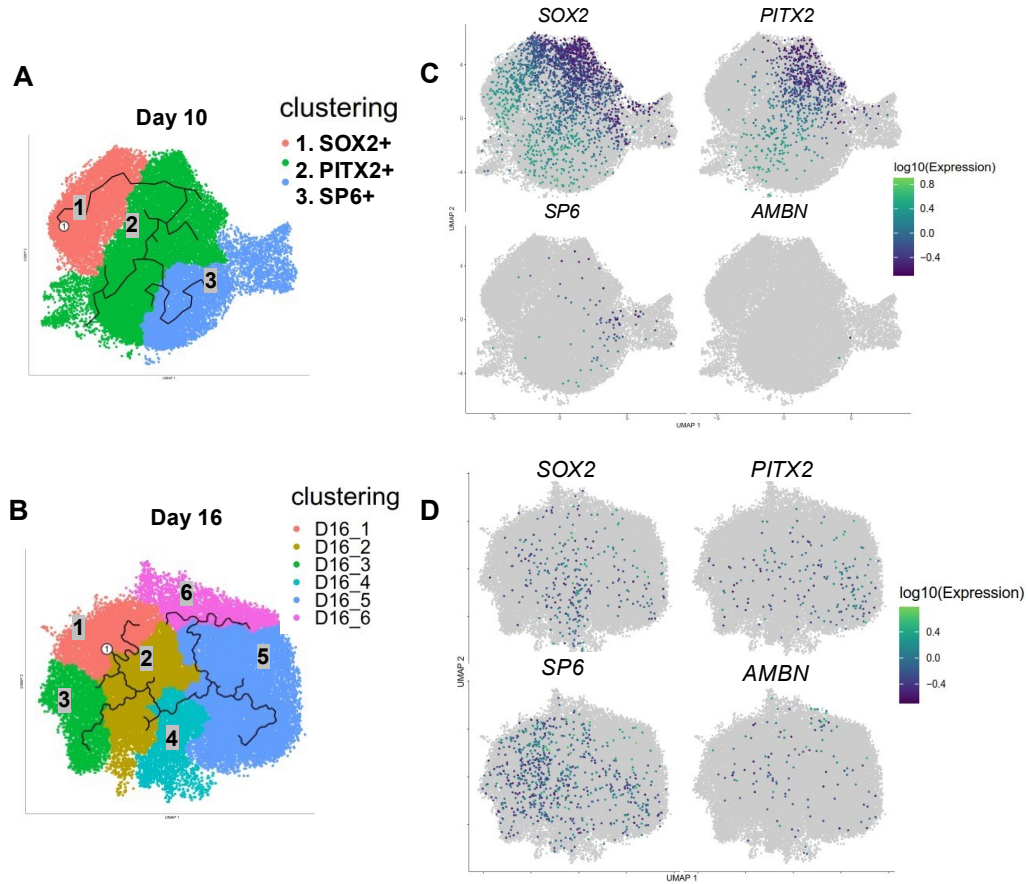


Figure 2.27. sci-RNA-seq for differentiated samples

Day 10 (A) and Day 16 (B) samples were sequenced with sci-RNA-seq. Cells were clustered and analyzed to identify clusters with similar gene expression patterns to known cell types in fetal development. Gene expression density plots for known markers of different phases of ameloblast development show continuity between day 10 and day 16, with early markers *SOX2* and *PITX2* being predominantly expressed by day 10 (C) and shifting toward ameloblast-specific markers *AMBN* and *SP6* in day 16 (D).

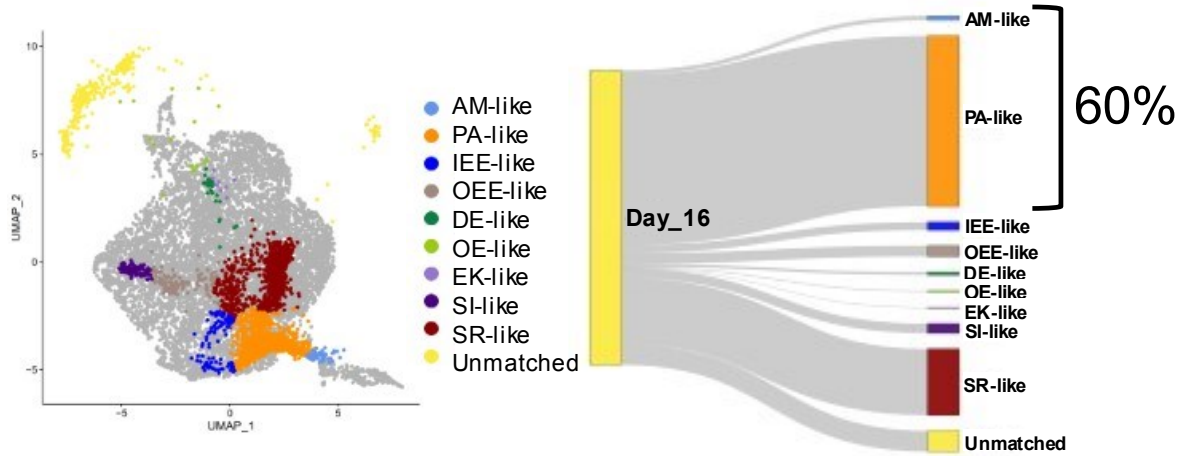


Figure 2.28. Projection of Day16 into UMAP of fetal AM lineage

Projection of the sequenced Day 16 *in vitro* differentiated cells into the UMAP space of the *in vivo* dental epithelium derived cell types (Figure 2.8) which suggests 60% of Day 16 cells share gene expression pattern of PA and eAM. Projection was done with Seurat 4.0.

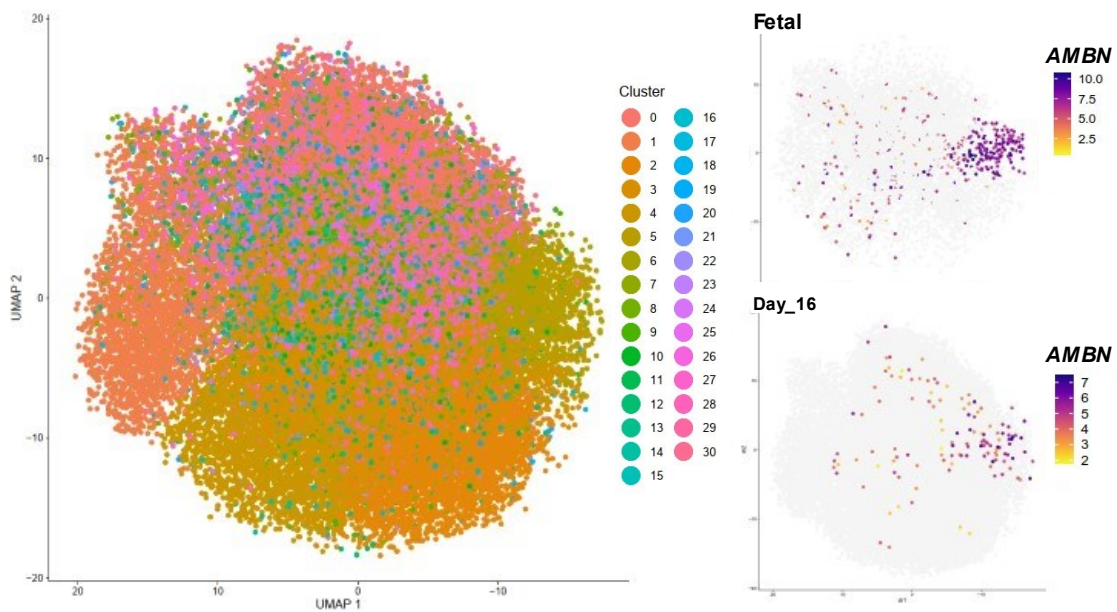


Figure 2.29. Integration of Day16 with fetal AM lineage

LIGER joint clustering analysis of Day 16 differentiation cells and the *in vivo* human fetal dental epithelium (Figure 2.8) derived cells suggests the colocalization of *AMBN* expressing cells from *in vivo* and *in vitro* in cluster 6.

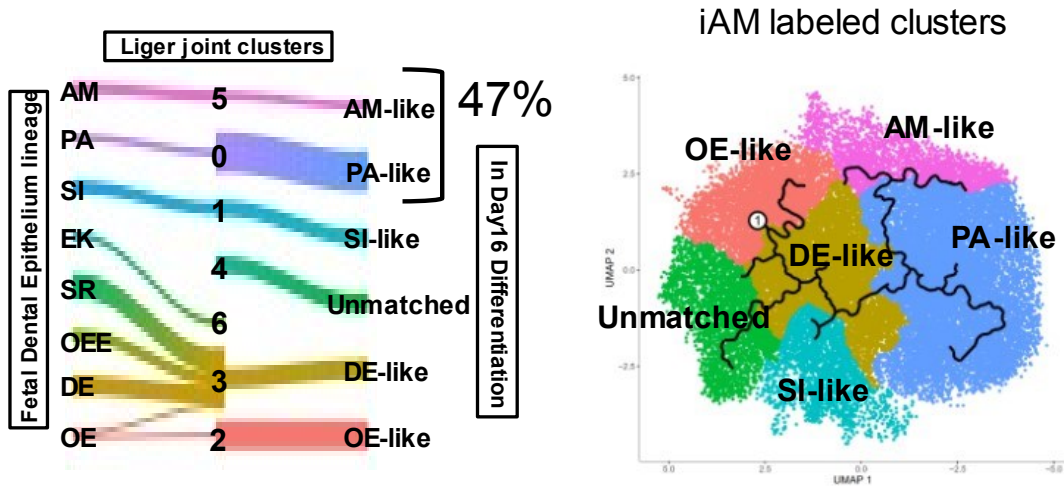


Figure 2.30. LIGER river plot and labeled Day 16 clusters

LIGER joint clustering analysis suggests 47% of Day 16 cells share gene expression pattern of AM and PA, which allowed the labels to be transfer and annotate the cell types identity on iAM Day 16 differentiation UMAP graph.

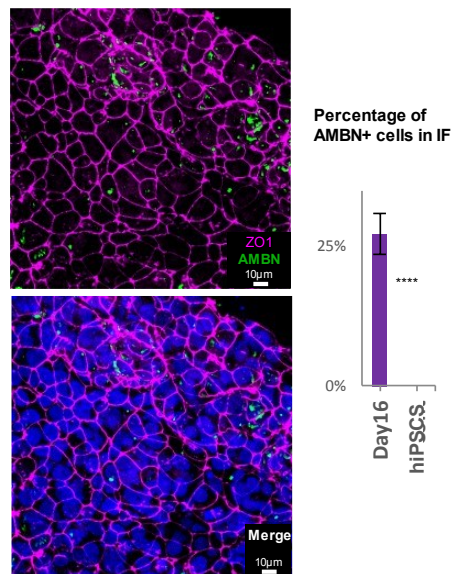


Figure 2.31. Percentage of AMBN+ cells in Day 16

Immunofluorescence staining of day 16, showing AMBN expression, and the membrane marker ZO1, with quantification analysis finding approximately 25% of cells positive for AMBN expression. Each study was performed in triplicate, with error bars representing \pm SEM. Significance was determined by unpaired Student's t-test; **** $p < 0.0001$

2.2.4 3D Enamel organoids show mineralization and Ameloblastin, Amelogenin, and Enamelin secretion

To further characterize iAM and evaluate their capacity to mature *in vivo*, we injected the differentiated cells (day16, 2D) intramuscularly into adult SCID mice and allowed the injected cells to develop for 8 weeks (Figure 2.32.A). The injected region was identified by human nuclear antigen staining (Figure 2.32.B). The maturation stage of the iAM cells was analyzed in the subsequent serial sections by definitive ameloblast markers: AMELX, AMBN, DSPP, KRT14, and by its calcification capacity. Importantly, the identified iAM cells were significantly more mature (Figures 2.32.B-E and 2.33), showing that the iPSC derived iAM cells have a capacity to develop to a more mature AM stage. The highly elongated morphology of these cells (Figure 2.32.D) suggests that they have developed into so-called secretory stage AM (sAM) that characteristically consists of tall columnar cells that express amelogenin (AMELX) and (AMBN) and produce mineralization. Accordingly, we further identified iAM capacity to produce calcified material via Alizarin red and Von Kossa staining (Figures 2.32.E and 2.33.G).

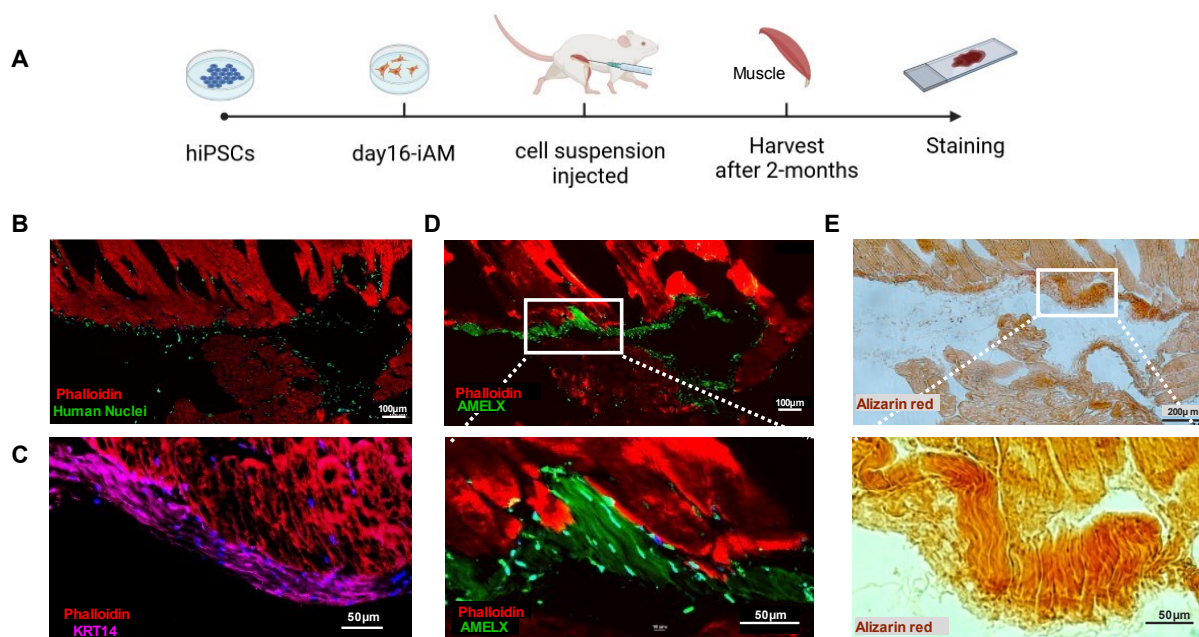


Figure 2.32. iAM transplantation into *in vivo* mouse model

(A) Schematic of the mouse *in vivo* experiments describing the steps for injecting day16-iAM subcutaneously into the left legs muscle of the adult SCID mice. The adult SCID mice at 2-month-old were dissected at the site of injection to perform further analysis to locate the cells such as immunofluorescence staining for human nuclear antigen in (B), KRT14(C), AMELX (D) and Alizarin red staining in (E) showing mineralization.

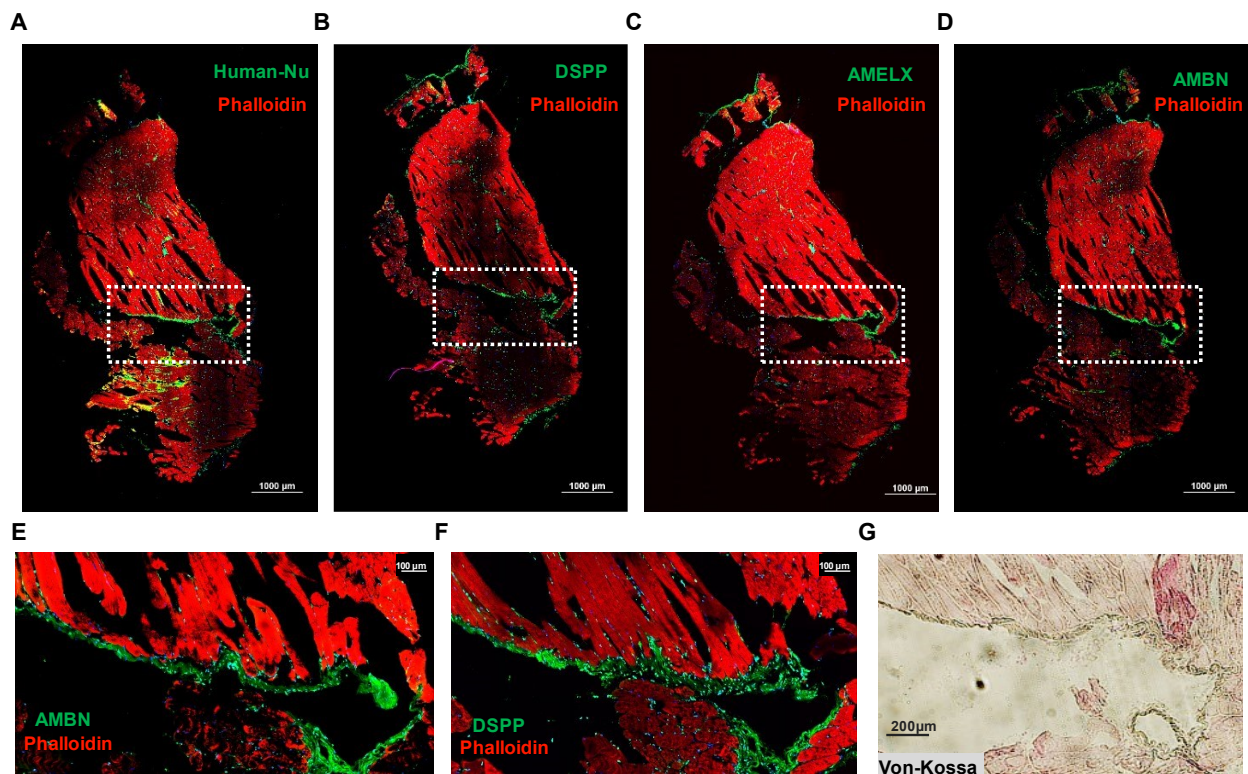


Figure 2.33. Mouse *in vivo* experiments (continued)

(A-D) Immunofluorescence staining shows the entire surface area of the stained muscle sections in Figures 6B–6E. The dotted boxes indicate the area of interest magnified in Figure 2.32 and in (2.33.E–G) for AMBN and DSPP. Von-Kossa staining for calcification was performed in a subsequent section in (G) showing black/brown staining localized to the injected cell region.

Since close contact between AM and OB is critical for tooth development, we proceeded towards developing an organoid model of the two cell types. We first developed an organoid model

of polarized AM. To generate cells expressing AMBN in a culture with apical-basal polarization, similar to ameloblasts *in vivo*, we grew the cells in suspension to form spheroids (Figure 2.34.A). We then performed immunofluorescence staining for SP6, AMBN (Figure 2.34.B), and ZO1, DSPP (Figure 2.34.C). We observed that the transcription factor SP6 is expressed in all the differentiated cells and is exclusively localized to the nucleus. The induced ameloblasts show apical-basal polarity and secrete AMBN to the apical surface. As seen in *in vivo* AM, the nucleus is located towards the basal side of the cell (Figure 2.34.C-D). Early ameloblasts are known to transiently express DSPP during development (Figure 2.7.C; Figure 2.15.A); we noticed that DSPP expression is also localized to the apical side of the induced cells. Moreover, the tight junction protein ZO1 marks the apical side of these iAM cells (Figure 2.34.C-D). The iAM in the organoids appear as tall columnar cells polarized toward a central lumen (Figure 2.34.D).

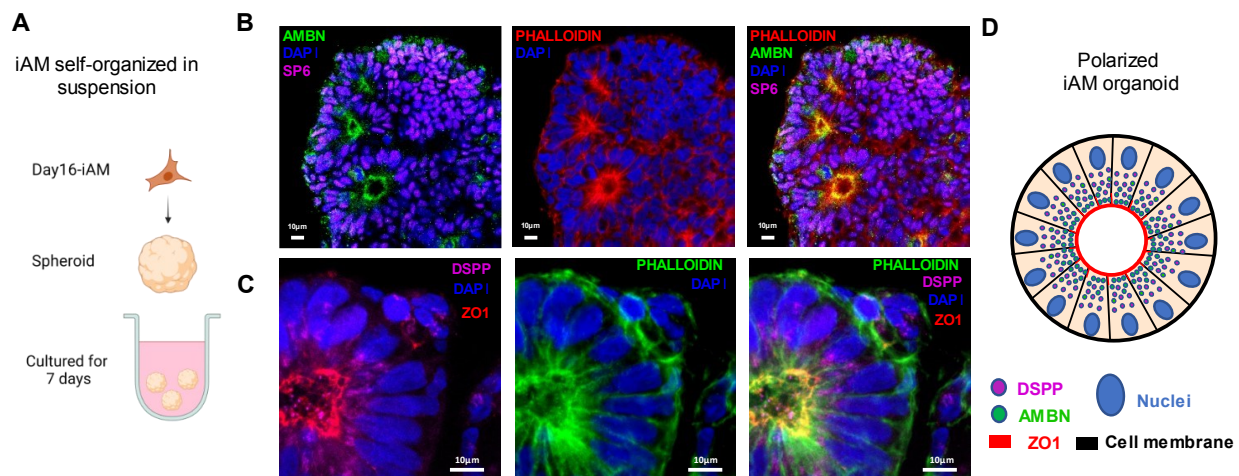


Figure 2.34. iAM organoids formation.

(A) Schematic of iAM organoids formation while cultured in suspension in ultra-low attachment plate. The formed iAM organoids express SP6 in the nuclei and secrete AMBN (B), and DSPP toward the apical side indicated by ZO1 (C). (D) A diagram simplifying the iAM organoid polarized structure toward a central lumen marked by ZO1, and the secretory vesicles of DSPP and AMBN.

We next co-cultured the induced ameloblast organoids with primary human dental pulp stem cells (DPSCs) to assess the interaction level between the two cell types and the effects on ameloblast maturation. We found that simple coculture in suspension can induce AMELX in iAM organoids and DSPP in the odontoblast organoids, as observed in the developing human tooth; as well as induction of calcified matrix (Figure 2.35). After confirming that iAM can mature in the presence of OB/DPSCs, we designed the following experiment to coculture the cells in a layered approach. We plated the DPSCs in the bottom of a flat bottom plate and then embedded iAM organoids in a Matrigel layer above the DPSCs (Figure 2.36.A). The co-culture media contained iAM and odontogenic media at 1:1 ratio, with calcein in addition to detect calcification. Through 3D reconstructed confocal images, we observed that iAM are associated with calcein, demonstrating the capacity of iAM to produce mineralization/calcification (Figure 2.36.B). Furthermore, the co-cultured iAM expressed ENAM and AMELX (Figure 2.36.C-D) and reverted their polarity towards the differentiating OB (Figure 2.36.D-E). This 3D organoid, therefore, mimics the normal cell-to-cell interface observed in developing tooth where the enamel proteins are secreted towards the OB and sets the stage towards developing human tooth organoids in a dish.

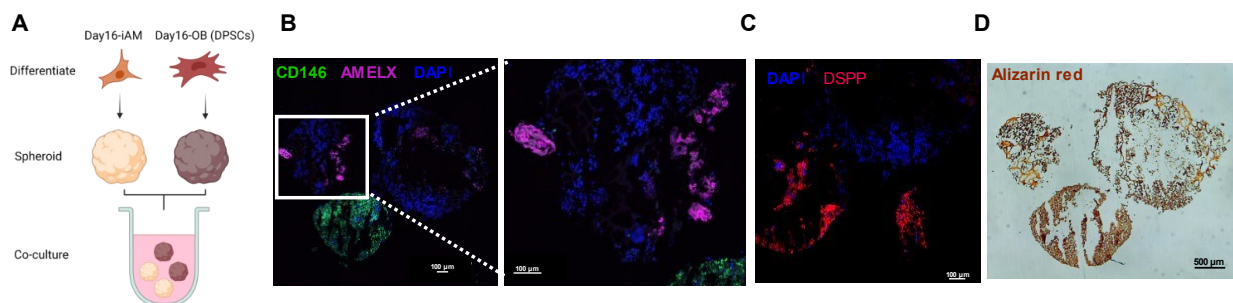


Figure 2.35. iAM/DPSC-OB organoids coculture.

(A) A schematic for the coculture experiment between iAM organoids and DPSC organoids in suspension culture where each cell type was formed in separate wells and then combined for 14 days in iAM base media. Organoids were snap frozen, cry-sectioned, and prepared for immunofluorescence. Expression of AMELX was noted in iAM organoids (B) and CD146 and DSPP in DPSC/OB organoids (C). Alizarin red staining (D) indicates the classification is positive in both organoid types, particularly DSPC/OB, which shows more calcifications.

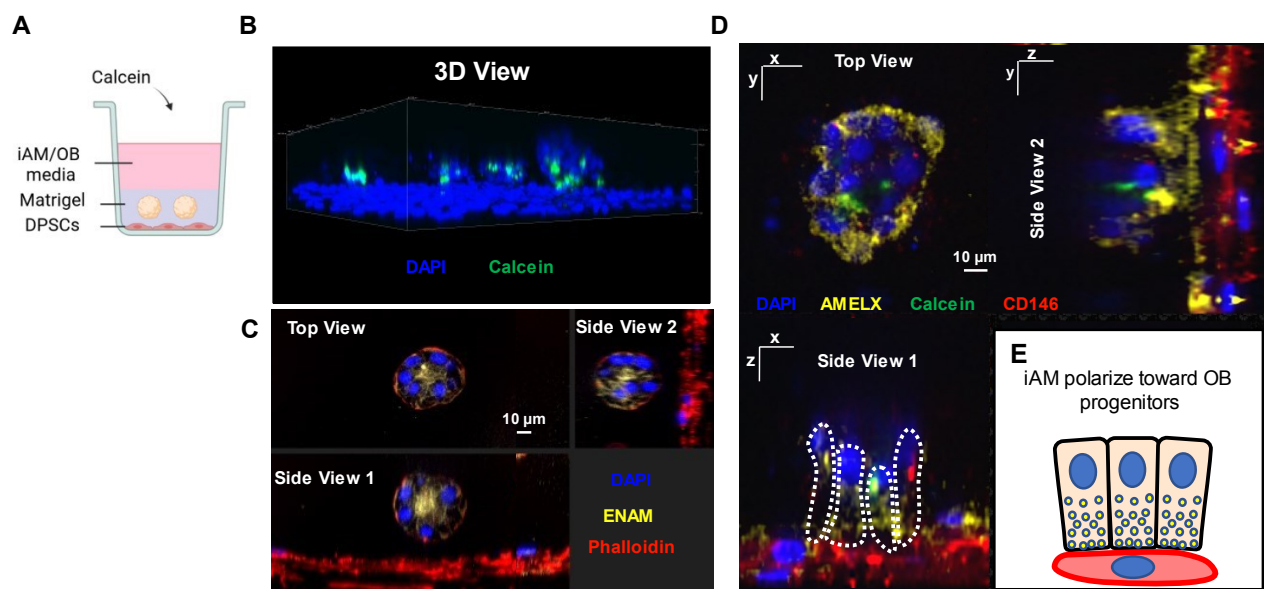


Figure 2.36. iAM/DPSC-OB coculture and polarity switch.

(A) Schematic for the coculture experiment between DPSCs as monolayer and iAM embedded in Matrigel above it. Calcein, which is a fluorescent dye that binds to calcium, was added to the media containing iAM base media and odontogenic media in 1:1 ratio. (B) 3D reconstructed image from z-stacked confocal images captured from the coculture experiment plate. The cocultured organoid show association with Calcein, as well as expression of ENAM at the center after 7 days (C), and after 14 days the organoids close to CD146-expressing DPSC/OB, started to revert polarity towards DPSCs/OB while expressing AMELX (D) as simplified in the diagram in (E).

2.3 DISCUSSION AND CONCLUSIONS

Functional ameloblasts and odontoblasts are two critical cell types secreting the protective tooth coverings, enamel, and dentin, that are required to generate the functional structure of teeth. Ameloblasts do not exist in adult oral structures, making enamel regeneration impossible; however, dentin-secreting odontoblasts are critical for the regeneration of adult teeth. While previous morphological studies have suggested that two cell types can give rise to odontoblasts, the developmental lineages and molecular characterization of this process were not understood. Here we generate and utilize single-cell sequencing to identify the cell types in the developing human tooth and their molecular interactions across several developmental stages. We identified the major cell types in human oral development that derive from the jaw tissue and give rise to teeth and salivary glands. Importantly, we identified novel human support cell types that significantly and precisely promote the differentiation of ameloblasts. Analyzing the signaling interaction in the ameloblast trajectory allowed us to predict the signaling molecules needed to recapitulate ameloblast development *in vitro*. Utilizing these findings, we developed a novel differentiation protocol to drive the differentiation of iPSCs toward early ameloblasts (iAM). We successfully verified their identity by comparing the expression profile of the *in vitro* generated ameloblast lineage to the *in vivo* fetal counterpart. Finally, we used this information to develop an enamel organoid that expresses mature ameloblast markers and secretes mineralized calcium.

The sci-RNA-seq data revealed novel transcriptionally defined subgroups of cells in both the epithelial and mesenchymal lineages. Our analyses identified 13 subclusters of cell types in the dental epithelial lineage, of which SRI, SRO, SIO, and SII are novel types of support cells in human tooth development. The newly identified support cell type, SRI, produces a TGF β ligand

at an early stage of tooth development to aid in the differentiation of IEE to PA. While SII secrete EGF and SIO secrete FGF ligands at later stages to aid in the maturation of AM. Our data have amended the detail with which we understand how support cells contribute to the patterning and development of ameloblasts.

For the first time in human tooth development, our studies have revealed, in extreme detail, the signaling pathways that govern each transition between cell identity. Previous studies of hypodontia and tooth agenesis have shown that disruption of WNT, BMP, and FGF signals results in defective tooth development. However, the detail with which our study has revealed the role of these pathways at various points in development may more mechanistically explain how defects in these pathways lead to tooth loss or tooth agenesis. For example, studies have shown that mutations in BMP4 correlated to tooth agenesis (Yu et al., 2019a). Our analysis showed that BMP4 signaling is critical during the early stages of both the OE to DE and DE to OEE transition, suggesting that loss of BMP4 may lead to agenesis by disrupting these transitions. In other studies, disruption of FGF signaling leads to enamel irregularities (Marangoni et al., 2019). Using AI-based protein design, we now revealed that FGF signaling is essential at the point of ameloblast maturation, suggesting that these irregularities are a result of failure of ameloblasts to mature. While some studies have focused on the role of a single signaling pathway, many others have highlighted the importance of crosstalk between pathways in tooth development and maintenance (Liu et al., 2020; Malik et al., 2018; Yu et al., 2019b). Our predictive pathway analysis highlights not only the primary pathway responsible for each stage but also ranks the other pathways involved. Overall, our study will facilitate the investigation into both previously identified and yet undescribed crosstalk in driving forward development. The detailed analysis we have provided in

this study will facilitate more detailed and informed studies on degenerative dental diseases and can lead to developing more effective ways to mitigate or reverse tooth loss. Furthermore, our work with AI-designed, de novo receptor mini-binders that specifically bind and inhibit target receptor signaling (Cao *et al.*, 2022) now reveals a novel, highly simplified method to identify the exact stage of a specific signaling pathway required in the differentiation process. The method described in this study using the de novo FGFR-mb to unravel the FGFR pathway requirement in Ameloblast maturation will be generally applicable and specific to any signaling pathway analyzed in the differentiation of normal and disease organoids.

Ameloblasts secrete the most mineralized and highly vulnerable layer in the human tooth. However, this cell type, and hence enamel regeneration, is absent in adult humans, presenting an impasse for progress in human regenerative dentistry. Our studies have revealed multiple new potential avenues through which further study could overcome this. First, our studies present the first single-cell analysis and *in vivo* localization of the cervical loop in human fetal teeth. The cervical loop is part of the enamel organ in the developing tooth located where the OEE and the IEE join. It has been extensively studied in the mouse, most often in the mouse incisor. However, unlike the human tooth, the mouse incisor grows continuously, with the cervical loop serving as a reservoir of stem cells that contribute to that consistent growth. Therefore, it is necessary to understand the function and contribution of the cervical loop in human tissue. Classically, the cervical loop is known to give rise to Hertwig's Epithelial Root Sheath, which initiates root formation. Intriguingly, our analysis revealed a role for the CL in giving rise to human ameloblasts in early tooth development, as the crown expands before the root begins to form. Our findings

provide a basis for future studies to develop cervical loop-like cells with ameloblast lineage potential.

Finally, the present work characterized the molecular basis for human ameloblast differentiation. We have used this knowledge to develop an assay for differentiating human iPSC-derived ameloblasts in a dish (iAM). Comparing fetal data to the iAM differentiation suggests that iAM shares high similarity with fetal pre-ameloblasts and early ameloblasts. Further, iAM can reach the secretory stage since Ameloblastin protein production and secretion is observed in these cells. In addition, the iAM cells showed a significant increase in maturation, including calcifications, when tested *in vivo*. Upon co-culturing iAM and OB lineage we observed the iAM reverting their polarity and apical secretion of enamel proteins toward the OB lineage cells. Hence, we argue to have developed a chemically defined serum-free differentiation protocol to generate human dental epithelium, and their subsequent differentiation into enamel organ-like 3D organoids. This developed organoid has potential for future dental therapies.

The first human single-cell tooth development atlas described here paves the way toward successful human regenerative dentistry in the future. The molecular analysis and *in vitro* ameloblast differentiation protocol allow future dissection of diseases such as Amelogenesis Imperfecta that will guide the field toward therapeutic approaches.

2.4 MATERIALS AND METHODS

2.4.1 *Tissue collection and dissection*

This study is approved by the Institutional Review Boards (IRB) at University of Washington for the use of human fetal tissues: BDRL (CR000000131) and Ruohola-Baker Laboratory (STUDY00005235). Fetal craniofacial tissues were collected from Birth Defect Research Laboratory (BDRL), University of Washington, and transferred to Ruohola-Baker laboratory submerged in Hank's Balanced Salt Solution (HBSS) media (Gibco, #14025092) on ice. Toothgerms and salivary glands were dissected in cold RNase free Phosphate-Buffered Saline (PBS) (Invitrogen, #AM9624) within six hours from the initial dissection at BDRL. To extract the toothgerms, a vertical cut was made at the midline of the upper/lower jaw for orientation, then a horizontal cut was made from the right side of the midline along the top of the alveolar ridge to expose one toothgerm at a time. The first two toothgerms from the midline were the incisors, the next toothgerm was the canine, and the last two toothgerms were the molars. The same procedure was followed to extract toothgerms on the left side of the jaw. The submandibular salivary glands were harvested from the distal end of the lower jaw. The toothgerms from 9 to 11 weeks old were too small for dissection and not useable for sequencing; therefore, these jaws were cut into two posterior sections and one anterior section to separate molars from the incisors and canines at these timepoints. The extracted tissues were transferred into an Eppendorf tube and snap frozen using liquid nitrogen. The frozen samples were stored at -80°C until nuclei extraction.

2.4.2 *Nuclei extraction*

Frozen tissues were carefully transferred to a stack of chilled aluminum foil kept on dry ice to prevent thawing. The folded foil encapsulating the tissues were placed on a block of dry ice and the foil was pounded with a pestle to pulverize the tissues into powder. 1mL of lysis buffer that contains nuclei buffer (10 mM Tris-HCl, 10 mM NaCl, 3 mM MgCl₂, pH 7.4), 0.1% IGEPAL CA-630, 1% SUPERase In RNase inhibitor (20 U/μL, Thermo), and 1% BSA (20 mg/mL, NEB) were added onto the tissue powder and transferred to a 1.5mL tubes. Samples were incubated in the lysis buffer for 1 hour on ice. The samples were pipetted up and down with pre-cut 1000uL pipette tip to disassociate the tissue further. The dissociated tissues were passed through 70 um cell strainers (Corning) into a 50mL conical tube. The strainers were rinsed with lysis buffer to minimize nuclei loss. The samples were centrifuged to pellet the nuclei at 500g for 5 minutes at 4°C and the supernatant was discarded. The samples resuspended again in 1ml lysis buffer, transferred into new 15mL tubes, pelleted again and the supernatant was discarded. The pellets were resuspended in 50ul of nuclei buffer, and 5 mL of 4% Paraformaldehyde (PFA) (EMS) diluted in RNase free PBS, was added to fix the nuclei for 15 minutes on ice. The tubes were flicked gently every 5 minutes to reduce clumping of nuclei. The fixed nuclei were pelleted at 500g for 3 minutes at 4°C and the PFA waste was discarded. The pelleted nuclei washed in nuclei wash buffer (cell lysis buffer without IGEPAL) and then centrifuged again at 500g for 5 minutes 4°C, and the supernatant was discarded. Finally, the pellets were resuspended again in nuclei wash buffer and then flash-frozen in liquid nitrogen before storing in -80°C.

For nuclei extraction from the differentiation culture, the cells were treated with StemPro Accutase (Thermo, #A1110501) for 7min to detach the cells and transfer them into 15mL tube, then

incubated in trypsin (Thermo, #25300054) for another 7min to prevent re-clumping. The cells were spun down to remove trypsin after inactivation with more media. The pellet was treated with nuclei lysis buffer and the same steps for nuclei extraction protocol were followed.

2.4.3 *Sci-RNA-seq*

Single-cell combinatorial-indexing RNA-sequencing (sci-RNA-seq) protocol is described previously (Cao *et al.*, 2019). sci-RNA-seq relies on the following steps, (i) thawed nuclei were permeabilized with 0.2% TritonX-100 (Sigma, #T9284) (in nuclei wash buffer) for 3 min on ice, and briefly sonicated to reduce nuclei clumping; (ii) nuclei distributed across 96-well plates; (iii) A first molecular index is introduced to the mRNA of cells within each well, with in situ reverse transcription (RT) incorporating the unique molecular identifiers (UMIs); (iv) All cells were pooled and redistributed to multiple 96-well plates in limiting numbers (e.g., 10 to 100 per well) and a second molecular index is introduced by hairpin ligation;(v) Second strand synthesis, fragmentation, purification and indexed PCR; (vi) Library purification and sequencing is performed.

All libraries were sequenced on one NovaSeq platform (Illumina). Base calls, downstream sequence processing and single-cell digital-expression matrix generation steps were similar to what was described in sci-RNA-seq3 paper (Cao *et al.*, 2019). STAR (Dobin *et al.*, 2013) v.2.5.2b54 aligner used with default settings and gene annotations (GRCh38-primary-assembly, gencode.v27). Uniquely mapping reads were extracted, and duplicates were removed using the UMI sequence, reverse transcription index, hairpin ligation adaptor index and read 2 end-

coordinate (that is, reads with identical UMI, reverse transcription index, ligation adaptor index and tagmentation site were considered duplicates).

2.4.4 *Data Analysis*

All low-quality reads were removed from the data (including jaws, toothgerms and salivary glands samples from all time points) by setting UMI cutoff to greater than 200 and removing all mitochondrial reads (QC table: Table 2.4). Following Monocle3 workflow (Cao *et al.*, 2019; Qiu *et al.*, 2017; Trapnell *et al.*, 2014), data underwent normalization by size factor, preprocessing, dimension reduction (UMAP algorithm (McInnes *et al.*, 2018)), and unsupervised graph-based clustering analysis (Leiden Algorithm (Levine *et al.*, 2015; Traag *et al.*, 2019)). Certain clusters from the initial analysis were selected for further sub-clustering, and the previous analysis repeated. Pseudotime analysis also was done with Monocle3 following the default workflow, which include learning the graph, ordering the cells, and plotting the trajectory over UMAP. Mutual nearest neighbors (MNNs) algorithm (Haghverdi *et al.*, 2018) was used for batch effect correction only between day10 differentiation sample and day16 sample. PanglaoDB (Franzén *et al.*, 2019), a curated single-cell gene expression database was utilized to explore the consensus of cell type markers used across publicly available single-cell datasets.

Table 2.4. Sequencing Depth

	Overall QC
Total reads	274558788
Total UMIs	120304751
Duplication rate	56.17%
Cells with >100 UMIs	145258
Cells with >200 UMIs	96072
Mean UMIs per cell	455
Mean genes per cell	373
Percentage of mitochondrial UMIs per cell	1.38%

2.4.5 *Top marker genes*

Each dataset or subset was analyzed with monocle's `top_maker` function to find potential marker genes. All non-protein coding genes, ribosomal and mitochondrial genes were excluded from the input genes, and only the top 100 genes sorted by marker score were included in the results.

2.4.6 *Heatmap and GO-terms enrichment*

ComplexHeatmap package (Gu et al., 2016) was used to generate custom heatmaps that integrate GO-terms per clusters. ViSEAGO package (Brionne et al., 2019) used to generate the GO-terms, and simplifyEnrichment package (Gu and Hübschmann, 2021) used to extract keywords from the top 100 GO-terms (by p value) per cluster. The top 50 marker genes in each cluster were utilized as the input for ViSEAGO. The keywords generated by simplifyEnrichment, were filtered to eliminate redundant and irrelevant words, and only the very top words are displayed on the heatmap.

2.4.7 *Pseudotime analysis*

Pseudotime analysis was done using monocle3 and the density outline of each time point were overlaid on the UMAP graph, to give a better indication of the temporal presence of each cluster.

2.4.8 *Top pathway analysis*

We analyzed the stages of ameloblast development as identified in (Figure 2.12.B). OEE and CL were combined as one OEE cluster to increase the statistical power (Figure 2.19). To analyze those stages in a thorough and reproducible manner, we compiled a comprehensive analysis pipeline that evaluate pathway activity based on ligand receptor interaction and downstream activity. The workflow for our analysis is shown in (Figure 2.18). The first step in the analysis is selecting the appropriate input for each stage of the differentiation to be analyzed. At each stage, we consider the progenitor cells and the target cell type to be differentiated into, as well as all the support cell types that are present in the same stage and that are likely to send the signals. The second step is to analyze all the potential ligand-receptor interactions between the selected cell types, but only focus on in-coming interactions toward the progenitor cells of interest. For this part of the analysis, we used a software, talklr package (Wang, 2020), which uses an information-theoretic approach to identify and rank ligand-receptor interactions with high cell type-specificity. We further filtered talklr output by selecting those ligand-receptor pairs that fall within the major signaling pathway of interest (TGF β , BMP, GDF, GDNF, NODAL, ACTIVIN, WNT, ncWNT, EGF, NRG, FGF, PDGF, VEGF, IGF, INSULIN, HH, EDA, NGF, NT, FLT3, HGF, ROBO, NOTCH, NRXN, OCLN). The third step of the workflow is to obtain the differentially expressed genes (DEGs) between the progenitor cells of interest and their differentiated cell type. This set of genes can be used to evaluate the downstream activity and can be linked to specific ligand-receptor pairs. We

used DEsingle package (Miao *et al.*, 2018) with FDR threshold set to 0.1 to obtain DEGs. The top marker genes for the progenitor cells were also excluded from DEGs in this analysis, to ensure more weight is given to the differentiated cell type. The fourth step is to generate a multilayer network that models the upstream interactions (obtained from step #2) and the downstream interactions that includes transcription factors (TF) and their target genes (DEGs obtained from step #3). We used the R package scMLnet (Cheng *et al.*, 2021) to generate the multilayered network interactions that consists of a top layer for ligands, a layer for receptors, a layer for TFs and a layer for TF-targets. The fifth step is to implement a scoring system to evaluate the connectivity of each part of the multilayered network obtained from previous step, to determine which path is more probably active. We started by assigning fold-change values (obtained in step #3) to target genes at the lowest level. At next level, the TF layer, we assigned the mean values of all the connected TF-targets to each TF. Normalization of the scores to the interaction database depth is done after each step, to ensure the scores remain comparable with each category of interactions. At the receptor layer, we calculated the sum of the values of all the connected TFs to each receptor. At the ligand layer, we calculated the sum of the values of all the connected receptors to each ligand. And finally, all ligands that fall within the same pathway family are aggregated together. The sixth step of our pipeline is to rank pathways based on the percentage of activity compared to the overall combined activity scores of all pathways evaluated in this analysis. The results indicate the most active pathways or the most active ligands that are key drivers of the differentiation at a specific stage of development (Figure 2.19).

2.4.9 *Differential expression*

DEsingle package (Miao *et al.*, 2018) was used to calculate differential expression (DE) between clusters. DEsingle was designed for single-cell RNA sequencing, and it employs Zero-Inflated Negative Binomial model to estimate the proportion of real and dropout zeros. Our cutoff for DE genes were set to include genes with False Discovery Rate (FDR) < 0.1 and more than twofold change.

2.4.10 *Multilayer network analysis*

To generate a multilayer network that models the upstream interactions and the downstream interactions that includes transcription factors (TF) and their target genes, we used the R package scMLnet (Cheng *et al.*, 2021). A custom wrapper code was developed to integrate talklr and DEsingle results with scMLnet.

2.4.11 *Signaling interaction*

In our study, we used talklr package (Wang, 2020) to identify ligand-receptor interaction changes between two adjacent tooth developmental stages. talklr uses an information-theoretic approach to identify ligand-receptor interactions with high cell type-specificity. Ligand-receptor interaction score is defined as $L_i * R_j$, the product of expression levels for the ligand in cell type i and the receptor in cell type j . We normalize interaction scores by dividing $L_i * R_j$ with the sum of interaction scores across all n^2 cell-cell interactions. talklr uses the Kullback-Leibler divergence to quantify how much the observed interaction score distribution differs from the reference distribution. The reference distribution is the equi-probable distribution where every possible

interaction has $1/n^2$ probability, when the aim is to identify cell type-specific ligand-receptor pairs in a single condition. Compared to existing methods such as cellPhoneDB (Efremova et al., 2020) or singleCellSignalR (Cabello-Aguilar et al., 2020) the unique strength of talklr is that it can automatically uncover changes in ligand-receptor re-wiring between two conditions (e.g. different time points, disease vs. normal), where the reference distribution is the observed interaction scores in the baseline condition. The parameters we used were 0.001 for expression threshold, which was determined by calculating the level of expression of the 20th quantile of the aggregated clusters, and $1e-06$ for the pseudo-count value which was determined by the minimum averaged expression value in the set. We considered the interactions among the top 100 ligand-receptor pairs returned by talklr, and we further prioritized them by selecting those that are known to be from physically proximal cell types.

2.4.12 *Datasets projection analysis*

Seurat 4.0 package (Hao *et al.*, 2021) was used to project the invitro differentiation sample into the UMAP space of fetal ameloblasts sample. The dataset in monocle object format that contains the precomputed PCA and UMAP was converted into Seurat object. The projection was done with the default parameters. Graph-based clustering was performed on the projected data by calculating the nearest neighbor cluster center of the fetal sample. Package ‘networkD3’ (Allaire et al., 2017) was used to create the river plot showing the proportions of the classified cells.

Datasets integration analysis

LIGER package (Welch *et al.*, 2019) was used to integrate the fetal dental epithelium lineage dataset with the differentiation datasets to facilitate the cell type label transfer between the sets.

The following integration parameters were used: $k = 25$, $\lambda = 10$, and these settings were determined by utilizing the built-in function that suggest the best values that suit our datasets. For the river plot generation, the minimum fraction of the branching streams was set to 0.25, and the minimum number of cells set to 50. Clusters that have no out- or ingoing connection were eliminated from the graph for clarity.

2.4.13 *RNA Fluorescence in situ Hybridization (FISH) and analysis*

A 12-probe RNAScope HiPlex assay (Advanced Cell Diagnostics, Inc.) including probes against 13 transcripts differentially expressed between cell type clusters in mesenchyme- and epithelial-derived lineages were selected to distinguish cell populations: VWDE, SALL1, FGF4, IGFBP5, FGF10, PRRX1, FBN2, ENAM, PCDH7, SOX5, KRT5, and either DSPP or LGR6. Fresh frozen tissue sections from d80 and d117 were assayed according to the manufacturer's protocol. Briefly, the fresh-frozen tissue sections were fixed using 4% paraformaldehyde in 1X PBS, dehydrated, and treated with the Protease IV kit component. The first four probes were imaged after completing the manufacturer's specified hybridization steps, counterstaining, and coverslipping. Images of tissue sections were obtained using an Nikon Ti2 with an Aura light engine (Lumencor, Beaverton, OR), and BrightLine Sedat filter set optimized for DAPI, FITC, TRITC, Cy5 & Cy7 (Semrock, Rochester, NY: LED-DA/FI/TR/Cy5/Cy7-5X5M-A-000) or a Yokogawa CSU-X1 spinning disk confocal microscope (Yokogawa Corporation, Sugar Land, TX) with a Celesta light engine (Lumencor), ORCA-Fusion scientific CMOS camera (Hamamatsu Corp, Bridgewater, NJ), and a HS-625 high speed emission filter wheel (Finger Lakes Instrumentation, Lima, NY). Coverslips were removed, the first four fluorophores were cleaved, and the process was repeated for probes 5-8 and then probes 9-12. Images were analyzed using Fiji (ImageJ2 v2.3.0) and QuPath (v0.3.0)

quantitative pathology and bioimage analysis freeware (Bankhead et al., 2017). Briefly, The DAPI channel images for imaging rounds two and three were aligned to the DAPI image for imaging round one using the BigDataViewer > BigWarp plugin in Fiji. Matching reference points were identified across the DAPI images and the resultant landmark tables were used in a custom .groovy script to align the FITC, Cy3, Cy5, and Cy7 images from the three rounds of imaging. Images were uniformly background corrected and scaled. Cellular segmentation was performed in QuPath and positive signal foci and clusters were identified as subcellular detections. Parameters were set to allow for detection of foci while avoiding false positive detection events using positive and negative control images. From QuPath, the coordinates and the number of spots estimated (sum of individual puncta and estimated number of transcripts for clustered signal) for each segmented cell were processed using custom R scripts to map cell locations and expression levels. Out of the transcripts assayed by RNAScope, probe set criteria (Table 2.3) used to identify a given cell population in RNAScope data was selected based on differential expression across the cell types identified in the sci-RNA-seq data at corresponding time points (Figure 2.13). Cells matching expression criteria for a cluster's probe set were designated by cluster color and mapped spatially.

2.4.14 *In vitro differentiation*

Briefly, hiPSCs (WTC-11 human induced pluripotent stem cells) (Coriell, #GM25256) were seeded on 12-well plates coated with growth factor-reduced Matrigel (Corning, #356231) and cultured in mTeSR1 stem cell medium (StemCell Technologies, #85850) until cells reach confluency with medium changes daily. On the first day of differentiation (deemed Day 0), stem cell media is replaced with ameloblast base media consisted of either EpiCult-C media (StemCell Technologies, #05630) or RPMI 1640 Medium (Thermo, #11875093) mixed with EpiLife

(Thermo, #MEPI500CA) at 1:1 ratio, supplemented with 0.1x supplement S7 (Thermo, #S0175), 0.1uM β -mercaptoethanol (BME) (Sigma, #M7522) and 400um smoothed agonist (SAG) (Selleckchem, # S7779). At day 3 of differentiation 150pM of bone morphogenic protein-4 (BMP4) (rndsystems, #314-BP-010) is continuously added daily till day 7. At day 8, the base media is supplemented with 1uM of BMP-I inhibitor (LDN-193189) (Tocris, # 6053), 5uM of GSK3-Inhibitor (CHIR99021) (Selleckchem, # 4423), 500pM epidermal growth factor (EGF) (rndsystems, #236-EG) and 3.5 μ M of Neurotrophin-4 (NT4) (rndsystems, #268-N4). The cultures were then harvested at day 10 at an oral epithelium stage, or extended to day 16 by adding 300pM BMP4, and 800nM transforming growth factor beta 1(TGF β 1) (rndsystems, #7754-BH) for the early ameloblast stage at day16. For testing FGFR signaling requirement for the maturation process we added 50nM purified FGFR-mb (see below) to the media at day 14 and harvested the samples at day 16 of the differentiation.

2.4.15 *De novo FGFR-Miniprotein expression*

The gene encoding the designed FGFR-mb protein sequence was synthesized and cloned into modified pET-29b(+) E. coli plasmid expression vectors (GenScript, N-terminal 8-His tag followed by a TEV cleavage site). The sequence of the N-terminal tag is MSHHHHHHHHSENLYFQSGGG, which is followed immediately by the sequence of the designed protein. Plasmids were transformed into chemically competent E. coli Lemo21 cells (NEB). The protein expression was performed using Studier autoinduction medium supplemented with antibiotic, and cultures were grown overnight. Then, IPTG was added to a final concentration of 500 mM and the cells were grown overnight at 22 °C for expression. The cells were collected by spinning at 4,000g for 10 min and then resuspended in lysis buffer (300 mM NaCl, 30 mM Tris-

HCL (pH 8.0), with 0.25% CHAPS for cell assay samples) with DNase and protease inhibitor tablets. The cells were lysed with a sonicator (Qsonica Sonicators) for 4 min in total (2 min each time, 10 s on, 10 s off) with an amplitude of 80%. The soluble fraction was clarified by centrifugation at 20,000g for 30 min. The soluble fraction was purified by immobilized metal affinity chromatography (Qiagen) followed by FPLC SEC (Superdex 75 10/300 GL, GE Healthcare). The protein samples were characterized by SDS-PAGE, and purity was greater than 95%. Protein concentrations were determined by absorbance at 280 nm measured with a NanoDrop spectrophotometer (Thermo Scientific) using predicted extinction coefficients.

2.4.16 *RNA extraction and RT-qPCR analysis*

RNA was extracted using Trizol (Life Technologies) according to manufacturer's instructions. RNA samples were treated with Turbo DNase (Thermo Fisher Scientific) and quantified using Nanodrop ND-1000. Reverse transcription was performed using iScript cDNA Synthesis Kit (Bio-Rad). 10 ng of cDNA was used to perform QRT-PCR using SYBR Green (Applied Biosystems) on a 7300 real time PCR system (Applied Biosystems). The PCR conditions were set up as the following: stage 1 as 50 °C for 2 mins, stage 2 as 95 °C for 10mis, 95 °C for 15 sec, 60 °C for 1 min (40 Cycles). β -actin was used as an endogenous control. The primer sequences used in this work are available in Table 2.5.

Table 2.5. List of QRT-PCR primers

Primer name	Sequence
PITX1_F	TCCACCAAGAGCTTCACCTT
PITX1_R	CGGTGAGGTTGTTGATGTTG
PITX2_3F	GTGTGGACCAACCTTACGGAAG
PITX2_3R	CGAAGCCATTCTTGCATAGCTCG
KRT14_F	CATGAGTGTGGAAGCCGACAT
KRT14_R	GCCTCTCAGGGCATTTCATCTC
bActin_F	TCCCTGGAGAAGAGCTACG
bActin_R	GTAGTTTCGTGGATGCCACA
NEST_F	GAAACAGCCATAGAGGGCAA
NEST_R	TGGTTTTCCAGAGTCTTCAGTGA
OCT4_F	GCTGAAGCTGGAGAAGGAGAAGCTG
OCT4_R	CAAGGGCCGCAGCTTACACATGTTC
P63_F	TTCTTAGCGAGGTTGGGCTG
P63_R	GATCGCATGTGCGAAATTGCTC
TBX1_1F	CGCAGTGGATGAAGCAAATCGTG
TBX1_1R	TTTTCGTGGGTCCACATAGACC
Brachyury_1F	TATGAGCCTCGAATCCACATAGT
Brachyury_1R	CCTCGTTCTGATAAGCAGTCAC
AMBN_2F	TTGAGCCTTGAGACAATGAGAC
AMBN_2R	AGACCGTGCATCCACAAAGAA

2.4.17 Development of Ameloblast Organoid

The day16 differentiated iAM cells were trypsinized using TrypLE (Thermo Scientific) and re-plated in in 24-well ultra-low attachment plate (Corning, #4441) containing an ameloblast base medium with 10 μ M ROCKi (Y-27632, Selleckchem, #S1049). The organoid cultures were maintained at 37°C in 5% CO₂, and the medium was changed every 3-days until further analysis.

Co-culture protocol for ameloblast and odontoblast organoid

The day16 differentiated iAM cells were cultured in ultra-low attachment 12-well plate for a week in ameloblast base medium. The odontogenic organoids were made in a similar manner in a separate plate by culturing DPSCs (isolated from primary molar sample of young patient (Macrin et al., 2019)) in odontogenic differentiation medium containing DMEM (Gibco, #11995073)

ascorbic acid (Sigma, #A8960), β -Glycerophosphate (Sigma, #35675), and dexamethasone (Sigma, #D2915), 10% FBS (Gibco, #10437028) and 1% Penicillin/Streptomycin (Gibco, #15140122). The two types of organoids were co-cultured in the same wells for two weeks, supplemented with a 1:1 mixture of both odontogenic and ameloblasts base media at 37°C in 5% CO₂. The co-culture was sampled later for further analysis.

2.4.18 *Co-culture protocol for monolayer*

The DPSCs were plated as monolayer mixed in 25% (v/v) of Matrigel (Corning, #356231) diluted in odontogenic media in a glass-bottomed 96-well plate (Corning, #3603). The following day, iAM cells suspended in the ameloblast base medium and 10 μ M ROCKi (Y-27632, Selleckchem, #S1049) were added on top of the DPSCs monolayer and then incubated for 24 hours at 37°C in 5% CO₂. The formed organoids were supplemented with fresh media (1:1 mixture ameloblast and odontogenic media) containing Calcein solution (Sigma, #C0875) (1 μ M, 1:1000) on every three consecutive days. The co-culture was sampled on the 14th day for further analysis.

2.4.19 *Cryosectioning and Immunostaining for the organoids*

The organoids were imbedded in OCT compound (Tissue-Tek, # 4583) and slowly frozen on a metal block chilled on dry ice. Frozen organoids were cut using Cryostat (Leica CM1850) to create 10 μ m slices and fixed on glass slides (Fisherbrand, #12-55015) for staining. The organoid sections were fixed in 4% paraformaldehyde (PFA) for 10-15min at RT and later washed thrice with 1X PBS for 5 min each. Slides were then immersed in 0.5% TritonX 100 at RT for 5 minutes to facilitate permeabilization. Later blocking was done for 1 hour at RT in a humidified chamber with

a blocking buffer consisting of 0.1% Triton X-100 and 5% Bovine Serum Albumin (VWR). The organoids were incubated in primary antibodies (Table 2.6) overnight at 4°C in a humidified chamber. After 3x5 minute washes in PBS in a coplin jar, the slides were transferred to a humidified chamber with secondary antibodies. Secondary antibodies and Phalloidin (Table 2.7) were applied for 1 hour at RT in the same blocking agent, followed by rinsing the slides with PBS 3x5min in coplin jar. The slides were incubated in autofluorescence quenching solution (Vector Labs, #SP-8400) for 5 min at RT under dark conditions and rinsed 1x with PBS. DAPI (Thermo Fisher) was applied for 10 minutes at room temperature in PBS. Slides were then rinsed with PBS for 10 minutes in a coplin jar. Slides were then mounted with Vectashield (Vector Labs) and stored at 4°C for imaging.

Table 2.6. List of primary antibodies

Isotype/ Antigen	Company	Identifier	Dilution factor	Host species
AMBN	Santa Cruz	sc-271012; RRID: AB_10613795	1:50	Mouse
AMELX	Santa Cruz	sc-365284; RRID: AB_10843799	1:50	Mouse
DSPP	Santa Cruz	sc-73632; RRID: AB_2230660	1:50	Mouse
ENAM	Thermo Fisher	PA5-25734; RRID: AB_2543234	1:100	Rabbit
VIMENTIN	Cell Signalling	5741S; RRID: AB_10695459	1:200	Rabbit
Human Nuclei	Millipore	MAB1281; RRID:AB_94090	1:100	Rabbit
CD146 (MCAM)	Abcam	ab75769; RRID: AB_2143375	1:200	Mouse
KRT14	Thermo Fisher	LL002; RRID: AB_306091	1:200	Mouse
KRT5	Sigma-Aldrich	HPA059479; RRID:AB_2684034	1:100	Rabbit
ZO-1	Invitrogen	33-9100; RRID: AB_87181	1:100	Mouse
anti-GFP	Invitrogen	A-1112; RRID:AB_221569	1:500	Rabbit
SP6	Atlas Antibodies	HPA024516; RRID: AB_10960551	1:100	Rabbit
CD144	BD Biosciences	555661, RRID: AB_396015	1:200	Mouse
DAPI	Thermo Fisher	D1306, RRID: AB_2629482		

Table 2.7. List of Secondary antibodies

Isotype/ Antigen	Company	Identifier	Dilution factor	Host species
Mouse IgG (Alexa Flour 488)	Thermo Fisher	A11001; RRID: AB 2534069	1:500	Goat
Rabbit IgG (Alexa Flour 488)	Thermo Fisher	A-32731; RRID:AB 2633280	1:500	Goat
Mouse IgG (Alexa Flour 568)	Thermo Fisher	A-11004; RRID:AB 2534072	1:500	Goat
Rabbit IgG (Alexa Flour 568)	Thermo Fisher	A-11036, RRID:AB 10563566	1:500	Goat
Mouse IgG (Alexa Flour 647)	Thermo Fisher	A32728, RRID:AB 2633277	1:500	Goat
Rabbit IgG (Alexa Flour 647)	Thermo Fisher	A32733, RRID:AB 2633282	1:500	Goat

2.4.20 *Wholemout immunostaining analysis*

The organoids were collected in a 2ml tube after two weeks and washed thoroughly with 1x PBS before fixation. The organoids were fixed in 4% paraformaldehyde (PFA) for 10-15min at RT on a rocker. Later the fixed organoids were washed thrice with 1X PBS for 5 min each. The organoids were then immersed in 0.5% TritonX 100 at RT on a rocker for 5 minutes. Later blocking was done for 1hour at RT on a rocker with a blocking buffer consisting of 0.1% Triton X-100 and 5% goat serum (VWR). The organoids were incubated overnight in the primary antibodies (Table 2.6) at 4°C on a rocker. After 5-minute washes in PBS for thrice in a coplin jar, the organoids were incubated with secondary antibodies (Table 2.7) for an hour at RT on a rocker. The primary and the secondary antibodies were prepared in the blocking agent consisting of 0.1% Triton X-100 and 3% goat serum (VWR). Followed by washing the organoids with PBS 3x5min on a rocker. The organoids were incubated in autofluorescence quenching solution (Vector Labs, #SP-8400) for 5 min at RT under dark conditions on a rocker and rinsed 1x with PBS. Incubate the organoids in 200 mL of PBS containing DAPI (Thermo Fisher) for 10 min. The organoids were then rinsed with PBS, mounted with Vectashield (Vector Labs, # H-1700), and stored at 4°C for imaging.

2.4.21 *Injection of iPSC-derived ameloblast-like cells into mouse muscles*

hiPSCs (WTC11) were allowed to undergo differentiation for the pre-ameloblast stage at day16 using the following basal supplements mentioned above cultured in Matrigel. 1×10^6 iAM cells were resuspended in Matrigel supplemented with a cocktail of pro-survival factors (Laflamme et al., 2007) and injected into the femoral muscle of SCID-Beige mice (Charles River, Wilmington, MA). Mice were kept under BioSafety containment Level 2. Mice were sacrificed and femoral muscles were harvested after 2 months and were dissected at the site of injection (left leg muscle) to perform further analysis. Experiment was performed in compliance with ethical regulations, IACUC protocol #4152-01. After dissection, left leg muscles were embedded in embedding cryo-mold (Polysciences, #18986-1) with minimum amount of Tissue-Tek O.C.T. compound (Sakura, catalog number: 4583) to cover the muscle region. The embedded tissue was then snap-frozen by placing on a cold-resistant beaker of 2-methylbutane solution (EMD, #MX0760-1) into a slurry of liquid nitrogen for 5-mins, which allows fast cooling to $-80\text{ }^{\circ}\text{C}$. The snap-frozen samples are then placed in a $-80\text{ }^{\circ}\text{C}$ freezer for storage. The cryostat and blade are both pre-chilled to $-20\text{ }^{\circ}\text{C}$ before cryo-sectioning. $10\text{ }\mu\text{m}$ -thick sections were made on pre-chilled Superfrost Plus microscope slides (Fisherbrand, #12-550-15) and then store in a $-80\text{ }^{\circ}\text{C}$.

2.4.22 *Calcification assays: Von Kossa and Alizarin Red Staining*

Identification of mineralization was performed on tissue sections stained with Von Kossa and Alizarin Red S. Frozen leg muscle sections ($10\mu\text{m}$) were fixed with 4% paraformaldehyde (EMS, #15710) in H₂O at room temperature for 12min. Rinse the section with deionized distilled water thrice for 5min each. Sections were incubated in with 5% silver nitrate solution (SIGMA-ALDRICH #209139) placed under ultraviolet light for 1 hour. The section was rinsed with several

changes of deionized distilled water for 5min each and later incubated in 5% Sodium Thiosulfate solution (SIGMA-ALDRICH #217263) for 5 minute to remove un-reacted silver. Similarly, sections were stained with 2% Alizarin red S solution (pH4.2) (Sigma, #A5533) for 1 hour in the dark. The slides were thoroughly with deionized distilled water for 5min each followed by counterstaining the sections with nuclear fast red stain (EMS, # 26078-05) for 5 minutes. Rinsed in deionized distilled water briefly for 5mins each the slides were successfully transferred into coplin jars to perform dehydration step through graded alcohol and clear the slides in CitriSolv solution (Decon, #1601). Slides were then mounted with Vectashield (Vector Labs, #H-1400-10) and stored at room temperature for imaging.

2.4.23 *Cryosectioning of fetal samples*

Jaw tissues were fixed with 4% PFA overnight at 4°C followed by 30% sucrose (Sigma, #RDD023) treatment until the tissue sank to the bottom of the tube. The tissue is then imbedded in OCT compound (Tissue-Tek, # 4583) and slowly frozen on a metal block chilled on dry ice. Frozen samples were cut using Cryostat (Leica CM1850) to create 10µm slices of tissue and fixed on glass slides (Fiserbrand, #12-55015) for staining.

2.4.24 *Immunofluorescence staining and Confocal Imaging*

Toothgerms embedded in O.C.T. were cryosectioned to 10-micron thick sections. The slides were stored at -80°C after cryosectioning and warmed at room temperature prior to staining. Tissues were fixed in 4% paraformaldehyde (PFA) then immersed in 1X PBS for 3x5 minute washes. Antigen retrieval was performed using 10X Citrate Buffer (Sigma-Aldrich) in a capped coplin jar

microwaved for ~45 seconds followed by 15-minutes incubation in microwave. Slides were then allowed to be washed in PBS at room temperature for 7 minutes. Slides were blocked for 90 minutes at room temperature in a humidified chamber with a blocking buffer consisting of 0.1% Triton X-100 and 5% Bovine Serum Albumin (VWR). All the antibodies used in this study and their concentrations are listed in (Table 2.6 and Table 2.7). The primary antibodies were incubated overnight at 4°C in a humidified chamber. After 3x5 minute washes in PBS in a coplin jar, the slides were transferred to a humidified chamber with secondary antibodies. Secondary antibodies were applied for 75 minutes at room temperature in the same blocking agent. Slides were then rinsed with PBS 4x10 minute washes in a coplin jar. DAPI (Thermo Fisher) was applied for 10 minutes at room temperature in PBS. Slides were then rinsed with PBS for 10 minutes in a coplin jar. Slides were then mounted with Vectashield (Vector Labs) and stored at 4°C for imaging. Confocal Imaging was done on a Leica TCS-SPE Confocal microscope using a 40x objective and Leica Software. Images were processed with Fiji software distribution of ImageJ v2.3.0 (Schindelin et al., 2012; Schindelin et al., 2015). NIS-Elements (RRID:SCR_014329) was used for 3D reconstruction.

2.4.25 *Data availability*

The data generated in this study can be downloaded in raw and processed forms from the NCBI Gene Expression Omnibus under accession number (GSE184749). Upon publication, raw RNAScope data will be made publicly available on dryad.org (Dryad research data repository).

2.4.26 *Code availability*

The custom R codes used to generate some of the results in this paper are available in https://github.com/Ruohola-Baker-lab/Tooth_sciRNAseq.

REFERENCES

- Adams, D. (1976). Keratinization of the oral epithelium. *Annals of the Royal College of Surgeons of England* 58, 351-358.
- Aghajanian, H., Choi, C., Ho, V.C., Gupta, M., Singh, M.K., and Epstein, J.A. (2014). Semaphorin 3d and semaphorin 3e direct endothelial motility through distinct molecular signaling pathways. *The Journal of biological chemistry* 289, 17971-17979. 10.1074/jbc.M113.544833.
- Ahmed, N.E., Murakami, M., Kaneko, S., and Nakashima, M. (2016). The effects of hypoxia on the stemness properties of human dental pulp stem cells (DPSCs). *Scientific reports* 6, 35476. 10.1038/srep35476.
- Ahtiainen, L., Uski, I., Thesleff, I., and Mikkola, M.L. (2016). Early epithelial signaling center governs tooth budding morphogenesis. *The Journal of cell biology* 214, 753-767. 10.1083/jcb.201512074.
- Albelda, S.M., Muller, W.A., Buck, C.A., and Newman, P.J. (1991). Molecular and cellular properties of PECAM-1 (endoCAM/CD31): a novel vascular cell-cell adhesion molecule. *The Journal of cell biology* 114, 1059-1068. 10.1083/jcb.114.5.1059.
- Alexa, A., Rahnenfuhrer, J., and Lengauer, T. (2006). Improved scoring of functional groups from gene expression data by decorrelating GO graph structure. *Bioinformatics (Oxford, England)* 22, 1600-1607. 10.1093/bioinformatics/btl140.
- Allaire, J., Ellis, P., Gandrud, C., Kuo, K., Lewis, B., Owen, J., Russell, K., Rogers, J., Sese, C., and Yetman, C. (2017). Package 'networkD3'. D3 JavaScript Network Graphs from R.
- Almushayt, A., Narayanan, K., Zaki, A.E., and George, A. (2006). Dentin matrix protein 1 induces cytodifferentiation of dental pulp stem cells into odontoblasts. *Gene Ther* 13, 611-620. 10.1038/sj.gt.3302687.
- Alraies, A., Alaidaroos, N.Y., Waddington, R.J., Moseley, R., and Sloan, A.J. (2017). Variation in human dental pulp stem cell ageing profiles reflect contrasting proliferative and regenerative capabilities. *BMC cell biology* 18, 12. 10.1186/s12860-017-0128-x.
- Alt, E.U., Senst, C., Murthy, S.N., Slakey, D.P., Dupin, C.L., Chaffin, A.E., Kadowitz, P.J., and Izadpanah, R. (2012). Aging alters tissue resident mesenchymal stem cell properties. *Stem cell research* 8, 215-225. 10.1016/j.scr.2011.11.002.

- An, Z., Sabalic, M., Bloomquist, R.F., Fowler, T.E., Strelman, T., and Sharpe, P.T. (2018). A quiescent cell population replenishes mesenchymal stem cells to drive accelerated growth in mouse incisors. *Nature Communications* 9, 378. 10.1038/s41467-017-02785-6.
- Anders, S., and Huber, W. (2010). Differential expression analysis for sequence count data. *Genome biology* 11, R106. 10.1186/gb-2010-11-10-r106.
- Aomatsu, E., Takahashi, N., Sawada, S., Okubo, N., Hasegawa, T., Taira, M., Miura, H., Ishisaki, A., and Chosa, N. (2014). Novel SCRG1/BST1 axis regulates self-renewal, migration, and osteogenic differentiation potential in mesenchymal stem cells. *Scientific reports* 4, 3652. 10.1038/srep03652.
- Atari, M., Gil-Recio, C., Fabregat, M., Garcia-Fernandez, D., Barajas, M., Carrasco, M.A., Jung, H.S., Alfaro, F.H., Casals, N., Prosper, F., et al. (2012). Dental pulp of the third molar: a new source of pluripotent-like stem cells. *Journal of cell science* 125, 3343-3356. 10.1242/jcs.096537.
- Aurrekoetxea, M., Irastorza, I., García-Gallastegui, P., Jiménez-Rojo, L., Nakamura, T., Yamada, Y., Ibarretxe, G., and Unda, F.J. (2016). Wnt/ β -Catenin Regulates the Activity of Epiprofin/Sp6, SHH, FGF, and BMP to Coordinate the Stages of Odontogenesis. *Frontiers in cell and developmental biology* 4, 25. 10.3389/fcell.2016.00025.
- Balic, A. (2019). Concise Review: Cellular and Molecular Mechanisms Regulation of Tooth Initiation. *Stem cells (Dayton, Ohio)* 37, 26-32. 10.1002/stem.2917.
- Balic, A., and Thesleff, I. (2015). Tissue Interactions Regulating Tooth Development and Renewal. *Current topics in developmental biology* 115, 157-186. 10.1016/bs.ctdb.2015.07.006.
- Bankhead, P., Loughrey, M.B., Fernández, J.A., Dombrowski, Y., McArt, D.G., Dunne, P.D., McQuaid, S., Gray, R.T., Murray, L.J., Coleman, H.G., et al. (2017). QuPath: Open source software for digital pathology image analysis. *Scientific reports* 7, 16878. 10.1038/s41598-017-17204-5.
- Barzilai, N., Huffman, D.M., Muzumdar, R.H., and Bartke, A. (2012). The critical role of metabolic pathways in aging. *Diabetes* 61, 1315-1322. 10.2337/db11-1300.
- Beyaz, S., Mana, M.D., Roper, J., Kedrin, D., Saadatpour, A., Hong, S.J., Bauer-Rowe, K.E., Xifaras, M.E., Akkad, A., Arias, E., et al. (2016). High-fat diet enhances stemness and tumorigenicity of intestinal progenitors. *Nature* 531, 53-58. 10.1038/nature17173.
- Bianchi-Smiraglia, A., Kunnev, D., Limoge, M., Lee, A., Beckerle, M.C., and Bakin, A.V. (2013). Integrin-beta5 and zyxin mediate formation of ventral stress fibers in response to transforming growth factor beta. *Cell cycle (Georgetown, Tex.)* 12, 3377-3389. 10.4161/cc.26388.

- Böheim, K., Denz, H., Böheim, C., Glassl, H., and Huber, H. (1987). An immunohistologic study of the distribution and status of activation of head and neck tumor infiltrating leukocytes. *Archives of oto-rhino-laryngology* *244*, 127-132. 10.1007/bf00458563.
- Bonab, M.M., Alimoghaddam, K., Talebian, F., Ghaffari, S.H., Ghavamzadeh, A., and Nikbin, B. (2006). Aging of mesenchymal stem cell in vitro. *BMC cell biology* *7*, 14. 10.1186/1471-2121-7-14.
- Brionne, A., Juanchich, A., and Hennequet-Antier, C. (2019). ViSEAGO: a Bioconductor package for clustering biological functions using Gene Ontology and semantic similarity. *BioData mining* *12*, 16. 10.1186/s13040-019-0204-1.
- Buck, M.D., O'Sullivan, D., Klein Geltink, R.I., Curtis, J.D., Chang, C.H., Sanin, D.E., Qiu, J., Kretz, O., Braas, D., van der Windt, G.J., et al. (2016). Mitochondrial Dynamics Controls T Cell Fate through Metabolic Programming. *Cell* *166*, 63-76. 10.1016/j.cell.2016.05.035.
- Cabello-Aguilar, S., Alame, M., Kon-Sun-Tack, F., Fau, C., Lacroix, M., and Colinge, J. (2020). SingleCellSignalR: inference of intercellular networks from single-cell transcriptomics. *Nucleic Acids Research* *48*, e55. 10.1093/nar/gkaa183.
- Camilleri, E.T., Gustafson, M.P., Dudakovic, A., Riester, S.M., Garces, C.G., Paradise, C.R., Takai, H., Karperien, M., Cool, S., Sampen, H.J., et al. (2016). Identification and validation of multiple cell surface markers of clinical-grade adipose-derived mesenchymal stromal cells as novel release criteria for good manufacturing practice-compliant production. *Stem cell research & therapy* *7*, 107. 10.1186/s13287-016-0370-8.
- Cao, J., Spielmann, M., Qiu, X., Huang, X., Ibrahim, D.M., Hill, A.J., Zhang, F., Mundlos, S., Christiansen, L., Steemers, F.J., et al. (2019). The single-cell transcriptional landscape of mammalian organogenesis. *Nature* *566*, 496-502. 10.1038/s41586-019-0969-x.
- Cao, L., Coventry, B., Goresnik, I., Huang, B., Sheffler, W., Park, J.S., Jude, K.M., Marković, I., Kadam, R.U., Verschueren, K.H.G., et al. (2022). Design of protein-binding proteins from the target structure alone. *Nature* *605*, 551-560. 10.1038/s41586-022-04654-9.
- Chan, Y.S., Goke, J., Ng, J.H., Lu, X., Gonzales, K.A., Tan, C.P., Tng, W.Q., Hong, Z.Z., Lim, Y.S., and Ng, H.H. (2013). Induction of a human pluripotent state with distinct regulatory circuitry that resembles preimplantation epiblast. *Cell stem cell* *13*, 663-675. 10.1016/j.stem.2013.11.015.
- Chang, J.Y., Wang, C., Jin, C., Yang, C., Huang, Y., Liu, J., McKeehan, W.L., D'Souza, R.N., and Wang, F. (2013). Self-renewal and multilineage differentiation of mouse dental epithelial stem cells. *Stem cell research* *11*, 990-1002. 10.1016/j.scr.2013.06.008.
- Chang, T.H., Huang, H.D., Ong, W.K., Fu, Y.J., Lee, O.K., Chien, S., and Ho, J.H. (2014). The effects of actin cytoskeleton perturbation on keratin intermediate filament formation in mesenchymal stem/stromal cells. *Biomaterials* *35*, 3934-3944. 10.1016/j.biomaterials.2014.01.028.

- Cheng, J., Zhang, J., Wu, Z., and Sun, X. (2021). Inferring microenvironmental regulation of gene expression from single-cell RNA sequencing data using scMLnet with an application to COVID-19. *Briefings in bioinformatics* 22, 988-1005. 10.1093/bib/bbaa327.
- Cherepkova, M.Y., Sineva, G.S., and Pospelov, V.A. (2016). Leukemia inhibitory factor (LIF) withdrawal activates mTOR signaling pathway in mouse embryonic stem cells through the MEK/ERK/TSC2 pathway. *Cell death & disease* 7, e2050. 10.1038/cddis.2015.387.
- Chiba, Y., Saito, K., Martin, D., Boger, E.T., Rhodes, C., Yoshizaki, K., Nakamura, T., Yamada, A., Morell, R.J., Yamada, Y., and Fukumoto, S. (2020). Single-Cell RNA-Sequencing From Mouse Incisor Reveals Dental Epithelial Cell-Type Specific Genes. *Frontiers in cell and developmental biology* 8, 841. 10.3389/fcell.2020.00841.
- Cho, K.A., Ryu, S.J., Oh, Y.S., Park, J.H., Lee, J.W., Kim, H.P., Kim, K.T., Jang, I.S., and Park, S.C. (2004). Morphological adjustment of senescent cells by modulating caveolin-1 status. *The Journal of biological chemistry* 279, 42270-42278. 10.1074/jbc.M402352200.
- Cho, S.Y., Seo, D.G., Lee, S.J., Lee, J., Lee, S.J., and Jung, I.Y. (2013). Prognostic factors for clinical outcomes according to time after direct pulp capping. *Journal of endodontics* 39, 327-331. 10.1016/j.joen.2012.11.034.
- Choi, H.J., Park, M.J., Kim, B.S., Choi, H.J., Joo, B., Lee, K.S., Choi, J.H., Chung, T.W., and Ha, K.T. (2017). Transforming growth factor beta1 enhances adhesion of endometrial cells to mesothelium by regulating integrin expression. *BMB reports* 50, 429-434.
- Cliff, T.S., Wu, T., Boward, B.R., Yin, A., Yin, H., Glushka, J.N., Prestegard, J.H., and Dalton, S. (2017). MYC Controls Human Pluripotent Stem Cell Fate Decisions through Regulation of Metabolic Flux. *Cell stem cell* 21, 502-516.e509. 10.1016/j.stem.2017.08.018.
- Cortazar, A.R., Oguiza, J.A., Aransay, A.M., and Lavin, J.L. (2017). VerSeDa: vertebrate secretome database. *Database : the journal of biological databases and curation* 2017. 10.1093/database/baw171.
- de Paula, F., Teshima, T.H.N., Hsieh, R., Souza, M.M., Nico, M.M.S., and Lourenco, S.V. (2017). Overview of Human Salivary Glands: Highlights of Morphology and Developing Processes. *Anatomical record (Hoboken, N.J. : 2007)* 300, 1180-1188. 10.1002/ar.23569.
- Degnim, A.C., Visscher, D.W., Hoskin, T.L., Frost, M.H., Vierkant, R.A., Vachon, C.M., Shane Pankratz, V., Radisky, D.C., and Hartmann, L.C. (2012). Histologic findings in normal breast tissues: comparison to reduction mammoplasty and benign breast disease tissues. *Breast cancer research and treatment* 133, 169-177. 10.1007/s10549-011-1746-1.
- Desai, V.D., Hsia, H.C., and Schwarzbauer, J.E. (2014). Reversible modulation of myofibroblast differentiation in adipose-derived mesenchymal stem cells. *PloS one* 9, e86865. 10.1371/journal.pone.0086865.

- Desmouliere, A., Geinoz, A., Gabbiani, F., and Gabbiani, G. (1993). Transforming growth factor-beta 1 induces alpha-smooth muscle actin expression in granulation tissue myofibroblasts and in quiescent and growing cultured fibroblasts. *The Journal of cell biology* *122*, 103-111.
- Dimri, G.P., Lee X Fau - Basile, G., Basile G Fau - Acosta, M., Acosta M Fau - Scott, G., Scott G Fau - Roskelley, C., Roskelley C Fau - Medrano, E.E., Medrano Ee Fau - Linskens, M., Linskens M Fau - Rubelj, I., Rubelj I Fau - Pereira-Smith, O., Pereira-Smith, O., and et al. (1995). A biomarker that identifies senescent human cells in culture and in aging skin in vivo.
- Dobin, A., Davis, C.A., Schlesinger, F., Drenkow, J., Zaleski, C., Jha, S., Batut, P., Chaisson, M., and Gingeras, T.R. (2013). STAR: ultrafast universal RNA-seq aligner. *Bioinformatics (Oxford, England)* *29*, 15-21. 10.1093/bioinformatics/bts635.
- Dong, F., Patnaik, S., Duan, Z.H., Kiedrowski, M., Penn, M.S., and Mayorga, M.E. (2017). A Novel Role for CAMKK1 in the Regulation of the Mesenchymal Stem Cell Secretome. *Stem cells translational medicine* *6*, 1759-1766. 10.1002/sctm.17-0046.
- Edlund, S., Landstrom, M., Heldin, C.H., and Aspenstrom, P. (2002). Transforming growth factor-beta-induced mobilization of actin cytoskeleton requires signaling by small GTPases Cdc42 and RhoA. *Molecular biology of the cell* *13*, 902-914. 10.1091/mbc.01-08-0398.
- Efremova, M., Vento-Tormo, M., Teichmann, S.A., and Vento-Tormo, R. (2020). CellPhoneDB: inferring cell-cell communication from combined expression of multi-subunit ligand-receptor complexes. *Nature protocols* *15*, 1484-1506. 10.1038/s41596-020-0292-x.
- El Agha, E., Kramann, R., Schneider, R.K., Li, X., Seeger, W., Humphreys, B.D., and Bellusci, S. (2017). Mesenchymal Stem Cells in Fibrotic Disease. *Cell stem cell* *21*, 166-177. 10.1016/j.stem.2017.07.011.
- Endoh, M., Kobayashi, Y., Yamakami, Y., Yonekura, R., Fujii, M., and Ayusawa, D. (2009). Coordinate expression of the human pregnancy-specific glycoprotein gene family during induced and replicative senescence. *Biogerontology* *10*, 213-221. 10.1007/s10522-008-9173-3.
- Engin, A.B., Tsatsakis, A.M., Tsoukalas, D., and Engin, A. (2017). Do flavanols-rich natural products relieve obesity-related insulin resistance? *Food and chemical toxicology : an international journal published for the British Industrial Biological Research Association* *112*, 157-167. 10.1016/j.fct.2017.12.055.
- Fang, Z.F., Jin, F., Gai, H., Chen, Y., Wu, L., Liu, A.L., Chen, B., and Sheng, H.Z. (2005). Human embryonic stem cell lines derived from the Chinese population. *Cell research* *15*, 394-400. 10.1038/sj.cr.7290307.
- Filion, L.G., Izaguirre, C.A., Garber, G.E., Huebsh, L., and Aye, M.T. (1990). Detection of surface and cytoplasmic CD4 on blood monocytes from normal and HIV-1 infected

- individuals. *Journal of immunological methods* 135, 59-69. 10.1016/0022-1759(90)90256-u.
- Franzén, O., Gan, L.M., and Björkegren, J.L.M. (2019). PanglaoDB: a web server for exploration of mouse and human single-cell RNA sequencing data. *Database : the journal of biological databases and curation* 2019. 10.1093/database/baz046.
- Fresia, R., Marangoni, P., Burstyn-Cohen, T., and Sharir, A. (2021). From Bite to Byte: Dental Structures Resolved at a Single-Cell Resolution. *Journal of dental research* 100, 897-905. 10.1177/00220345211001848.
- Fugolin, A.P.P., and Pfeifer, C.S. (2017). New Resins for Dental Composites. *Journal of dental research* 96, 1085-1091. 10.1177/0022034517720658.
- Fujikura, J., Yamato, E., Yonemura, S., Hosoda, K., Masui, S., Nakao, K., Miyazaki Ji, J., and Niwa, H. (2002). Differentiation of embryonic stem cells is induced by GATA factors. *Genes & development* 16, 784-789. 10.1101/gad.968802.
- Fujita, T., Shiba, H., Sakata, M., Uchida, Y., Ogawa, T., and Kurihara, H. (2002). Effects of transforming growth factor-beta 1 and fibronectin on SPARC expression in cultures of human periodontal ligament cells. *Cell biology international* 26, 1065-1072.
- Gafni, O., Weinberger, L., Mansour, A.A., Manor, Y.S., Chomsky, E., Ben-Yosef, D., Kalma, Y., Viukov, S., Maza, I., Zviran, A., et al. (2013). Derivation of novel human ground state naive pluripotent stem cells. *Nature* 504, 282-286. 10.1038/nature12745.
- Gascon, S., Murenu, E., Masserdotti, G., Ortega, F., Russo, G.L., Petrik, D., Deshpande, A., Heinrich, C., Karow, M., Robertson, S.P., et al. (2016). Identification and Successful Negotiation of a Metabolic Checkpoint in Direct Neuronal Reprogramming. *Cell stem cell* 18, 396-409. 10.1016/j.stem.2015.12.003.
- Gharibi, B., Ghuman, M., and Hughes, F.J. (2016). DDIT4 regulates mesenchymal stem cell fate by mediating between HIF1alpha and mTOR signalling. *Scientific reports* 6, 36889. 10.1038/srep36889.
- Ghazanfari, R., Zacharaki, D., Li, H., Ching Lim, H., Soneji, S., and Scheduling, S. (2017). Human Primary Bone Marrow Mesenchymal Stromal Cells and Their in vitro Progenies Display Distinct Transcriptional Profile Signatures. *Scientific reports* 7, 10338. 10.1038/s41598-017-09449-x.
- Goto, N., Fujimoto, K., Fujii, S., Ida-Yonemochi, H., Ohshima, H., Kawamoto, T., Noshiro, M., Shukunami, C., Kozai, K., and Kato, Y. (2016). Role of MSX1 in Osteogenic Differentiation of Human Dental Pulp Stem Cells. *Stem cells international* 2016, 8035759. 10.1155/2016/8035759.
- Govindasamy, V., Ronald, V.S., Abdullah, A.N., Nathan, K.R., Ab Aziz, Z.A., Abdullah, M., Musa, S., Kasim, N.H., and Bhonde, R.R. (2011). Differentiation of dental pulp stem

- cells into islet-like aggregates. *Journal of dental research* *90*, 646-652. 10.1177/0022034510396879.
- Graneli, C., Thorfve, A., Ruetschi, U., Brisby, H., Thomsen, P., Lindahl, A., and Karlsson, C. (2014). Novel markers of osteogenic and adipogenic differentiation of human bone marrow stromal cells identified using a quantitative proteomics approach. *Stem cell research* *12*, 153-165. 10.1016/j.scr.2013.09.009.
- Gronthos, S., Arthur, A., Bartold, P.M., and Shi, S. (2011). A method to isolate and culture expand human dental pulp stem cells. *Methods in molecular biology (Clifton, N.J.)* *698*, 107-121. 10.1007/978-1-60761-999-4_9.
- Gronthos, S., Mankani, M., Brahim, J., Robey, P.G., and Shi, S. (2000). Postnatal human dental pulp stem cells (DPSCs) in vitro and in vivo. *Proceedings of the National Academy of Sciences of the United States of America* *97*, 13625-13630. 10.1073/pnas.240309797.
- Grow, E.J., Flynn, R.A., Chavez, S.L., Bayless, N.L., Wossidlo, M., Wesche, D.J., Martin, L., Ware, C.B., Blish, C.A., Chang, H.Y., et al. (2015). Intrinsic retroviral reactivation in human preimplantation embryos and pluripotent cells. *Nature* *522*, 221-225. 10.1038/nature14308.
- Gu, Z., Eils, R., and Schlesner, M. (2016). Complex heatmaps reveal patterns and correlations in multidimensional genomic data. *Bioinformatics (Oxford, England)* *32*, 2847-2849. 10.1093/bioinformatics/btw313.
- Gu, Z., and Hübschmann, D. (2021). *simplifyEnrichment*: an R/Bioconductor package for Clustering and Visualizing Functional Enrichment Results. *bioRxiv*, 2020.2010.2027.312116. 10.1101/2020.10.27.312116.
- Guo, D., Huang, J., and Gong, J. (2012). Bone morphogenetic protein 4 (BMP4) is required for migration and invasion of breast cancer. *Molecular and cellular biochemistry* *363*, 179-190. 10.1007/s11010-011-1170-1.
- Haghverdi, L., Lun, A.T.L., Morgan, M.D., and Marioni, J.C. (2018). Batch effects in single-cell RNA-sequencing data are corrected by matching mutual nearest neighbors. *Nature biotechnology* *36*, 421-427. 10.1038/nbt.4091.
- Haleem-Smith, H., Calderon, R., Song, Y., Tuan, R.S., and Chen, F.H. (2012). Cartilage oligomeric matrix protein enhances matrix assembly during chondrogenesis of human mesenchymal stem cells. *Journal of cellular biochemistry* *113*, 1245-1252. 10.1002/jcb.23455.
- Hamilton, L.K., Dufresne, M., Joppe, S.E., Petryszyn, S., Aumont, A., Calon, F., Barnabe-Heider, F., Furtos, A., Parent, M., Chaurand, P., and Fernandes, K.J. (2015). Aberrant Lipid Metabolism in the Forebrain Niche Suppresses Adult Neural Stem Cell Proliferation in an Animal Model of Alzheimer's Disease. *Cell stem cell* *17*, 397-411. 10.1016/j.stem.2015.08.001.

- Hanzelmann, S., Beier, F., Gusmao, E.G., Koch, C.M., Hummel, S., Charapitsa, I., Jousen, S., Benes, V., Brummendorf, T.H., Reid, G., et al. (2015). Replicative senescence is associated with nuclear reorganization and with DNA methylation at specific transcription factor binding sites. *Clinical epigenetics* 7, 19. 10.1186/s13148-015-0057-5.
- Hao, Y., Hao, S., Andersen-Nissen, E., Mauck, W.M., 3rd, Zheng, S., Butler, A., Lee, M.J., Wilk, A.J., Darby, C., Zager, M., et al. (2021). Integrated analysis of multimodal single-cell data. *Cell* 184, 3573-3587.e3529. 10.1016/j.cell.2021.04.048.
- Harada, H., Ichimori, Y., Yokohama-Tamaki, T., Ohshima, H., Kawano, S., Katsube, K., and Wakisaka, S. (2006). Stratum intermedium lineage diverges from ameloblast lineage via Notch signaling. *Biochemical and biophysical research communications* 340, 611-616. 10.1016/j.bbrc.2005.12.053.
- Harada, H., Mitsuyasu, T., Toyono, T., and Toyoshima, K. (2002). Epithelial stem cells in teeth. *Odontology* 90, 1-6. 10.1007/s102660200000.
- Haro, E., Delgado, I., Junco, M., Yamada, Y., Mansouri, A., Oberg, K.C., and Ros, M.A. (2014). Sp6 and Sp8 transcription factors control AER formation and dorsal-ventral patterning in limb development. *PLoS genetics* 10, e1004468. 10.1371/journal.pgen.1004468.
- Hofsteen, P., Robitaille, A.M., Chapman, D.P., Moon, R.T., and Murry, C.E. (2016). Quantitative proteomics identify DAB2 as a cardiac developmental regulator that inhibits WNT/beta-catenin signaling. *Proceedings of the National Academy of Sciences of the United States of America* 113, 1002-1007. 10.1073/pnas.1523930113.
- Hosoya, A., and Nakamura, H. (2015). Ability of stem and progenitor cells in the dental pulp to form hard tissue. *Japanese Dental Science Review* 51, 75-83. 10.1016/j.jdsr.2015.03.002.
- Hovorakova, M., Lesot, H., Peterka, M., and Peterkova, R. (2018). Early development of the human dentition revisited. *Journal of anatomy* 233, 135-145. 10.1111/joa.12825.
- Huang da, W., Sherman, B.T., and Lempicki, R.A. (2009a). Bioinformatics enrichment tools: paths toward the comprehensive functional analysis of large gene lists. *Nucleic Acids Research* 37, 1-13. 10.1093/nar/gkn923.
- Huang da, W., Sherman, B.T., and Lempicki, R.A. (2009b). Systematic and integrative analysis of large gene lists using DAVID bioinformatics resources. *Nature protocols* 4, 44-57. 10.1038/nprot.2008.211.
- Hung, R.J., and Terman, J.R. (2011). Extracellular inhibitors, repellents, and semaphorin/plexin/MICAL-mediated actin filament disassembly. *Cytoskeleton (Hoboken, N.J.)* 68, 415-433. 10.1002/cm.20527.
- Ibarretxe, G., Aurrekoetxea, M., Crende, O., Badiola, I., Jimenez-Rojo, L., Nakamura, T., Yamada, Y., and Unda, F. (2012). Epiprofin/Sp6 regulates Wnt-BMP signaling and the establishment of cellular junctions during the bell stage of tooth development. *Cell and tissue research* 350, 95-107. 10.1007/s00441-012-1459-8.

- Ignotz, R.A., and Massague, J. (1986). Transforming growth factor-beta stimulates the expression of fibronectin and collagen and their incorporation into the extracellular matrix. *The Journal of biological chemistry* 261, 4337-4345.
- Isobe, Y., Koyama, N., Nakao, K., Osawa, K., Ikeno, M., Yamanaka, S., Okubo, Y., Fujimura, K., and Bessho, K. (2016). Comparison of human mesenchymal stem cells derived from bone marrow, synovial fluid, adult dental pulp, and exfoliated deciduous tooth pulp. *International journal of oral and maxillofacial surgery* 45, 124-131. 10.1016/j.ijom.2015.06.022.
- Jang, J.H., Lee, H.W., Cho, K.M., Shin, H.W., Kang, M.K., Park, S.H., and Kim, E. (2016). In vitro characterization of human dental pulp stem cells isolated by three different methods. *Restorative dentistry & endodontics* 41, 283-295. 10.5395/rde.2016.41.4.283.
- Jernvall, J., and Thesleff, I. (2012). Tooth shape formation and tooth renewal: evolving with the same signals. *Development (Cambridge, England)* 139, 3487-3497. 10.1242/dev.085084.
- Jiang, L., Lin, L., Li, R., Yuan, C., Xu, M., Huang, J.H., and Huang, M. (2016). Dimer conformation of soluble PECAM-1, an endothelial marker. *The international journal of biochemistry & cell biology* 77, 102-108. 10.1016/j.biocel.2016.06.001.
- Jussila, M., and Thesleff, I. (2012). Signaling networks regulating tooth organogenesis and regeneration, and the specification of dental mesenchymal and epithelial cell lineages. *Cold Spring Harbor perspectives in biology* 4, a008425. 10.1101/cshperspect.a008425.
- Kanehisa, M., Furumichi, M., Tanabe, M., Sato, Y., and Morishima, K. (2017). KEGG: new perspectives on genomes, pathways, diseases and drugs. *Nucleic Acids Research* 45, D353-d361. 10.1093/nar/gkw1092.
- Karamzadeh, R., Eslaminejad, M.B., and Aflatoonian, R. (2012). Isolation, characterization and comparative differentiation of human dental pulp stem cells derived from permanent teeth by using two different methods. *Journal of visualized experiments : JoVE*. 10.3791/4372.
- Kardos, T.B., and Hubbard, M.J. (1981). Rapid dissection of rodent molar-tooth germs. *Laboratory animals* 15, 371-373. 10.1258/002367781780952870.
- Knobloch, M., Braun, S.M., Zurkirchen, L., von Schoultz, C., Zamboni, N., Arauzo-Bravo, M.J., Kovacs, W.J., Karalay, O., Suter, U., Machado, R.A., et al. (2013). Metabolic control of adult neural stem cell activity by Fasn-dependent lipogenesis. *Nature* 493, 226-230. 10.1038/nature11689.
- Kolar, M.K., Itte, V.N., Kingham, P.J., Novikov, L.N., Wiberg, M., and Kelk, P. (2017). The neurotrophic effects of different human dental mesenchymal stem cells. *Scientific reports* 7, 12605. 10.1038/s41598-017-12969-1.
- Koyama, E., Wu, C., Shimo, T., Iwamoto, M., Ohmori, T., Kurisu, K., Ookura, T., Bashir, M.M., Abrams, W.R., Tucker, T., and Pacifici, M. (2001). Development of stratum intermedium

and its role as a Sonic hedgehog-signaling structure during odontogenesis. *Developmental dynamics* : an official publication of the American Association of Anatomists *222*, 178-191. 10.1002/dvdy.1186.

- Krivanek, J., Soldatov, R.A., Kastriti, M.E., Chontorotzea, T., Herdina, A.N., Petersen, J., Szarowska, B., Landova, M., Matejova, V.K., Holla, L.I., et al. (2020). Dental cell type atlas reveals stem and differentiated cell types in mouse and human teeth. *Nat Commun* *11*, 4816. 10.1038/s41467-020-18512-7.
- Kruger, R.P., Aurandt, J., and Guan, K.L. (2005). Semaphorins command cells to move. *Nature reviews. Molecular cell biology* *6*, 789-800. 10.1038/nrm1740.
- Kurpinski, K., Lam, H., Chu, J., Wang, A., Kim, A., Tsay, E., Agrawal, S., Schaffer, D.V., and Li, S. (2010). Transforming growth factor-beta and notch signaling mediate stem cell differentiation into smooth muscle cells. *Stem cells (Dayton, Ohio)* *28*, 734-742. 10.1002/stem.319.
- La Noce, M., Paino, F., Spina, A., Naddeo, P., Montella, R., Desiderio, V., De Rosa, A., Papaccio, G., Tirino, V., and Laino, L. (2014). Dental pulp stem cells: state of the art and suggestions for a true translation of research into therapy. *Journal of dentistry* *42*, 761-768. 10.1016/j.jdent.2014.02.018.
- Laflamme, M.A., Chen, K.Y., Naumova, A.V., Muskheli, V., Fugate, J.A., Dupras, S.K., Reinecke, H., Xu, C., Hassanipour, M., Police, S., et al. (2007). Cardiomyocytes derived from human embryonic stem cells in pro-survival factors enhance function of infarcted rat hearts. *Nature biotechnology* *25*, 1015-1024. 10.1038/nbt1327.
- Lampugnani, M.G., Resnati, M., Raiteri, M., Pigott, R., Pisacane, A., Houen, G., Ruco, L.P., and Dejana, E. (1992). A novel endothelial-specific membrane protein is a marker of cell-cell contacts. *The Journal of cell biology* *118*, 1511-1522. 10.1083/jcb.118.6.1511.
- Laurenti, E., and Gottgens, B. (2018). From haematopoietic stem cells to complex differentiation landscapes. *Nature* *553*, 418-426. 10.1038/nature25022.
- Lee, J.W., Kim, Y.H., Kim, S.H., Han, S.H., and Hahn, S.B. (2004). Chondrogenic differentiation of mesenchymal stem cells and its clinical applications. *Yonsei medical journal* *45 Suppl*, 41-47. 10.3349/ymj.2004.45.Suppl.41.
- Levine, J.H., Simonds, E.F., Bendall, S.C., Davis, K.L., Amir el, A.D., Tadmor, M.D., Litvin, O., Fienberg, H.G., Jager, A., Zunder, E.R., et al. (2015). Data-Driven Phenotypic Dissection of AML Reveals Progenitor-like Cells that Correlate with Prognosis. *Cell* *162*, 184-197. 10.1016/j.cell.2015.05.047.
- Li, X., Law, J.W., and Lee, A.Y. (2012). Semaphorin 5A and plexin-B3 regulate human glioma cell motility and morphology through Rac1 and the actin cytoskeleton. *Oncogene* *31*, 595-610. 10.1038/onc.2011.256.

- Liang, J., Zhao, H., Hu, J., Liu, Y., and Li, Z. (2018). SPOCD1 promotes cell proliferation and inhibits cell apoptosis in human osteosarcoma. *Molecular medicine reports* 17, 3218-3225. 10.3892/mmr.2017.8263.
- Liao, Y., Smyth, G.K., and Shi, W. (2014). featureCounts: an efficient general purpose program for assigning sequence reads to genomic features. *Bioinformatics (Oxford, England)* 30, 923-930. 10.1093/bioinformatics/btt656.
- Lipski, M., Nowicka, A., Kot, K., Postek-Stefanska, L., Wysoczanska-Jankowicz, I., Borkowski, L., Andersz, P., Jarzabek, A., Grocholewicz, K., Sobolewska, E., et al. (2018). Factors affecting the outcomes of direct pulp capping using Biodentine. *Clinical oral investigations* 22, 2021-2029. 10.1007/s00784-017-2296-7.
- Liu, H., Yan, X., Pandya, M., Luan, X., and Diekwisch, T.G. (2016). Daughters of the Enamel Organ: Development, Fate, and Function of the Stratum Intermedium, Stellate Reticulum, and Outer Enamel Epithelium. *Stem cells and development* 25, 1580-1590. 10.1089/scd.2016.0267.
- Liu, J., Saiyin, W., Xie, X., Mao, L., and Li, L. (2020). Ablation of Fam20c causes amelogenesis imperfecta via inhibiting Smad dependent BMP signaling pathway. *Biology direct* 15, 16. 10.1186/s13062-020-00270-7.
- Lv, F.J., Tuan, R.S., Cheung, K.M., and Leung, V.Y. (2014). Concise review: the surface markers and identity of human mesenchymal stem cells. *Stem cells (Dayton, Ohio)* 32, 1408-1419. 10.1002/stem.1681.
- Maas, R., and Bei, M. (1997). The genetic control of early tooth development. *Critical reviews in oral biology and medicine : an official publication of the American Association of Oral Biologists* 8, 4-39. 10.1177/10454411970080010101.
- Macrin, D., Alghadeer, A., Zhao, Y.T., Miklas, J.W., Hussein, A.M., Detraux, D., Robitaille, A.M., Madan, A., Moon, R.T., Wang, Y., et al. (2019). Metabolism as an early predictor of DPSCs aging. *Scientific reports* 9, 2195. 10.1038/s41598-018-37489-4.
- Malik, Z., Alexiou, M., Hallgrimsson, B., Economides, A.N., Luder, H.U., and Graf, D. (2018). Bone Morphogenetic Protein 2 Coordinates Early Tooth Mineralization. *Journal of dental research* 97, 835-843. 10.1177/0022034518758044.
- Manokawinchoke, J., Nattasit, P., Thongngam, T., Pavasant, P., Tompkins, K.A., Egusa, H., and Osathanon, T. (2017). Indirect immobilized Jagged1 suppresses cell cycle progression and induces odonto/osteogenic differentiation in human dental pulp cells. *Scientific reports* 7, 10124. 10.1038/s41598-017-10638-x.
- Marangoni, P., Charles, C., Ahn, Y., Seidel, K., Jheon, A., Ganss, B., Krumlauf, R., Viriot, L., and Klein, O.D. (2019). Downregulation of FGF Signaling by Spry4 Overexpression Leads to Shape Impairment, Enamel Irregularities, and Delayed Signaling Center Formation in the Mouse Molar. *JBMR plus* 3, e10205. 10.1002/jbm4.10205.

- Marques, M.S., Wesselink, P.R., and Shemesh, H. (2015). Outcome of Direct Pulp Capping with Mineral Trioxide Aggregate: A Prospective Study. *Journal of endodontics* *41*, 1026-1031. 10.1016/j.joen.2015.02.024.
- Mathieu, J., and Ruohola-Baker, H. (2017). Metabolic remodeling during the loss and acquisition of pluripotency. *Development (Cambridge, England)* *144*, 541-551. 10.1242/dev.128389.
- Mathieu, J., Zhang, Z., Zhou, W., Wang, A.J., Heddleston, J.M., Pinna, C.M., Hubaud, A., Stadler, B., Choi, M., Bar, M., et al. (2011). HIF induces human embryonic stem cell markers in cancer cells. *Cancer research* *71*, 4640-4652. 10.1158/0008-5472.Can-10-3320.
- Matthews, B.G., Roguljic, H., Franceschetti, T., Roeder, E., Matic, I., Vidovic, I., Joshi, P., Kum, K.Y., and Kalajzic, I. (2016). Gene-expression analysis of cementoblasts and osteoblasts. *Journal of periodontal research* *51*, 304-312. 10.1111/jre.12309.
- Matz, A., Lee, S.J., Schwedhelm-Domeyer, N., Zanini, D., Holubowska, A., Kannan, M., Farnworth, M., Jahn, O., Gopfert, M.C., and Stegmuller, J. (2015). Regulation of neuronal survival and morphology by the E3 ubiquitin ligase RNF157. *Cell death and differentiation* *22*, 626-642. 10.1038/cdd.2014.163.
- McInnes, L., Healy, J., and Melville, J. (2018). Umap: Uniform manifold approximation and projection for dimension reduction. *arXiv preprint arXiv:1802.03426*.
- Meng, D., Frank, A.R., and Jewell, J.L. (2018). mTOR signaling in stem and progenitor cells. *Development (Cambridge, England)* *145*. 10.1242/dev.152595.
- Miao, Z., Deng, K., Wang, X., and Zhang, X. (2018). DEsingle for detecting three types of differential expression in single-cell RNA-seq data. *Bioinformatics (Oxford, England)* *34*, 3223-3224. 10.1093/bioinformatics/bty332.
- Miletich, I., and Sharpe, P.T. (2004). Neural crest contribution to mammalian tooth formation. *Birth defects research. Part C, Embryo today : reviews* *72*, 200-212. 10.1002/bdrc.20012.
- Miletich, I., Yu, W.Y., Zhang, R., Yang, K., Caixeta de Andrade, S., Pereira, S.F., Ohazama, A., Mock, O.B., Buchner, G., Sealby, J., et al. (2011). Developmental stalling and organ-autonomous regulation of morphogenesis. *Proceedings of the National Academy of Sciences of the United States of America* *108*, 19270-19275. 10.1073/pnas.1112801108.
- Moiseeva, E.P., Belkin, A.M., Spurr, N.K., Koteliansky, V.E., and Critchley, D.R. (1996). A Novel Dystrophin/Utrophin-Associated Protein is an Enzymatically Inactive Member of the Phosphoglucosyltransferase Superfamily. *The FEBS journal* *235*, 103-113.
- Molt, S., Buhrdel, J.B., Yakovlev, S., Schein, P., Orfanos, Z., Kirfel, G., Winter, L., Wiche, G., van der Ven, P.F., Rottbauer, W., et al. (2014). Aciculin interacts with filamin C and Xin and is essential for myofibril assembly, remodeling and maintenance. *Journal of cell science* *127*, 3578-3592. 10.1242/jcs.152157.

- Montagnani, S., Rueger, M.A., Hosoda, T., and Nurzynska, D. (2016). Adult Stem Cells in Tissue Maintenance and Regeneration. *Stem cells international* 2016, 7362879. 10.1155/2016/7362879.
- Moody, J.D., Levy, S., Mathieu, J., Xing, Y., Kim, W., Dong, C., Tempel, W., Robitaille, A.M., Dang, L.T., Ferreccio, A., et al. (2017). First critical repressive H3K27me3 marks in embryonic stem cells identified using designed protein inhibitor. *Proceedings of the National Academy of Sciences of the United States of America* 114, 10125-10130. 10.1073/pnas.1706907114.
- Muguruma, Y., Reyes, M., Nakamura, Y., Sato, T., Matsuzawa, H., Miyatake, H., Akatsuka, A., Itoh, J., Yahata, T., Ando, K., et al. (2003). In vivo and in vitro differentiation of myocytes from human bone marrow-derived multipotent progenitor cells. *Experimental hematology* 31, 1323-1330.
- Muruganandan, S., Roman, A.A., and Sinal, C.J. (2010). Role of chemerin/CMKLR1 signaling in adipogenesis and osteoblastogenesis of bone marrow stem cells. *Journal of bone and mineral research : the official journal of the American Society for Bone and Mineral Research* 25, 222-234. 10.1359/jbmr.091106.
- Nakamura, M., Bringas, P., Jr., and Slavkin, H.C. (1991). Inner enamel epithelia synthesize and secrete enamel proteins during mouse molar occlusal "enamel-free area" development. *Journal of craniofacial genetics and developmental biology* 11, 96-104.
- Nakamura, T., Jimenez-Rojo, L., Koyama, E., Pacifici, M., de Vega, S., Iwamoto, M., Fukumoto, S., Unda, F., and Yamada, Y. (2017). Epirofin Regulates Enamel Formation and Tooth Morphogenesis by Controlling Epithelial-Mesenchymal Interactions During Tooth Development. *Journal of bone and mineral research : the official journal of the American Society for Bone and Mineral Research* 32, 601-610. 10.1002/jbmr.3024.
- Nanci, A., and TenCate, A.R. (2018). Ten Cate's oral histology : development, structure, and function.
- Nelson, S.J. (2020). Wheeler's dental anatomy, physiology, and occlusion.
- Neves, V.C., Babb, R., Chandrasekaran, D., and Sharpe, P.T. (2017). Promotion of natural tooth repair by small molecule GSK3 antagonists. *Scientific reports* 7, 39654. 10.1038/srep39654.
- Nistala, H., Lee-Arteaga, S., Smaldone, S., Siciliano, G., and Ramirez, F. (2010). Extracellular microfibrils control osteoblast-supported osteoclastogenesis by restricting TGF{beta} stimulation of RANKL production. *The Journal of biological chemistry* 285, 34126-34133. 10.1074/jbc.M110.125328.
- Ochiai, H., Suga, H., Yamada, T., Sakakibara, M., Kasai, T., Ozone, C., Ogawa, K., Goto, M., Banno, R., Tsunekawa, S., et al. (2015). BMP4 and FGF strongly induce differentiation of mouse ES cells into oral ectoderm. *Stem cell research* 15, 290-298. 10.1016/j.scr.2015.06.011.

- Oh, J., Lee, Y.D., and Wagers, A.J. (2014). Stem cell aging: mechanisms, regulators and therapeutic opportunities. *Nature Medicine* 20, 870. 10.1038/nm.3651.
- Oja, S., Komulainen, P., Penttila, A., Nystedt, J., and Korhonen, M. (2018). Automated image analysis detects aging in clinical-grade mesenchymal stromal cell cultures. *Stem cell research & therapy* 9, 6. 10.1186/s13287-017-0740-x.
- Onishi, K., and Zandstra, P.W. (2015). LIF signaling in stem cells and development. *Development (Cambridge, England)* 142, 2230-2236. 10.1242/dev.117598.
- Paduano, F., Marrelli, M., White, L.J., Shakesheff, K.M., and Tatullo, M. (2016). Odontogenic Differentiation of Human Dental Pulp Stem Cells on Hydrogel Scaffolds Derived from Decellularized Bone Extracellular Matrix and Collagen Type I. *PloS one* 11, e0148225. 10.1371/journal.pone.0148225.
- Park, S.J., Bae, H.S., Cho, Y.S., Lim, S.R., Kang, S.A., and Park, J.C. (2013). Apoptosis of the reduced enamel epithelium and its implications for bone resorption during tooth eruption. *Journal of molecular histology* 44, 65-73. 10.1007/s10735-012-9465-4.
- Pires, A.O., Mendes-Pinheiro, B., Teixeira, F.G., Anjo, S.I., Ribeiro-Samy, S., Gomes, E.D., Serra, S.C., Silva, N.A., Manadas, B., Sousa, N., and Salgado, A.J. (2016). Unveiling the Differences of Secretome of Human Bone Marrow Mesenchymal Stem Cells, Adipose Tissue-Derived Stem Cells, and Human Umbilical Cord Perivascular Cells: A Proteomic Analysis. *Stem cells and development* 25, 1073-1083. 10.1089/scd.2016.0048.
- Pittenger, M.F., Mackay, A.M., Beck, S.C., Jaiswal, R.K., Douglas, R., Mosca, J.D., Moorman, M.A., Simonetti, D.W., Craig, S., and Marshak, D.R. (1999). Multilineage potential of adult human mesenchymal stem cells. *Science* 284, 143-147.
- Ponnaiyan, D., and Jegadeesan, V. (2014). Comparison of phenotype and differentiation marker gene expression profiles in human dental pulp and bone marrow mesenchymal stem cells. *European journal of dentistry* 8, 307-313. 10.4103/1305-7456.137631.
- Popova, A.P., Bozyk, P.D., Goldsmith, A.M., Linn, M.J., Lei, J., Bentley, J.K., and Hershenson, M.B. (2010). Autocrine production of TGF-beta1 promotes myofibroblastic differentiation of neonatal lung mesenchymal stem cells. *American journal of physiology. Lung cellular and molecular physiology* 298, L735-743. 10.1152/ajplung.00347.2009.
- Purcell, M., Kruger, A., and Tainsky, M.A. (2014). Gene expression profiling of replicative and induced senescence. *Cell cycle (Georgetown, Tex.)* 13, 3927-3937. 10.4161/15384101.2014.973327.
- Qiu, X., Mao, Q., Tang, Y., Wang, L., Chawla, R., Pliner, H.A., and Trapnell, C. (2017). Reversed graph embedding resolves complex single-cell trajectories. *Nature methods* 14, 979-982. 10.1038/nmeth.4402.
- Quirós-Terrón, L., Arráez-Aybar, L.A., Murillo-González, J., De-la-Cuadra-Blanco, C., Martínez-Álvarez, M.C., Sanz-Casado, J.V., and Mérida-Velasco, J.R. (2019). Initial

- stages of development of the submandibular gland (human embryos at 5.5-8 weeks of development). *Journal of anatomy* 234, 700-708. 10.1111/joa.12955.
- Radlanski, R.J., Renz, H., Tsengelsaikhan, N., Schuster, F., and Zimmermann, C.A. (2016). The remodeling pattern of human mandibular alveolar bone during prenatal formation from 19 to 270mm CRL. *Annals of anatomy = Anatomischer Anzeiger : official organ of the Anatomische Gesellschaft* 205, 65-74. 10.1016/j.aanat.2016.01.005.
- Rao, K.B., Malathi, N., Narashiman, S., and Rajan, S.T. (2014). Evaluation of myofibroblasts by expression of alpha smooth muscle actin: a marker in fibrosis, dysplasia and carcinoma. *Journal of clinical and diagnostic research : JCDR* 8, Zc14-17. 10.7860/jcdr/2014/7820.4231.
- Reed, M.J., Vernon, R.B., Abrass, I.B., and Sage, E.H. (1994). TGF-beta 1 induces the expression of type I collagen and SPARC, and enhances contraction of collagen gels, by fibroblasts from young and aged donors. *Journal of cellular physiology* 158, 169-179. 10.1002/jcp.1041580121.
- Renstrom, J., Istvanffy, R., Gauthier, K., Shimono, A., Mages, J., Jardon-Alvarez, A., Kroger, M., Schiemann, M., Busch, D.H., Esposito, I., et al. (2009). Secreted frizzled-related protein 1 extrinsically regulates cycling activity and maintenance of hematopoietic stem cells. *Cell stem cell* 5, 157-167. 10.1016/j.stem.2009.05.020.
- Rhodes, C.S., Yoshitomi, Y., Burbelo, P.D., Freese, N.H., Nakamura, T., Chiba, Y., and Yamada, Y. (2021). Sp6/Epiprofin is a master regulator in the developing tooth. *Biochemical and biophysical research communications* 581, 89-95. 10.1016/j.bbrc.2021.10.017.
- Sadanandam, A., Rosenbaugh, E.G., Singh, S., Varney, M., and Singh, R.K. (2010). Semaphorin 5A promotes angiogenesis by increasing endothelial cell proliferation, migration, and decreasing apoptosis. *Microvascular research* 79, 1-9. 10.1016/j.mvr.2009.10.005.
- Sarrazy, V., Koehler, A., Chow, M.L., Zimina, E., Li, C.X., Kato, H., Caldarone, C.A., and Hinz, B. (2014). Integrins alphavbeta5 and alphavbeta3 promote latent TGF-beta1 activation by human cardiac fibroblast contraction. *Cardiovascular research* 102, 407-417. 10.1093/cvr/cvu053.
- Schindelin, J., Arganda-Carreras, I., Frise, E., Kaynig, V., Longair, M., Pietzsch, T., Preibisch, S., Rueden, C., Saalfeld, S., Schmid, B., et al. (2012). Fiji: an open-source platform for biological-image analysis. *Nature methods* 9, 676-682. 10.1038/nmeth.2019.
- Schindelin, J., Rueden, C.T., Hiner, M.C., and Eliceiri, K.W. (2015). The ImageJ ecosystem: An open platform for biomedical image analysis. *Molecular reproduction and development* 82, 518-529. 10.1002/mrd.22489.
- Seidel, K., Ahn, C.P., Lyons, D., Nee, A., Ting, K., Brownell, I., Cao, T., Carano, R.A., Curran, T., Schober, M., et al. (2010). Hedgehog signaling regulates the generation of ameloblast

- progenitors in the continuously growing mouse incisor. *Development (Cambridge, England)* *137*, 3753-3761. 10.1242/dev.056358.
- Sharir, A., Marangoni, P., Zilionis, R., Wan, M., Wald, T., Hu, J.K., Kawaguchi, K., Castillo-Azofeifa, D., Epstein, L., Harrington, K., et al. (2019). A large pool of actively cycling progenitors orchestrates self-renewal and injury repair of an ectodermal appendage. *Nature cell biology* *21*, 1102-1112. 10.1038/s41556-019-0378-2.
- Sharpe, P.T. (2016). Dental mesenchymal stem cells. *Development (Cambridge, England)* *143*, 2273-2280. 10.1242/dev.134189.
- Shi, S., and Gronthos, S. (2003). Perivascular niche of postnatal mesenchymal stem cells in human bone marrow and dental pulp. *Journal of bone and mineral research : the official journal of the American Society for Bone and Mineral Research* *18*, 696-704. 10.1359/jbmr.2003.18.4.696.
- Shibata, S., and Ishiyama, J. (2013). Secreted protein acidic and rich in cysteine (SPARC) is upregulated by transforming growth factor (TGF)-beta and is required for TGF-beta-induced hydrogen peroxide production in fibroblasts. *Fibrogenesis & tissue repair* *6*, 6. 10.1186/1755-1536-6-6.
- Shimaoka, H., Dohi, Y., Ohgushi, H., Ikeuchi, M., Okamoto, M., Kudo, A., Kirita, T., and Yonemasu, K. (2004). Recombinant growth/differentiation factor-5 (GDF-5) stimulates osteogenic differentiation of marrow mesenchymal stem cells in porous hydroxyapatite ceramic. *Journal of biomedical materials research. Part A* *68*, 168-176. 10.1002/jbm.a.20059.
- Shyh-Chang, N., and Daley, G.Q. (2013). Lin28: primal regulator of growth and metabolism in stem cells. *Cell stem cell* *12*, 395-406. 10.1016/j.stem.2013.03.005.
- Siegel, G., Kluba, T., Hermanutz-Klein, U., Bieback, K., Northoff, H., and Schafer, R. (2013). Phenotype, donor age and gender affect function of human bone marrow-derived mesenchymal stromal cells. *BMC medicine* *11*, 146. 10.1186/1741-7015-11-146.
- Simsek, T., Kocabas, F., Zheng, J., Deberardinis, R.J., Mahmoud, A.I., Olson, E.N., Schneider, J.W., Zhang, C.C., and Sadek, H.A. (2010). The distinct metabolic profile of hematopoietic stem cells reflects their location in a hypoxic niche. *Cell stem cell* *7*, 380-390. 10.1016/j.stem.2010.07.011.
- Snoeck, H.W. (2018). Mitochondrial regulation of hematopoietic stem cells. *Current opinion in cell biology* *49*, 91-98. 10.1016/j.ceb.2017.12.010.
- Soteriou, D., and Fuchs, Y. (2018). A matter of life and death: stem cell survival in tissue regeneration and tumour formation. *Nature reviews. Cancer*. 10.1038/nrc.2017.122.
- Sperber, H., Mathieu, J., Wang, Y., Ferreccio, A., Hesson, J., Xu, Z., Fischer, K.A., Devi, A., Detraux, D., Gu, H., et al. (2015). The metabolome regulates the epigenetic landscape

- during naive-to-primed human embryonic stem cell transition. *Nature cell biology* *17*, 1523-1535. 10.1038/ncb3264.
- Sperber, S.M., and Dawid, I.B. (2008). *barx1* is necessary for ectomesenchyme proliferation and osteochondroprogenitor condensation in the zebrafish pharyngeal arches. *Developmental biology* *321*, 101-110. 10.1016/j.ydbio.2008.06.004.
- Stadler, B., Ivanovska, I., Mehta, K., Song, S., Nelson, A., Tan, Y., Mathieu, J., Darby, C., Blau, C.A., Ware, C., et al. (2010). Characterization of microRNAs involved in embryonic stem cell states. *Stem cells and development* *19*, 935-950. 10.1089/scd.2009.0426.
- Suga, H., Kadoshima, T., Minaguchi, M., Ohgushi, M., Soen, M., Nakano, T., Takata, N., Wataya, T., Muguruma, K., Miyoshi, H., et al. (2011). Self-formation of functional adenohipophysis in three-dimensional culture. *Nature* *480*, 57-62. 10.1038/nature10637.
- Sun, Z., Yu, W., Sanz Navarro, M., Sweat, M., Eliason, S., Sharp, T., Liu, H., Seidel, K., Zhang, L., Moreno, M., et al. (2016). Sox2 and Lef-1 interact with Pitx2 to regulate incisor development and stem cell renewal. *Development (Cambridge, England)* *143*, 4115-4126. 10.1242/dev.138883.
- Szklarczyk, D., Franceschini, A., Wyder, S., Forslund, K., Heller, D., Huerta-Cepas, J., Simonovic, M., Roth, A., Santos, A., Tsafou, K.P., et al. (2015). STRING v10: protein-protein interaction networks, integrated over the tree of life. *Nucleic Acids Research* *43*, D447-452. 10.1093/nar/gku1003.
- T, L.R., Sanchez-Abarca, L.I., Muntion, S., Preciado, S., Puig, N., Lopez-Ruano, G., Hernandez-Hernandez, A., Redondo, A., Ortega, R., Rodriguez, C., et al. (2016). MSC surface markers (CD44, CD73, and CD90) can identify human MSC-derived extracellular vesicles by conventional flow cytometry. *Cell communication and signaling : CCS* *14*, 2. 10.1186/s12964-015-0124-8.
- Takamori, K., Hosokawa, R., Xu, X., Deng, X., Bringas, P., Jr., and Chai, Y. (2008). Epithelial fibroblast growth factor receptor 1 regulates enamel formation. *Journal of dental research* *87*, 238-243. 10.1177/154405910808700307.
- Takashima, Y., Guo, G., Loos, R., Nichols, J., Ficuz, G., Krueger, F., Oxley, D., Santos, F., Clarke, J., Mansfield, W., et al. (2014). Resetting transcription factor control circuitry toward ground-state pluripotency in human. *Cell* *158*, 1254-1269. 10.1016/j.cell.2014.08.029.
- Tanaka, J., Ogawa, M., Hojo, H., Kawashima, Y., Mabuchi, Y., Hata, K., Nakamura, S., Yasuhara, R., Takamatsu, K., Irié, T., et al. (2018). Generation of orthotopically functional salivary gland from embryonic stem cells. *Nat Commun* *9*, 4216. 10.1038/s41467-018-06469-7.
- Tarca, A.L., Kathri, P., and Draghici, S. (2013). SPIA: Signaling Pathway Impact Analysis (SPIA) using combined evidence of pathway over-representation and unusual signaling perturbations. R package version 2.

- Thesleff, I. (2014). Current understanding of the process of tooth formation: transfer from the laboratory to the clinic. *Australian dental journal* *59 Suppl 1*, 48-54. 10.1111/adj.12102.
- Thesleff, I., Keränen, S., and Jernvall, J. (2001). Enamel knots as signaling centers linking tooth morphogenesis and odontoblast differentiation. *Advances in dental research* *15*, 14-18. 10.1177/08959374010150010401.
- Theunissen, T.W., Friedli, M., He, Y., Planet, E., O'Neil, R.C., Markoulaki, S., Pontis, J., Wang, H., Iouranova, A., Imbeault, M., et al. (2016). Molecular Criteria for Defining the Naive Human Pluripotent State. *Cell stem cell* *19*, 502-515. 10.1016/j.stem.2016.06.011.
- Theunissen, T.W., Powell, B.E., Wang, H., Mitalipova, M., Faddah, D.A., Reddy, J., Fan, Z.P., Maetzel, D., Ganz, K., Shi, L., et al. (2014). Systematic identification of culture conditions for induction and maintenance of naive human pluripotency. *Cell stem cell* *15*, 471-487. 10.1016/j.stem.2014.07.002.
- Tian, S., Tian, X., Liu, Y., Dong, F., Wang, J., Liu, X., Zhang, Z., and Chen, H. (2017). Effects of TAZ on human dental pulp stem cell proliferation and migration. *Molecular medicine reports* *15*, 4326-4332. 10.3892/mmr.2017.6550.
- Tipping, A.J., Pina, C., Castor, A., Hong, D., Rodrigues, N.P., Lazzari, L., May, G.E., Jacobsen, S.E., and Enver, T. (2009). High GATA-2 expression inhibits human hematopoietic stem and progenitor cell function by effects on cell cycle. *Blood* *113*, 2661-2672. 10.1182/blood-2008-06-161117.
- Traag, V.A., Waltman, L., and van Eck, N.J. (2019). From Louvain to Leiden: guaranteeing well-connected communities. *Scientific reports* *9*, 5233. 10.1038/s41598-019-41695-z.
- Trapnell, C., Cacchiarelli, D., Grimsby, J., Pokharel, P., Li, S., Morse, M., Lennon, N.J., Livak, K.J., Mikkelsen, T.S., and Rinn, J.L. (2014). The dynamics and regulators of cell fate decisions are revealed by pseudotemporal ordering of single cells. *Nature biotechnology* *32*, 381-386. 10.1038/nbt.2859.
- Trapnell, C., Pachter, L., and Salzberg, S.L. (2009). TopHat: discovering splice junctions with RNA-Seq. *Bioinformatics (Oxford, England)* *25*, 1105-1111. 10.1093/bioinformatics/btp120.
- Tucker, A.S., Matthews, K.L., and Sharpe, P.T. (1998). Transformation of tooth type induced by inhibition of BMP signaling. *Science* *282*, 1136-1138.
- Tung, P.Y., Varlakhanova, N.V., and Knoepfler, P.S. (2013). Identification of DPPA4 and DPPA2 as a novel family of pluripotency-related oncogenes. *Stem cells (Dayton, Ohio)* *31*, 2330-2342. 10.1002/stem.1526.
- Vahtokari, A., Aberg, T., Jernvall, J., Keränen, S., and Thesleff, I. (1996). The enamel knot as a signaling center in the developing mouse tooth. *Mechanisms of development* *54*, 39-43. 10.1016/0925-4773(95)00459-9.

- Vallénus, T. (2013). Actin stress fibre subtypes in mesenchymal-migrating cells. *Open biology* 3, 130001. 10.1098/rsob.130001.
- Vander Heiden, M.G., Cantley, L.C., and Thompson, C.B. (2009). Understanding the Warburg effect: the metabolic requirements of cell proliferation. *Science* 324, 1029-1033. 10.1126/science.1160809.
- Vardouli, L., Vasilaki, E., Papadimitriou, E., Kardassis, D., and Stournaras, C. (2008). A novel mechanism of TGFbeta-induced actin reorganization mediated by Smad proteins and Rho GTPases. *The FEBS journal* 275, 4074-4087. 10.1111/j.1742-4658.2008.06549.x.
- Vaughan, M.B., Howard, E.W., and Tomasek, J.J. (2000). Transforming growth factor-beta1 promotes the morphological and functional differentiation of the myofibroblast. *Experimental cell research* 257, 180-189. 10.1006/excr.2000.4869.
- Wang, B., Lee, W.Y., Huang, B., Zhang, J.F., Wu, T., Jiang, X., Wang, C.C., and Li, G. (2016). Secretome of Human Fetal Mesenchymal Stem Cell Ameliorates Replicative Senescence. *Stem cells and development* 25, 1755-1766. 10.1089/scd.2016.0079.
- Wang, B., Lindley, L.E., Fernandez-Vega, V., Rieger, M.E., Sims, A.H., and Briegel, K.J. (2012). The T box transcription factor TBX2 promotes epithelial-mesenchymal transition and invasion of normal and malignant breast epithelial cells. *PloS one* 7, e41355. 10.1371/journal.pone.0041355.
- Wang, G., Liu, J., Cai, Y., Chen, J., Xie, W., Kong, X., Huang, W., Guo, H., Zhao, X., Lu, Y., et al. (2017). Loss of Barx1 promotes hepatocellular carcinoma metastasis through up-regulating MGAT5 and MMP9 expression and indicates poor prognosis. *Oncotarget* 8, 71867-71880. 10.18632/oncotarget.18288.
- Wang, Y. (2020). talk1r uncovers ligand-receptor mediated intercellular crosstalk. *bioRxiv*, 2020.2002.2001.930602. 10.1101/2020.02.01.930602.
- Ware, C.B., Nelson, A.M., Mecham, B., Hesson, J., Zhou, W., Jonlin, E.C., Jimenez-Caliani, A.J., Deng, X., Cavanaugh, C., Cook, S., et al. (2014). Derivation of naive human embryonic stem cells. *Proceedings of the National Academy of Sciences of the United States of America* 111, 4484-4489. 10.1073/pnas.1319738111.
- Warstat, K., Meckbach, D., Weis-Klemm, M., Hack, A., Klein, G., de Zwart, P., and Aicher, W.K. (2010). TGF-beta enhances the integrin alpha2beta1-mediated attachment of mesenchymal stem cells to type I collagen. *Stem cells and development* 19, 645-656. 10.1089/scd.2009.0208.
- Weitzman, J.B., Fiette, L., Matsuo, K., and Yaniv, M. (2000). JunD protects cells from p53-dependent senescence and apoptosis. *Molecular cell* 6, 1109-1119.
- Welch, J.D., Kozareva, V., Ferreira, A., Vanderburg, C., Martin, C., and Macosko, E.Z. (2019). Single-Cell Multi-omic Integration Compares and Contrasts Features of Brain Cell Identity. *Cell* 177, 1873-1887.e1817. 10.1016/j.cell.2019.05.006.

- Wipff, P.J., and Hinz, B. (2008). Integrins and the activation of latent transforming growth factor beta1 - an intimate relationship. *European journal of cell biology* 87, 601-615. 10.1016/j.ejcb.2008.01.012.
- Wise, G.E., Marks, S.C., Jr., and Zhao, L. (1998). Effect of CSF-1 on in vivo expression of c-fos in the dental follicle during tooth eruption. *European journal of oral sciences* 106 Suppl 1, 397-400. 10.1111/j.1600-0722.1998.tb02205.x.
- Wordinger, R.J., Fleenor, D.L., Hellberg, P.E., Pang, I.H., Tovar, T.O., Zode, G.S., Fuller, J.A., and Clark, A.F. (2007). Effects of TGF-beta2, BMP-4, and gremlin in the trabecular meshwork: implications for glaucoma. *Investigative ophthalmology & visual science* 48, 1191-1200. 10.1167/iovs.06-0296.
- Yajima-Himuro, S., Oshima, M., Yamamoto, G., Ogawa, M., Furuya, M., Tanaka, J., Nishii, K., Mishima, K., Tachikawa, T., Tsuji, T., and Yamamoto, M. (2014). The junctional epithelium originates from the odontogenic epithelium of an erupted tooth. *Scientific reports* 4, 4867. 10.1038/srep04867.
- Yamada, T., Park, C.S., Burns, A., Nakada, D., and Lacorazza, H.D. (2012). The cytosolic protein G0S2 maintains quiescence in hematopoietic stem cells. *PloS one* 7, e38280. 10.1371/journal.pone.0038280.
- Ye, J., and Blueloch, R. (2014). Regulation of pluripotency by RNA binding proteins. *Cell stem cell* 15, 271-280. 10.1016/j.stem.2014.08.010.
- Yoon, I.K., Kim, H.K., Kim, Y.K., Song, I.H., Kim, W., Kim, S., Baek, S.H., Kim, J.H., and Kim, J.R. (2004). Exploration of replicative senescence-associated genes in human dermal fibroblasts by cDNA microarray technology. *Exp Gerontol* 39, 1369-1378. 10.1016/j.exger.2004.07.002.
- Yu, M., Wang, H., Fan, Z., Xie, C., Liu, H., Liu, Y., Han, D., Wong, S.W., and Feng, H. (2019a). BMP4 mutations in tooth agenesis and low bone mass. *Archives of oral biology* 103, 40-46. 10.1016/j.archoralbio.2019.05.012.
- Yu, M., Wong, S.W., Han, D., and Cai, T. (2019b). Genetic analysis: Wnt and other pathways in nonsyndromic tooth agenesis. *Oral diseases* 25, 646-651. 10.1111/odi.12931.
- Yu, T., and Klein, O.D. (2020). Molecular and cellular mechanisms of tooth development, homeostasis and repair. *Development (Cambridge, England)* 147. 10.1242/dev.184754.
- Yu, W., Sun, Z., Sweat, Y., Sweat, M., Venugopalan, S.R., Eliason, S., Cao, H., Paine, M.L., and Amendt, B.A. (2020). Pitx2-Sox2-Lef1 interactions specify progenitor oral/dental epithelial cell signaling centers. *Development (Cambridge, England)* 147. 10.1242/dev.186023.
- Zamani, S., Hashemibeni, B., Esfandiari, E., Kabiri, A., Rabbani, H., and Abutorabi, R. (2014). Assessment of TGF-beta3 on production of aggrecan by human articular chondrocytes in pellet culture system. *Advanced biomedical research* 3, 54. 10.4103/2277-9175.125799.

Zhang, H., Ryu, D., Wu, Y., Gariani, K., Wang, X., Luan, P., D'Amico, D., Ropelle, E.R., Lutolf, M.P., Aebersold, R., et al. (2016). NAD(+) repletion improves mitochondrial and stem cell function and enhances life span in mice. *Science* 352, 1436-1443. [10.1126/science.aaf2693](https://doi.org/10.1126/science.aaf2693).

Zheng, X., Boyer, L., Jin, M., Mertens, J., Kim, Y., Ma, L., Hamm, M., Gage, F.H., and Hunter, T. (2016). Metabolic reprogramming during neuronal differentiation from aerobic glycolysis to neuronal oxidative phosphorylation. *eLife* 5. [10.7554/eLife.13374](https://doi.org/10.7554/eLife.13374).

VITA

1. **NAME:** Ammar Ahmed Alghadeer
2. **NATIONALITY:** Saudi
3. **DATE AND PLACE OF BIRTH:** Dec 20, 1985 – Dammam, Saudi Arabia
4. **MARITAL STATUS:** Single
5. **ADDRESS:**

CURRENT ADDRESS (USA):

2820 EASTLAKE AVE E,
APT 610
Seattle, WA 98102,
USA.

Mobile: (+1) 2064609162

E-mail: amar1406@uw.edu

PERMENANT ADDRESS:

2713 - 9B Street - Al Kawther
Saihat, 32431 7715, Saudi Arabia

Mobile: (+966) 56930800

E-mail: dr.alghadeer@gmail.com

6. **ACADEMIC QUALIFICATIONS (in chronological order):**

Academic Degree	Place of Issue	Address	Date
MSc Degree in Regenerative Dentistry	King's College London.	London United Kingdom	Nov 2014
Bachelor Degree of Dental Surgery	University of Dammam	Dammam Saudi Arabia	April 2011

7. PROFESSIONAL RECORD (beginning from the most recent):

Job Rank	Place and Address of Work	Date
PhD Student	Department of Oral Health Sciences, University of Washington, School of Dentistry, Seattle, WA 98109, USA	Sept. 2016 – Present
MSc Student	Department of Craniofacial Development & Stem Cell Biology, King's College London. London, United Kingdom	Sept. 2013 – Nov 2014
Demonstrator in Oral Biology.	Biomedical Dental Science Department, Imam Abdul Rahman Bin Faisal University, College of Dentistry / P.O.Box 1982, Dammam 31441, Saudi Arabia.	Dec. 2011 – Present
G.P Dentist	Al-Khaim Dento-Facial Aesthetic private center in Al-Hassa, Saudi Arabia.	May 2011 – Sept 2011
Intern	Department of Dentistry at Dammam Central Hospital, Dammam, Saudi Arabia	Jan 2011 – Mar 2011
Intern	Department of Dentistry at Dhahran Airbase Hospital, Dhahran, Saudi Arabia.	Oct 2010 – Dec 2010
Intern	College of Dentistry, University of Dammam, Dammam, Saudi Arabia.	April 2010 – Sept 2010
Dental Student	College of Dentistry, University of Dammam (Formerly known as King Faisal University)	Sept 2003 – April 2010

8. Language Proficiency:

- ARABIC
- ENGLISH

FORM (B): SCIENTIFIC ACHIEVEMENTS

B (1) Current Research:

S. No.	Name of Investigator/s	Research Title	Status
1	Alghadeer A, Hanson-Drury S, Ehnes D, Zhao YT, Patni AP, O'Day D, Spurrell CH, Gogate AA, Phal A, Zhang H, Devi A, Wang Y, Starita L, Doherty D, Glass I, Shendure J, Baker D, Regier MC, Mathieu J, Ruohola- Baker H	Human iPSC Derived Enamel Organoid Guided by Single-Cell Atlas of Human Tooth Development	In review

B (2) Previous Research:

S. No.	Name of Investigator/s	Research Title	Status
1	Dannie Macrin*, Ammar Alghadeer* , Yan Ting Zhao, Jason W. Miklas, Abdiasis M. Hussein, Damien Detraux, Aaron M. Robitaille, Anup Madan, Randall T. Moon, Yuliang Wang, Devi Arikketh, Julie Mathieu, and Hannele Ruohola- Baker. *first co-authors	Metabolism as an early predictor of DPSCs aging	Published in <i>Scientific Reports</i> (18th Feb 19) DOI: 10.1038/s41598-018- 37489-4
	Tucker A. S, Alghadeer A.A.	Development of tooth replacement: Formation of Competent Successional Lamina in Diphyodont.	Unpublished work.

2	Emad O. AlShwaimi, Usama A. Badawi, Ammar Alghadeer , Ahmad AlMajed, Aiman A. Ali.	Computer Knowledge: A Comparative Study among Dental and Non Dental Students at the University of Dammam.	Accepted for publication in Al-Azhar Dental Journal. May 2013
---	---	--	---

B (3) Research Interest:

S. No	Research Subject
1	Stem cell biology & Tissue engineering.
2	Tooth development.
3	Salivary gland regeneration.
4	Cancer stem cell.

B (4) Contribution to Scientific Conferences & Symposia:

S. No.	Name of Conference	Place & Date	Participation
1	2022 IADR/APR General Session & Exhibition Virtual Experience.	June 22, 2022 China	Live Presentation
2	IADR/AADR/CADR General Session & Exhibition	18-21 th March 2020, Washington, D.C., USA	Selected for Oral Pres Selected as a finalist for the Craniofacial Biology Group Sarnat Poster Competition.
3	King Saud University 16th International Dental Conference The 27th for the Saudi Dental Society. (Regenerative Dentistry)	5-7 th Jan 2016, Riyadh International Convention & Exhibition Center	ATTENDEE

4	Continuing education course on the topic of “How to use and work with stem cells?” - by Prof. George Huang	5 th Jan 2016. Riyadh International Convention & Exhibition Center	CE Course ATTENDEE
5	10 th SORG Middle East Course (Orthognathic Surgery)	University of Dammam, College of Dentistry, Dammam,Saudi Arabia 14 th Feb, 2013	Organizer
6	“Prosthodontic Options in Implant Dentistry” “Management of Alveolar Ridge Deficiencies”	University of Dammam, College of Dentistry, Dammam,Saudi Arabia 25 th Dec,2012	ATTENDEE
7	“Evidence Based Periodontology: The search for Best Evidence”	University of Dammam, College of Dentistry, Dammam,Saudi Arabia 27 th Nov, 2012	ATTENDEE
8	The 10 th Annual Symposium (Dentistry in Evidence-based Practice Era)	Sheraton Dammam Hotel & Towers May, 2012	Organizer
9	“Interceptive Orthodontic Workshop”	University of Dammam, College of Dentistry, Dammam,Saudi Arabia 5th May 2011	ATTENDEE
10	The 9 th Annual Symposium (Raising the Bar in Dentistry)	University of Dammam, College of Dentistry, Dammam,Saudi Arabia 4th – 5th May 2011	ATTENDEE
11	one-day lecture and workshop on the Low Force-Low Friction Orthodontics (Damon System)	At GULF TERRACE Hotel, Al Khobar, Saudi Arabia 25 th February 2011	ATTENDEE
12	Mastering Molar Endodontic Workshops- Saudi Dental Society	University of Dammam, College of Dentistry, Dammam,Saudi Arabia 24 th February 2011	WORKSHOP
13	Monthly Scientific Activity of the Saudi Dental Society in University of Dammam-October	University of Dammam, College of Dentistry, Dammam,Saudi Arabia 26 th October 2010	ATTENDEE

14	Monthly Scientific Activity of the Saudi Dental Society in University of Dammam-November	University of Dammam, College of Dentistry, Dammam,Saudi Arabia 30 th November 2010	ATTENDEE
15	The 7 th Annual Symposium (Digitization in Dentistry)	at Medical Education Center of King Fahd Hospital of the University Of Dammam, Al-Khobar, Saudi Arabia. 26 th -28 th May 2009	ATTENDEE
16	Annual Pediatric Day Symposium (accredited by the Dental Board of California)	Saudi Aramco, Dhahran, Saudi Arabia 14 th May 2009	ATTENDEE
17	Comprehensive Oral Implantology	Manamah, Kingdom of Bahrain. 14-16 May 2009	ATTENDEE
18	The 6 th Annual Symposium “Restoration of the dentition”	held at the Medical Education Center – Site 1, King Fahad Hospital of the University of Dammam, Saudi Arabia 7 th -8 th May 2008	ATTENDEE
19	How to Master the Technique of Functional and Aesthetic Prostheses over Implants	Manamah, Kingdom of Bahrain. 14-16 March 2007	ATTENDEE
20	The 5 th Annual Update on Dentistry and Oral Medicine, “Pediatric Dentistry: Challenge of the Millennium”	University of Dammam, College of Dentistry, Dammam,Saudi Arabia 9 th April 2007	ATTENDEE
21	The 4th Annual Update on Dentistry & Oral Medicine Symposium, King Faisal University College of Dentistry	Dammam, Saudi Arabia, 7 th -8 th May 2006	ATTENDEE

B (5) Membership of Scientific and Professional Societies and Organizations:

S. No	Name of the Organization	Date
1	International Association for Dental Research	Sept, 2019
2	Saudi Dental Society	Nov, 2010
3	Saudi Commission for Health Specialties	May, 2011

B (6) Prizes conferred upon the candidate:

- Dean's Appreciation Certificate for Outstanding Contribution in College Achievement for Academic Year 2011-2012

FORM (C): TEACHING ACTIVITIES

- **A: Undergraduate**

S. No	Name of the Course
1	Oral Diagnosis; Clinical Instructor; University of Dammam;
2	Oral Radiology; Clinical Instructor; University of Dammam;
3	Oral Biology & Oral Histology; Lab Instructor; University of Dammam;
4	Oral Pathology; Lab Instructor; University of Dammam;
5	Dental Anatomy; Lab Instructor; University of Dammam;
6	Research supervision for students (graduate and undergraduate); Ruohola-baker Lab; University of Washington

FORM (D): COMMUNITY SERVICE

- **COMMUNITY SERVICES:**
 - Participated in the Annual World Autism Awareness Day held in Rashid mall in Khobar, Saudi Arabia, under the slogan "I'm with you".